NITROGEN-DOPED DLC DEPOSITION BY HOT FILAMENT AND INDUCTIVELY COUPLED PLASMA SPUTTERING FOR BIOMEDICAL APPLICATIONS

A Thesis Submitted to the College of

Graduate Studies and Research

In Partial Fulfillment of the Requirements

For the Degree of Master of Science

In the Department of Physics and Engineering Physics

University of Saskatchewan

Saskatoon

By

SEPEHR ESMAEILI KHATIR

PERMISSION TO USE

In presenting this thesis in partial fulfilment of the requirements for a Postgraduate degree from the University of Saskatchewan, I agree that the Libraries of this University may make it freely available for inspection. I further agree that permission for copying of this thesis in any manner, in whole or in part, for scholarly purposes may be granted by the professor or professors who supervised my thesis work or, in their absence, by the Head of the Department or the Dean of the College in which my thesis work was done. It is understood that any copying or publication or use of this thesis or parts thereof for financial gain shall not be allowed without my written permission. It is also understood that due recognition shall be given to me and to the University of Saskatchewan in any scholarly use which may be made of any material in my thesis.

Requests for permission to copy or to make other use of material in this thesis in whole or part should be addressed to:

Head of the Department of Physics and Engineering Physics

116 Science Place

University of Saskatchewan

Saskatoon, Saskatchewan, S7N 5E2

Canada

ABSTRACT

The heart is one of the most important organs of the human body and cardiovascular diseases remain the biggest cause of deaths worldwide. Today, due to the aging of the population and the growing demand for cardiovascular implants, improving the performance of artificial surfaces of vascular prostheses is highly desired. The common material for fabricating prostheses, such as stents used to remedy narrow and weak arteries, is Fluorocarbon polymers or expanded Polytetrafluoroethylene (ePTFE, Gore-tex). Although these polymers are well known for chemical inertness, thermal stability and low friction, they can cause early thrombosis (forming clot) and coagulation in blood vessels and require periodic replacement. Modifying the surface properties of Polytetrafluoroethylene (PTFE) by coating with carbon-based materials may improve its blood compatibility. Carbon-based coatings have properties similar to biomedical components, such as low friction, bioinertness, high wear resistance and exceptional hardness. Plasma processing methods are commonly used for coating thin films on various materials including carbon-based components. Plasma-based processes are also widely used in the aerospace, automotive, steel and biomedical industries. For example, extending the lifetime of surgically implanted hip joints and cutting tools are biomedical and industrial applications of plasma-based material processing respectively. Plasma-assisted deposition techniques are commonly used for carbon-based coating including nitrogen-doped amorphous carbon (a-C) films. In this thesis, PTFE samples with different thickness and roughness characteristics are used as substrates and diamond-like carbon (DLC) is deposited on them by simultaneous plasma-assisted sputtering and chemical vapour deposition (CVD). Hot filament plasma and ICP (Inductively coupling plasma) are used to coat DLC on PTFE and silicon (Si) substrates under various plasma conditions. The latter is the first report on the techniques to coat DLC by ICP

plasma sputtering. This new technique (ICP-sputtering) is developed to improve low deposition rate and high temperature deposition of previous method (Hot filament plasma sputtering). Advantageous of this new developed method (ICP-sputtering) are discussed and compared with the previous method in this thesis. Various amount of nitrogen is introduced to the plasma chambers and the effect of nitrogen dopant is also studied using different characterization techniques for chemical, electronic and morphological properties of coated films. sp^2 and sp^3 contents were also estimated in amorphous carbon (a-C) and nitrogenated amorphous carbon (a-CN) films. Characterization techniques used for in this thesis are including SEM (scanning electron microscopy), AFM (atomic force microscopy), Raman spectroscopy, XAS (x-ray absorption spectroscopy), XES (x-ray emission spectroscopy), XPS (x-ray photoelectron spectroscopy) and XRD (x-ray diffraction).

ACKNOWLEDGMENTS

It is with immense gratitude that I acknowledge the support and help of my supervisors, Professors Chijin Xiao and Akira Hirose, who provided me with an excellent opportunity to grow as a person and student to carry out this research at the University of Saskatchewan. I am also grateful to David McColl for his technical assistance and thoughtful supports in Plasma Physics Laboratory. He is always ready to fix whatever is broken and build whatever is needed.

Special thanks go out to those who provided help in sample characterization: Eamon Mcdermott for collecting XAS and XES data at CLS, Ronny Sutarto who measured the XPS data at CLS, Jason Maley for Raman spectroscopy and AFM at the Saskatchewan Structural Science Center (SSSC), Hamed Akhiani and Siamak Javadian for SEM and XRD measurements. Also, I would like to appreciate the collaboration with Dr. Diego Mantovani and Dr. Lucie Levesque for blood tests on samples at the University Hospital of Laval University (Quebec City).

My warmest thanks to all Plasma Physics Lab-mates for their invaluable help during my study. They created and shard friendly working environment. I cannot find words to express my gratitude to all my friends who provided a loving and peaceful environment for me throughout my study.

This research was funded by the Natural Science and Engineering Research Council of Canada (NSERC) and by Canada Research Chair program. Financial support by the University of Saskatchewan Graduate scholarship is also gratefully acknowledged.

DEDICATION

This work is dedicated to my beloved parents

Aria and Mojgan

TABLE OF CONTENTS

page

LIST OF TABLES

LIST OF FIGURES

LIST OF ABBREVIATIONS

a-C	Amorphous carbon.
a-C:H	Hydrogenated amorphous carbon.
a-C:N:H	Nitrogen doped hydrogenated amorphous carbon
AC	Alternative current.
a-C:N	Nitrogen-doped amorphous carbon.
AFM	Atomic force microscopy.
BE	Backscattered electrons.
CCP	Capacitively coupled plasma.
CLS	Canadian light source.
CNT	Carbon nanotubes.
CRT	Cathode ray display tube.
CVD	Chemical vapour deposition.
DC	Direct current.
DLC	Diamond-like carbon.
ECR	Electron cyclotron resonance.
EELS	Electron energy loss spectroscopy
ePTFE	Expanded polytetrafluoroethylene.
FCVA	Filtered cathodic vacuum arc.
FWHM	Full with half maximum.
GE	Glancing emission.

HCN_X	Refer to table 2.
H-DLC	Hydrogenated diamond-like carbon.
HDP	High-density plasma.
HFCVD	Hot filament chemical vapour deposition.
HOPG	Highly ordered pyrolytic graphite.
IBD	Ion beam deposition.
ICNx	Refer to table 3.
ICP	Inductively coupling plasma.
JCPDS	Joint committee on powder diffraction standards.
LTE	Local thermal equilibrium.
MSIBD	Mass selected ion beam deposition.
NE	Normal emission.
n-LTE	Non-local thermal equilibrium.
NMR	Nuclear magnetic resonance
PECVD	Plasma enhanced chemical vapour deposition.
PFY	Partial fluorescence yield.
PTFE	Polytetrafluoroethylene.
PVD	Physical vapour deposition.
RF	Radio frequency.
RMS	Root mean square.
SCCM	Standard cubic centimeter per minute.

SE	Secondary electrons.
SEM	Scanning electron microscopy.
Si	Silicon.
SSSC	Saskatchewan structural science center.
ta-C	Tetrahedral amorphous carbon.
ta-C:H	Hydrogenated tetrahedral amorphous carbon.
ta-C:N	Tetrahedral amorphous carbon nitride.
ta-C:N:H	Tetrahedral hydrogenated amorphous carbon nitride.
TEY	Total electron yield.
TFE	Tetrafluoroethylene.
TFY	Total fluorescence yield.
XAS	X-ray absorption spectroscopy.
XES	X-ray emission spectroscopy.
XPS	X-ray photoemission spectroscopy.
XRD	X-ray diffraction.

CHAPTER 1

INTRODUCTION

1.1 Motivation

Biomaterials are the materials that are in contact with one or more biological systems. The human body, as a sensitive and complicated biological system, is not compatible with all kinds of materials and it tends to present a hostile reaction to foreign objects such as implants. Thus, providing a good biomaterial requires full understanding of the properties of the materials and how the body reacts to those materials. Finding the most appropriate and biocompatible materials may help to cure more diseases. These days cardiovascular diseases are the leading cause of deaths worldwide, and blood clotting may cause heart attack, stroke, and even death in severe cases. One of the treatments is deploying a stent in the clogged vessel. A stent, as shown in Figure 1 [1], is a very small mesh tube that is permanently inserted into a heart vessel and keeps the arteries open so the blood can flow through them [2].

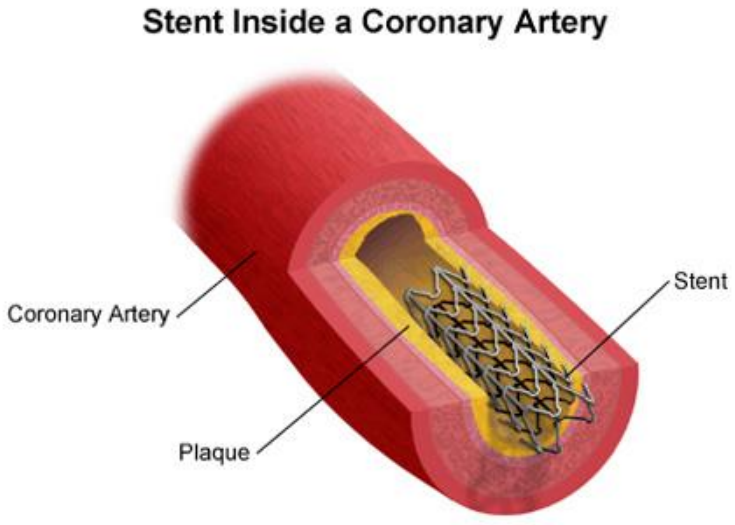

Figure 1. A stent inside a coronary artery with plaque around it

Deploying a stent into a weak or blocked artery is called angioplasty or stenting. It can be done using guide wires, catheters and balloons as shown in Figure 2 [3]. A small hollow tube, called the catheter, is inserted into an artery in a leg or arm and threaded to the affected artery in the heart. A thin flexible metal wire is then advanced through this tube until it passes the centre of blockage in the artery. Then a smaller catheter is inserted over the wire and threaded along the wire to the same narrowed area in the artery. The stent is situated over a balloon on this catheter. When it reaches the blocked zone, the balloon is inflated to reopen the artery. This will flatten the blockage into the artery wall. The stent expands until it hugs the wall of the artery. After a thorough investigation of the region, the balloon is deflated and then withdrawn along with the catheters and the guide wire. The stent remains permanently to provide support to the artery and resist the buildup of plaque.

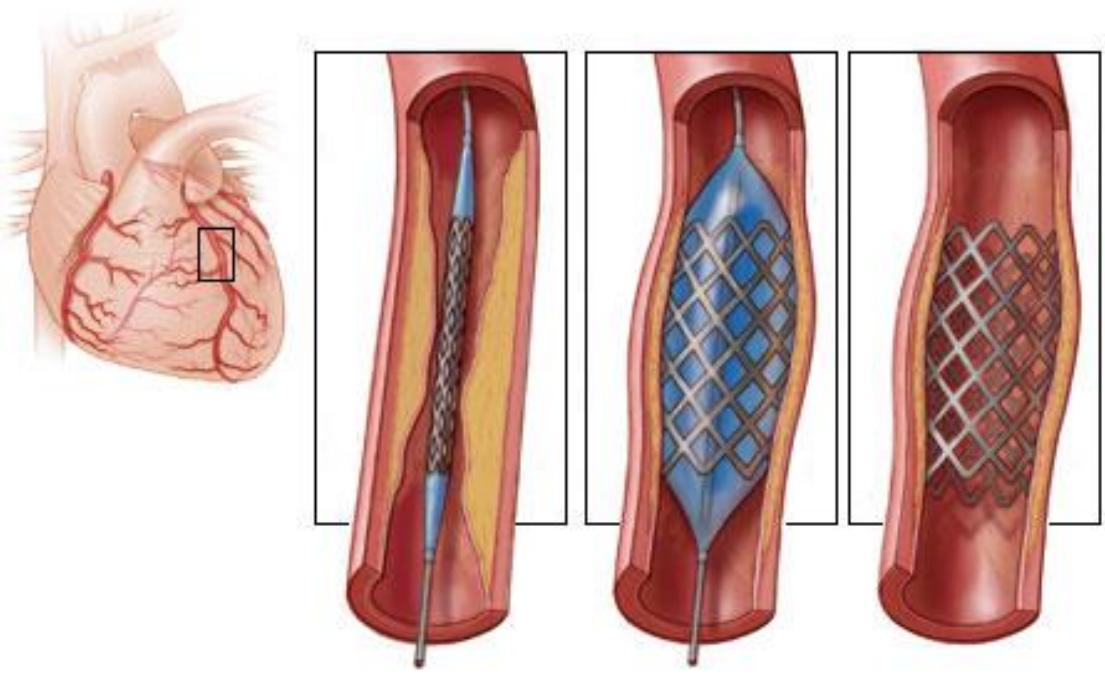

Figure 2. Stenting (angioplasty) procedure in a narrowed artery

Thus the stent should be fully compatible with the human body and its biological system since it is implanted permanently into the body. Implanting stents is becoming an increasingly more common, and effective procedure throughout the world, however the commercially available stents are not fully hemocompatible. Release of metal ion and thrombogenicity are the major problems with current stents. These stents also suffer less than satisfactory performance because they cause restenosis (narrowing of vessels), occlusion (sudden blockage of blood vessels) and stent-associated thrombosis [2].

Surface modification of the current stents could help to improve their blood compatibility. For example, stents coated with appropriate biomaterials last longer in a human blood environment. There are three categories of stents [4] including bare metals, covered metals, and drug eluting stents. Most stents are made of stainless steel and nitinol (nickel-titanium alloy). Those with a polytetrafluoroethylene (PTFE) covering on metal are called PTFE-covered stents which are superior to uncovered stents in some cases, especially in controlling the releasing of metal ions. However no significant difference was found in patient survival rates between groups receiving the PTFE-covered and uncovered stents [5]. Drug–eluting stents show a lower restenosis rate than the bare metal stents and they also delay the time of restenosis. However they still suffer from side effects such as delayed clotting and delayed restenosis. This happens after releasing all drugs into the blood and there is no drug to prevent restenosis.

Changing the surface properties by coating a stent with more blood-compatible materials is another possible approach to improving the hemocompatibility. Since amorphous carbon, known as diamond-like carbon (DLC), has biomaterial properties, depositing a DLC film on stents could lead to improved performance.

Chemical, mechanical, and morphological properties of DLC films may have a correlation with the biocompatibility of the films. Correlation between the optimum biocompatibility and these properties can be found by characterizing DLC films. These properties are helpful to find a surface structure with the best biomedical performance.

1.2 Objective

The Main purpose of the work presented in this thesis is to use plasma-enhanced coating techniques to improve the hemocompatibility of Polytetrafluoroethylene (PTFE), which is extensively used in cardiovascular implants. This research seeks to remedy the problems of existing PTFE stents, which cause early thrombosis. Depositing a thin film of nitrogen-doped amorphous carbon (a-CN) is a promising solution for improving the blood compatibility of PTFE.

The effects of nitrogen doping on PTFE coatings with amorphous carbon (a-C) thin film using hot filament plasma CVD and inductively coupled plasma (ICP) reactors have been studied. Samples made by these methods have been studied and compared. ICP has advantages such as lower temperature deposition which is suitable for PTFE with low melting point and less impurity was used in this work for DLC sputtering as a new technique.

Recent developments in the field of material characterization techniques have led to a renewed interest in producing samples with properties similar to biomedical components that are exceptionally hard, have low friction and are bioinert. These and other biomedical properties can be tested by material characterization techniques. Sample characterization has been the decisive part of this research, investigating mechanical properties, morphology and chemical composition. Characterizing techniques used includes Scanning Electron Microscopy (SEM) and

Atomic Force Microscopy (AFM) for high-resolution surface investigation and roughness measurement. Raman spectroscopy has been used for phase analysing and X-ray Absorption Spectroscopy (XAS) is done for chemical and element analysis.

1.3 Materials used in this research

1.3.1 PTFE

PolyTetraFluoroEthylene (PTFE) is a class of plastics referred to as fluoropolymers. A polymer is a repeating structure of a mixture of compounds. PTFE is produced after polymerization of TetraFluoroEthylene (TFE), which is a colorless, odorless gas with the formula C_2F_4 [6]. Thus the PTFE is poly (many) of TFE with the chemical formula $(C_2F_4)_n$:

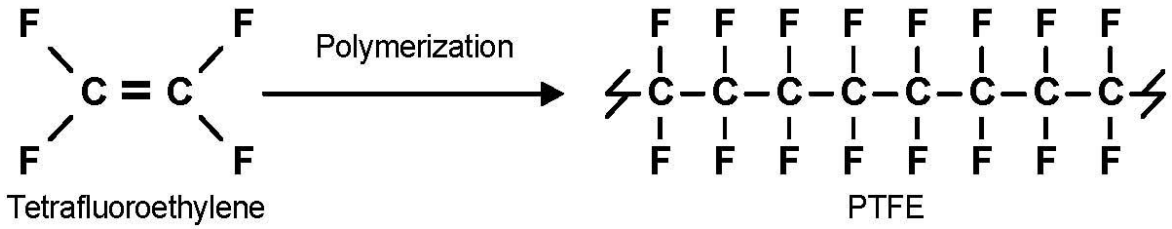

PTFE is also known by the famous brand name "Teflon." It has a relatively high melting point of 327° C, low friction, and is also extremely chemically inert and corrosion resistant; consequently it is barely dissolved by other materials. Moreover, PTFE is hydrophobic: It repels water and water containing substances. These properties make PTFE an applicable biomaterial. Thus it is used in biomedical implants either as a lubricant to reduce wear in metal prostheses such as hip joints or as a coated material on the surface of cardiac implants to improve the biocompatibility properties [7].

Fluorine atoms are located around the long chain of a PTFE molecule in a way that it looks like a firmly twisted rubber as shown in Figure 3 [8]. Since the carbon–fluorine bond is exceedingly strong and its outer shell is complete, PTFE is remarkably inert and stable [8].

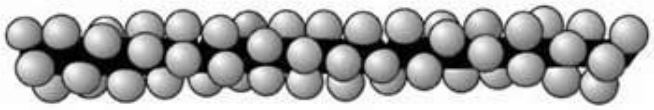

Figure 3. PTFE molecule

PTFE sheets are prepared commercially by different methods. In this research, PTFE samples with various thicknesses have been used as substrates, as shown in Figure 4. There are both skived and sintered-extruded sheets used as substrates. Sintered-extruded PTFE, which is used the most in this project, is provided from the company named SAINT GOBAIN.

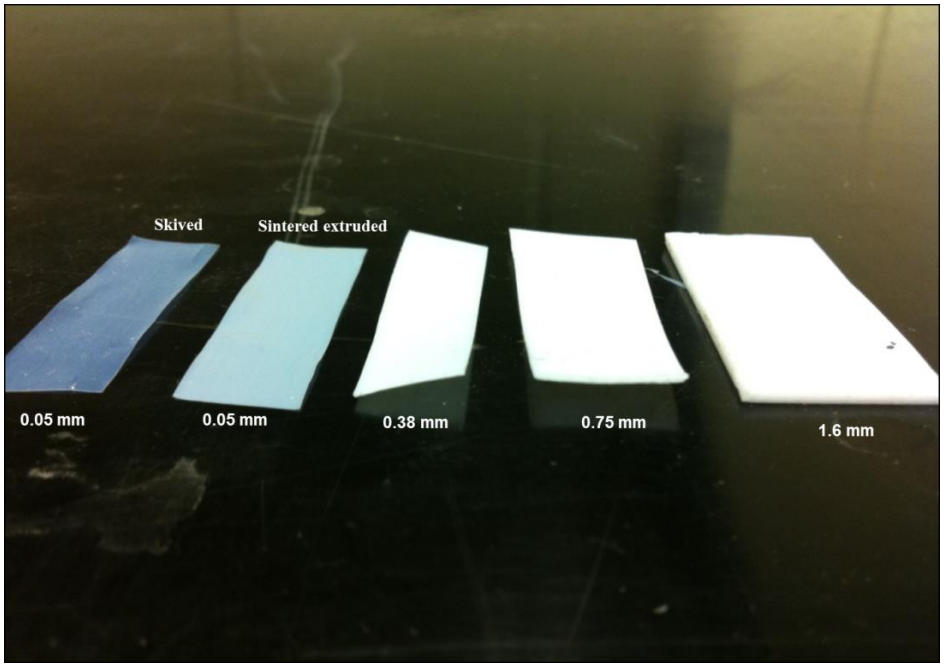

Figure 4. Images of PTFE substrates with various thicknesses from 0.05 mm to 1.6 mm

1.3.2 Carbon

One of the most interesting elements in the periodic table is carbon. It is an abundant chemical element in nature and almost 90% of all chemical substances contain carbon. Human bodies contain a large (18%) carbon mass, the second largest in the body next to oxygen (65%). Thus, it is one of the basic elements for life and is also widely used in industry. Furthermore, it plays the main role in synthesis of a thin coating of diamond and diamond-like carbon. One of the characteristics of carbon is its capability of making bonds and combining with other elements. The electronic structure of carbon is the reason for its unique behaviour. Carbon has 6 electrons in the $1s^2$ $2s^2$ $2p^2$ orbitals. The electron configuration of a carbon atom in its ground state (lowest energy state) is illustrated in Figure 5 [9].

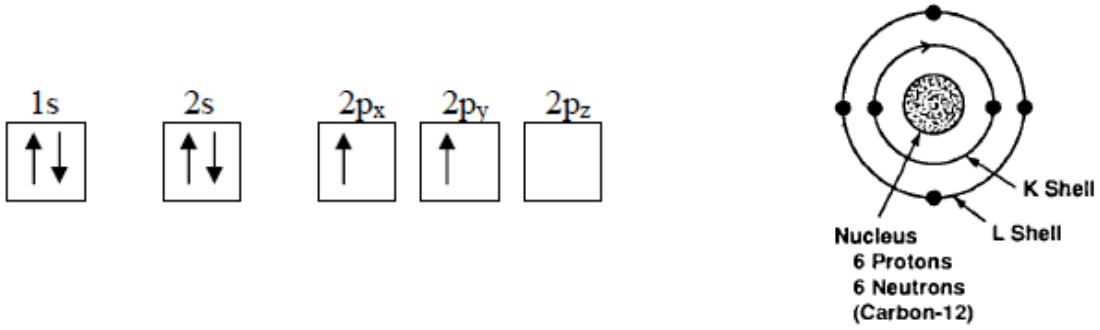

Figure 5. Electron distribution in the carbon orbitals

This electron distribution allows carbon to form various allotropes because it can have three bonding configurations. Carbon may form a single, double or triple bond. The bonding can take place only with valence shell electrons and they can be found in the incomplete outermost shell. Thus in the ground state it can form two bonds. In the process called hybridization, by promoting one of the 2s electrons to the empty p orbital, carbon would be able to form 4 bonds. In this

excited state carbon is relatively stable, since both the 2s and 2p subshells are half full. Carbon hybridization introduces three cases: sp, sp^2, and sp^3. In sp^3 one of the electrons in the 2s subshell is promoted to the higher orbital 2p as illustrated in Figure 6-a. The new orbitals, which are the combination of 2s and 2p orbitals, are called hybrids and labelled sp^3. These are also known as tetragonal hybrids because the orientation of the bonds forms a tetrahedron with equal angles of 109.28°. In addition, the hybrid orbitals are made only in bonding with other atoms and are not formed in a free carbon atom. Carbon bonding is covalent, and since four of the six electrons of carbon contribute to bonding, there are strong covalent bonds in sp^3 hybrids. By convention, these sp^3 bonds are called sigma (σ) bonds. As an example, diamond forms the sp^3 hybridization in its structure. Diamond contains metastable tetragonal sigma (σ) bonds with extremely high hardness, thermal conductivity, refractive index, band gap, atom density and low wear rate [10]. Figure 6-b [10] shows the crystal structure of diamond. Applications of diamond are found mostly in the industries where ultra-hard tools are needed or scratch resistant material is required [9].

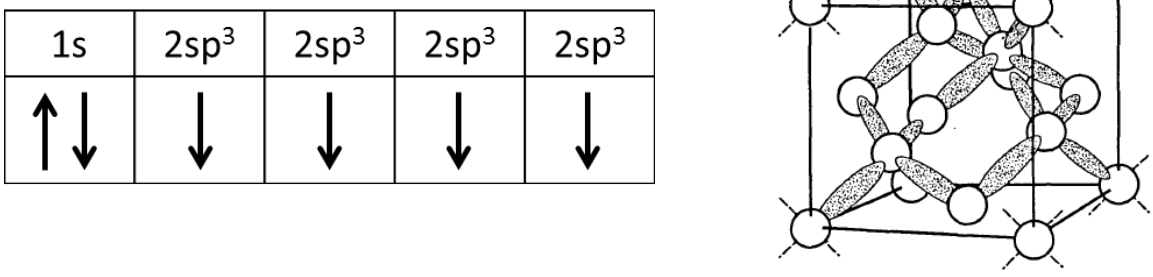

a b

Figure 6. a) sp^3 hybrid orbitals. b) 3D representation of sp^3 covalent bonding (diamond structure)

Hybridization of sp^2, which is the basic structure of graphite, is formed when one of the 2s electrons is promoted to 2p orbitals where an unhybridized p orbital is left delocalized. Thus, as illustrated in Figure 7-a, there are three sp^2 orbitals and one 2p delocalized electron. The three sp^2 are in the same plane and, as they are identical, the bonds are oriented with a 120° angle from each other as shown in Figure 7-b [10]. As a result, they form a trigonal shape and the unhybridized p electron is connected perpendicularly to the trigonal plane. This delocalized p electron would be able to form a pi (π) bond with other atoms. Layers of graphite are connected to each other by these pi (π) bonds. An sp^2 bond is covalent and called a sigma (σ) bond as well as sp^3. The sp^2 bonds are formed with higher energy and shorter bond length than sp^3 bonds. Graphite is the best example of the sp^2 carbon bonding. The trigonal crystal structure of graphite can be seen in Figure 8 [9]. Each plane of graphite is called graphene and these planes are connected to each other by pi (π) bonds formed by the weak van der Waals forces.

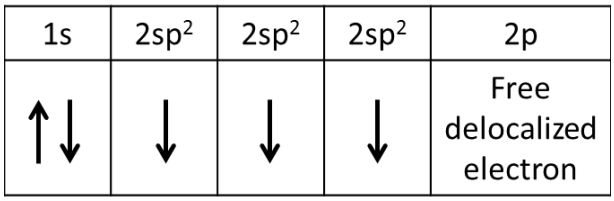

a

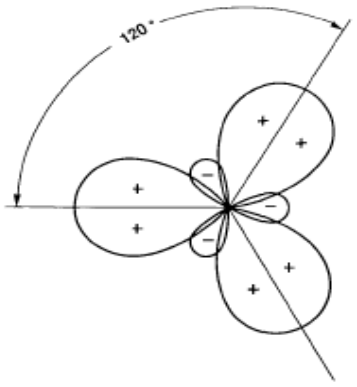

b

Figure 7. a) sp^2 hybrid orbitals. b) Planar section of the sp^2 hybrid orbitals of the carbon atom

Unlike the diamond, this material is soft and optically opaque. It has a high wear rate and low coefficient of friction. Graphite has uses in electrical applications, since it is an electric conductor. It is also used as a component in lubricants, electrodes, batteries and pencil

production. The last hybridized orbital is the sp orbital. It is a linear molecule known as a diagonal orbital. It forms a 180° angle between the sigma (σ) bonds. In this case there are two unhybridized p electrons, which can form pi (π) bonds [11]. An example of sp orbitals is acetylene, as can be seen in Figure 8.

Moreover, carbon can be found in other forms such as fullerenes (C60, nanotubes), in addition to graphite and diamond mentioned, and even amorphously. Buckminsterfullerenes, which are ball-shaped spherical lattices with 60, 70, and 540 carbon atom in C60, C70, and C540 respectively, were discovered in 1985. C60, as illustrated in Figure 9-a [12], contains both hexagonal and pentagonal structures. It led to the discovery of other types of fullerenes such as carbon nanotubes (CNT) in the 1990s. CNT, which is shown in Figure 9-b, is a tube form of a fullerene whose diameter is a few nanometers [10].

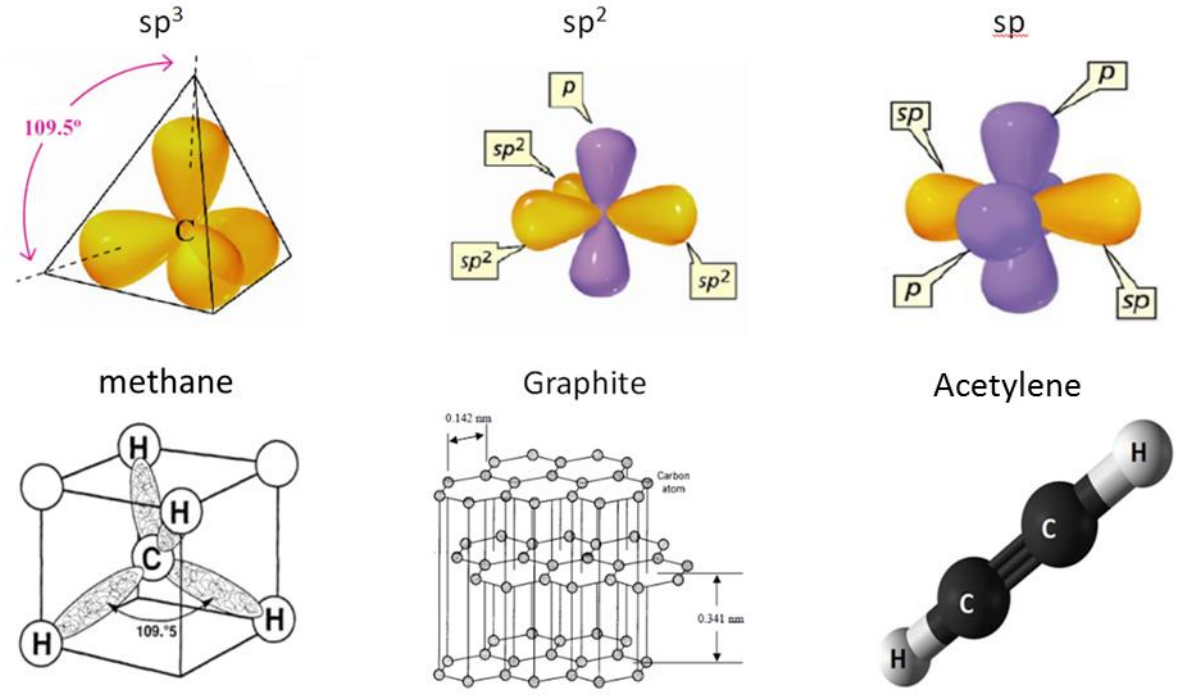

Figure 8. Summary and graphic visualization of sp^3, sp^2, sp hybridization with an example of each

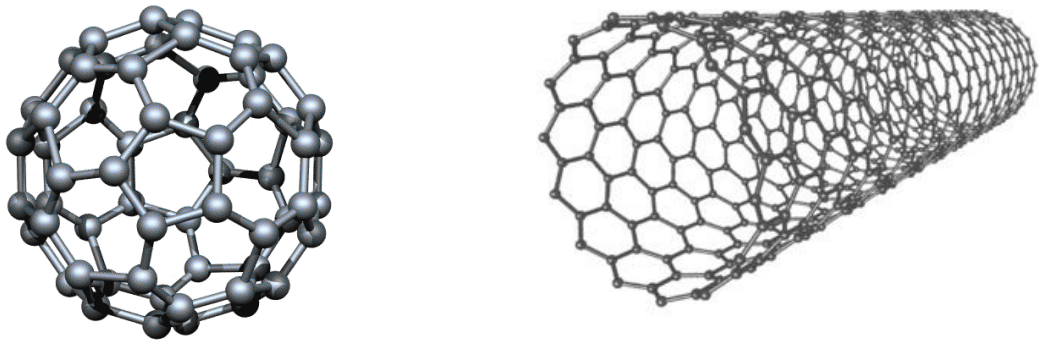

Figure 9. Fullerenes structure a) C60. b) single tube CNT

1.4 Thesis organization

This thesis consists of five chapters. Chapter 1 is a brief introduction and objectives of this project. Materials used in this thesis are also introduced in this chapter. Chapter 2 introduces the plasma and its applications for thin films deposition. Diamond-like carbon and different methods for producing it is also described in Chapter 2. Chapter 3 presents and compares the experimental setups used in this research. Chapter 4 is devoted to characterization of the samples with XRD, SEM, AFM, Raman, XPS, XAS, and XES. A brief description of each technique is given followed by experimental details, results, and discussions. Major findings made in this project are summarized in Chapter 5 with suggestions for future work.

CHAPTER 2

PLASMA AND DIAMOND-LIKE CARBON

2.1 Plasma

The word “plasma” comes from the Greek word meaning “something molded” and introduced by Irving Langmuir with an experiment on gas discharge in 1929 [13]. There are few definitions for plasma and they all explain the same issue. Plasma is matter heated to more than its gaseous state. Plasma is an ionized gas including electrons, ions, charged molecules and neutral particles. However, it has charge neutrality. Ionization occurs when the matter has absorbed enough energy (heat) to strip off at least one electron, thus, creating positive ions in the process. In fact, plasma is known as the fourth state of matter since its properties are quite different from those of solids, liquids or gases. Unlike ordinary fluids, the temperature of different particles (ions, electrons, and neutrals) may not be the same in a plasma since they may not have enough interaction to equalize the temperature. In other words a plasma is not necessarily in thermal equilibrium, and the velocity distribution of different kinds of particles may not have the same Maxwellian distribution at all. Plasma is divided into two categories: “Hot” and “Cold”. Electron temperature (T_e) in a cold plasma would have to be at least 10,000° K to have enough energy to overcome the binding energy between ions and electrons [14]. The hot plasma is almost fully ionized and it is often in thermal equilibrium. It is more common to show the temperature in eV instead of degrees. An electron gets 1 eV of energy (temperature) when it moves across an electric potential of 1 volt. Each eV is equal to 11,600°K in terms of temperature. For instance the electron temperature (T_e) of fluorescent lights is T_e = 1–2 eV. Plasma is also be characterized by a charged particle density ($n_e \approx n_i \approx n$ particles/m^3 for singly charged ions). Aurora, solar wind

and comet tails are examples of plasmas in nature, and artificial plasmas, such as laboratory gas discharges, are usually generated by electric fields. The electric field is applied to the free electrons, which play the main role in ionization. On the other hand, the heavy ions lose their energy in their collisions with neutrals or ions. Thus, cold plasmas are not in thermal equilibrium ($T_e >> T_i$) [15].

2.2 Role of plasma in material processing

Surface processing is one of the most important applications of plasma in industrial applications. For example, plasma discharges are used for modifying surface properties of materials in a unique way. Plasma processing is indispensable for surface engineering industries. Such processes have been used in developing electronic devices (integrated circuits), aerospace industries (airplane turbine blades), automotive parts, biomedical devices (cleaning and prostheses), etc. Producing diamond films and amorphous silicon for solar cells is also possible by exploiting the plasma processing properties. Moreover, its applications extend to implanted hip joint hardening, surface cleaning of different parts of industrial machines to extend their lifetimes and to many other areas [15]. Etching, depositing, sputtering, implanting and ashing are the related techniques that are possible only in plasma chambers, especially for microelectronics chips. Conventional chemical methods are not comparable with these plasma processing techniques in which the working scale is a few nanometres. Generally, cold (T_e = 1–10 eV) and weakly ionized ($n_i = 10^8$–10^{13} cm^{-3}) plasma in low pressure (P ≈ 1 mTorr – 1 Torr) are used for processing. Electron temperature is much higher than ion temperature, which means that the ions and neutral gas are not in the local thermal equilibrium state and the electrons are the particles that carry out the ionization and dissociation and generate free radicals [15]. Moreover, the energy distribution function of charged particles in a plasma is not necessarily Maxwellian, since

the charged particles are not dense enough to produce enough collisions. Fully ionized and high temperature plasma, is not ideal for plasma processing because of the lack of free chemical radicals [16]. Chemically active radicals are crucial in plasma-based material processing, since the chemical reactions would be enhanced by these free radicals, which require high electron temperatures to be created. On the other hand, the temperature of the much denser neutral particles is very low, preventing unwanted heating of the substrates. To maintain the quasi-neutrality ($n_i = n_e$) of a plasma, a thin layer sheath would be formed to isolate the plasma from the boundary. There is a drop in electrical potential in the sheath that causes repellence of the electrons and prevents electron loss to the wall of the plasma. This may balance the density of the electrons and ions and help to maintain the plasma [14].

There are various plasma sources for plasma processing, including DC discharges and RF (radio frequency) discharges. The commonly seen plasma sources include glow discharges, capacitively and inductively coupled plasma sources in RF and microwave frequencies, dense plasma focus, arc discharges, etc.

2.3 Amorphous carbon (a-C)

The amorphous form of carbon is also available and plays the main role in this thesis. Amorphous carbon (a-C) has no long-range lattice order. Diamond-like carbon (DLC) is a metastable form of amorphous carbon with a variety of fractions of sp^3 and sp^2 carbon hybridizations [17]. Although it may be true that DLC is an amorphous carbon, it is not a completely perfect amorphous such as glass. In fact, it has some small degree of crystallinity, which can be either in sp^3 or sp^2 forms. Nevertheless, they are small enough to not be detected by electron diffraction patterns. Therefore, in general, DLC is considered to be an amorphous

carbon [10]. The schematic structure of DLC is shown in Figure 10 [18]. Unlike the diamond, DLC is not made by itself in nature. It can be produced as a thin film in low pressure by energetic ions in a deposition process. The name "diamond-like" came from the diamond properties associated with the sp^3 bonds. DLC is not a specific material, but a group of materials with different characteristics, which vary by different concentrations of sp^3 and sp^2 bonds. Generally, diamond-like properties increase by growing the carbon-carbon (C-C) sp^3 fraction. For example, mechanical hardness, optical transparency, and low friction are the features that can be reinforced in DLC with more C-C sp^3 bonds [19]. DLC with a large amount of sp^3 is called tetrahedral amorphous carbon (ta-C). DLC can only be produced as a thin coating, since its internal compressive stress is high. Thus, characteristics and properties of the DLC are dependent on the substrate. DLC is divided into two main categories [10]:

1) Amorphous DLC or amorphous carbon (a-C). The a-C or hydrogen-free DLC is produced by the PVD (physical vapour deposition) process. Sputtering with a solid carbon (graphite) target is the main process, which can be done by ion beam, laser, and glow discharge to produce hydrogen-free DLC. This kind of DLC is produced and studied in my research and the processes will be discussed later.

2) Hydrogenated DLC (a-C:H or H-DLC). Hydrogen can be involved in the DLC structure and forms a hydrogenated amorphous carbon. To produce Hydrogenated DLC, the carbon source is a hydrocarbon gas such as methane instead of the graphite or the other solid carbon targets in a PVD-CVD (chemical vapour deposition) process [10].

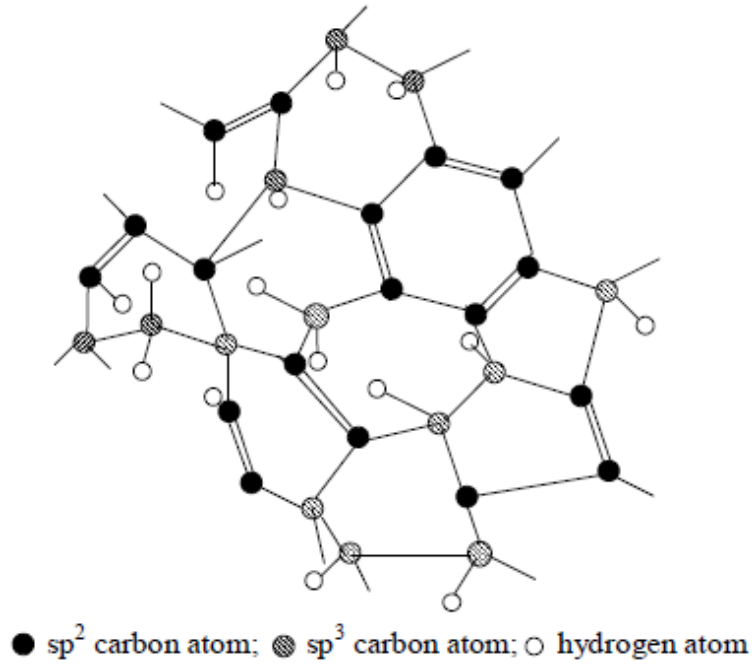

Figure 10. A two-dimensional representation of diamond-like carbon film structure

The sp^3 bonding can be produced by energetic ions in a deposition process. Different ratios of sp^2 to sp^3 correspond to materials with different characteristics, and these materials vary from graphite-like sp^2 hybridization to diamond-like sp^3. In 1993, Jacob and Moller [20] expressed the DLC composition on a ternary diagram. They compared published data by marking the reported concentrations on this ternary diagram as shown in Figure 11-a. The data are normalized and the proportions of all three phases (sp^2, sp^3, and H) sum to 100%. Close to the hydrogen-rich corner (more than 60% hydrogen), no stable film is reported to form. In the left side of these ternary diagrams we see the area between sp^2 and sp^3 which is tetrahedral amorphous carbon (ta-C) and this is the group of amorphous carbon with a high C-C sp^3 content. Sputtered, hydrogenated, and nitride films are clearly individuated in ternary diagrams. Different parts in the diagram are also distinguished by deposition methods including PLD (pulsed laser deposition), FCVA (filtered cathodic vacuum arc), MSIBD (mass-separated ion beam

deposition), ECWR (electron cyclotron wave resonance), PECVD (plasma-enhanced chemical vapour deposition), and graphite sputtering. Hence, one can predict the sp^3/sp^2 ratio of the film produced by a specific method. For example, sputtered a-C has sp^3 bonded carbon (10–30 at. %) less than ta-C, which is produced by filtered cathodic vacuum arc (FCVA) and mass selected ion beam deposition (MSIBD). Increasing nitrogen content (Figure 11-b,c [21]) changes the structure of amorphous carbon and compositions of carbon nitrides. For example, increasing N content is followed by increasing disorder and sp^3 content in a-C:N, and decreasing sp^3 content in a-C:N:H films.

2.4 Classification of diamond-like carbon

Casiraghi *et al*. [22], based on the ternary diagram (Figure 11-a), classified the hydrogenated amorphous carbons into four kinds:

(1) Polymer-like amorphous carbon or a-C:H with the highest H content (40-60 at. %). Plasma enhanced chemical vapour deposition (PECVD) at low bias voltage is the common method for providing these kinds of film.

(2) Diamond-like hydrogenated amorphous carbon or a-C:H with medium H content (20–40 at. %). Although overall sp^3 content of these films is less than the first group, C-C sp^3 bonds are superior. Electron cyclotron resonance (ECR) and PECVD are the common methods for producing these films.

(3) Hydrogenated tetrahedral amorphous carbon (ta-C:H). These films have the highest sp^3 content among the hydrogenated amorphous carbon films, while the hydrogen content is about 30%. High density plasma sources, such as electron cyclotron wave resonance (ECWR) and plasma beams, are the reported methods for ta-C:H coating.

(4) Graphite-like a-C:H which has less than 20% hydrogen and mostly sp^2 bonding. Magnetron sputtering and PECVD at high bias are used to deposit the graphite-like a-C:H.

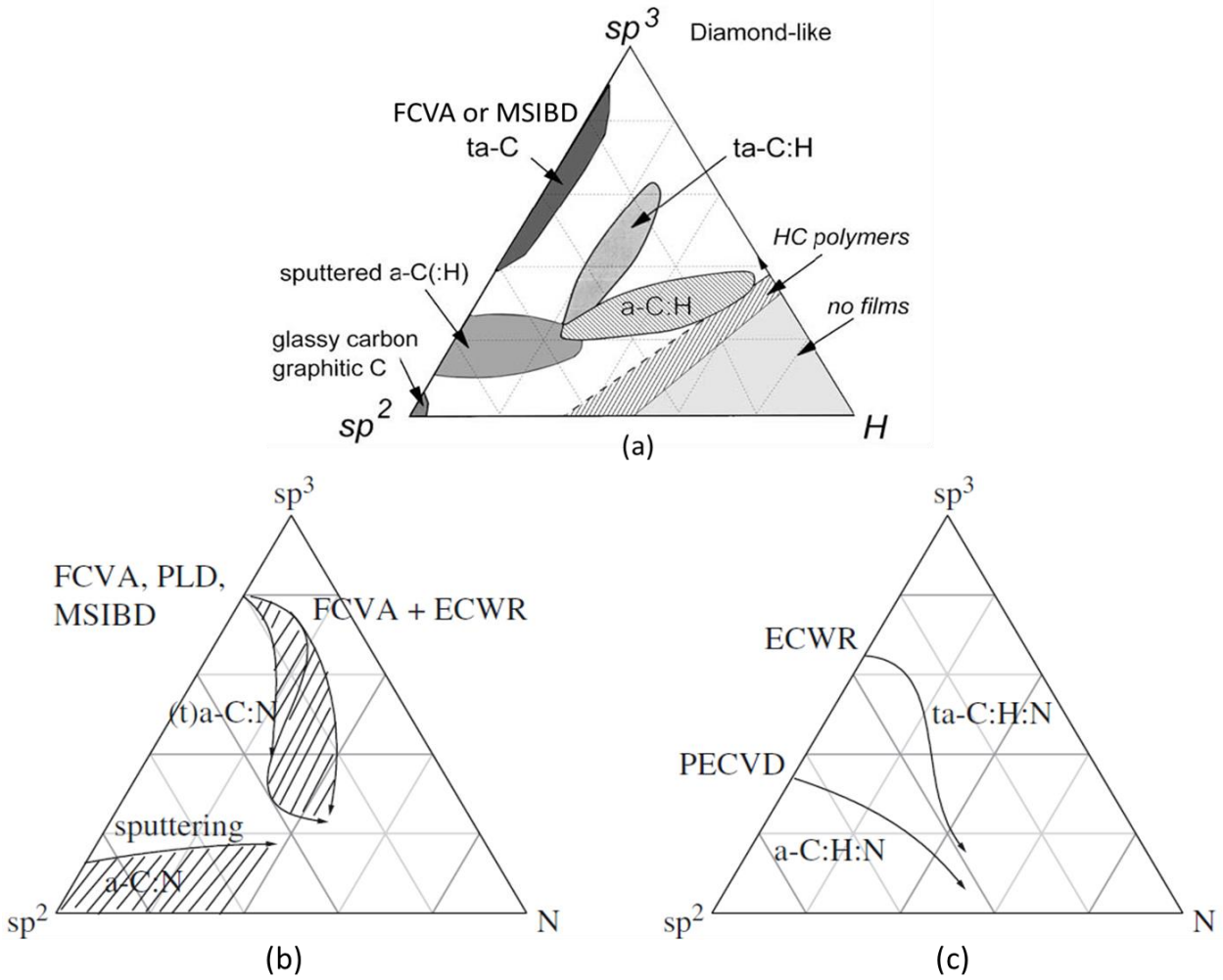

Figure 11. Ternary phase diagram of a) amorphous carbon-hydrogen alloy, b) amorphous carbon-nitride alloy without hydrogen, c) amorphous carbon-nitride with hydrogen

As can be seen in Figure 11-b,c, carbon nitride films are also divided into four main classes [22]: (1) amorphous carbon nitride (a-C:N). These films have high sp^2 content and the N content can reach up to 35%, while the sp^3 fraction increases slightly. These films are produced in a

hydrogen-free atmosphere and the carbon source is provided by sputtering a graphite target. Nitrogen can interact with carbon atoms either directly by nitrogen ion beams or by nitrogen doping to the plasma discharge.

(2) Tetrahedral amorphous carbon nitride (ta-C:N). These films need a high-density plasma in order to be deposited. Mass selected ion beam deposition (MSIBD) and filtered cathodic vacuum arc (FCVA) are the suitable techniques for producing these films. Increasing N content is followed by a rapid decrease of sp^3 bonding and clustering sp^2 bonds.

(3) Hydrogenated amorphous carbon nitride (a-C:H:N). A mixture of nitrogen and hydrocarbon gases is used in a PECVD process for preparing these films. Unlike the a-C:N, sp^3 content decreases by increasing nitrogen in these films, but the decreasing trend is not as fast as those in ta-C:Ns.

(4) Tetrahedral hydrogenated amorphous carbon nitride (ta-C:H:N). Like ta-C:N, low pressure and high density plasma is needed for depositing these films.

Figure 12 [23] indicates how sp^2 groups change from ring to chain configuration as the figuration changes from ordered graphite to nanocrystalline graphite, then to amorphous carbon and finally to sp^3-bonded tetrahedral amorphous carbon (ta-C). This evolution is the so-called amorphization trajectory. We also can see (Figure 12) the schematic evolution of sp^2 cluster size (L_a) and sp^3content. The percentage of sp^2 groups becomes smaller as the concentration of ta-C increases [23].

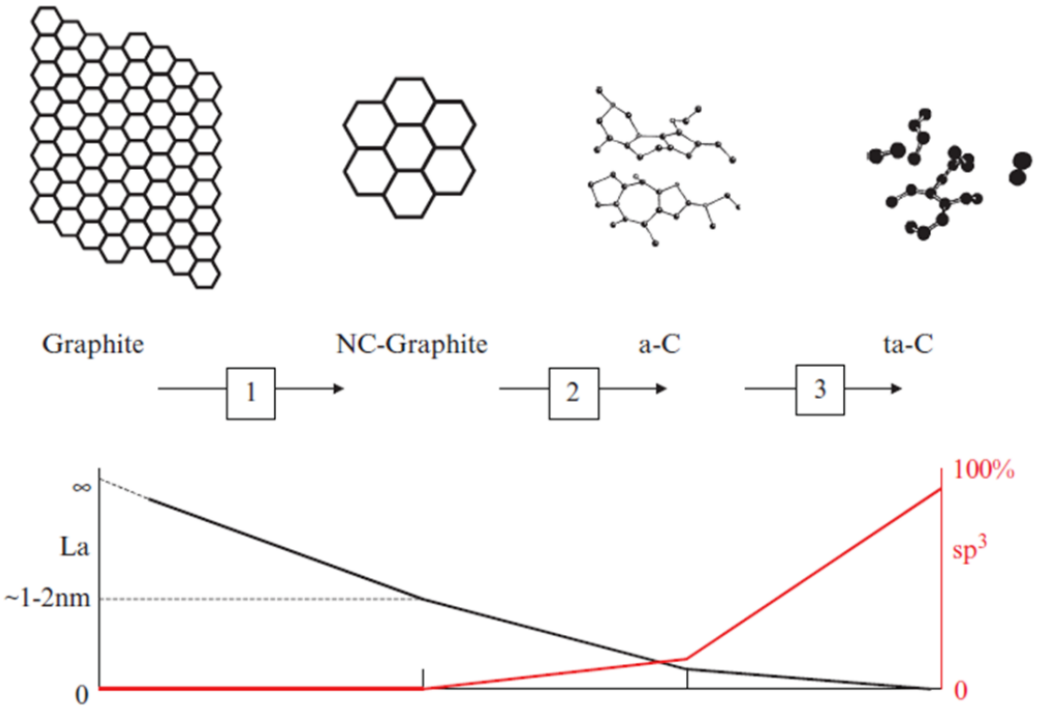

Figure 12. Amorphization trajectory: Evolution of sp^2 groups to sp^3, (L_a is the sp^2 cluster size)

2.5 Historical overview of DLC deposition

The first DLC coating was attempted in 1953 by Heinz Schmellenmeier [24], who made a black carbon film from Acetylene (C_2H_2) in glow discharge plasma. He mentions in his report that "if the current density is too small, a shiny black layer is formed on the cathode, which has initially great adherence but delaminates after hours or days… the layers were a few µm thick and…extraordinarily hard. With low loads of 10 and 20 g, the layer will not be attacked by a sharp diamond tip…this material is X-ray amorphous". It can be assumed that he produced DLC. However, it was left for Eisenberg and Chabot [25] in 1971 to (re-)discover the DLC. They developed an ion-beam deposition technique to produce insulating carbon films on room temperature substrates. They cite that the carbon films they made "have following characteristics similar to the carbon in diamond form: (1) transparent, (2) index of refraction greater than 2.0,

(3) highly insulating, (4) able to scratch glass, (5) resistant to hydrofluoric acid for long period of time, (6) at least partially crystalline and with a lattice constant similar to diamond…". Synthesizing DLC films continued in the mid 1970s by applying RF discharges in the presence of hydrocarbon gases [26]. Investigation on DLC films in 1979 revealed that the DLC has an amorphous structure [27, 28]. The 1980s was the era of finding some applications and characterising such films and a few papers were published about DLC thin films. Its application started with the thin film media and magnetic recording. It was predicted that the DLC could be used as a material for coating a magnetic recording medium [29, 30]. Incorporation of heteroatoms (N, O, F, Si, etc.) into the DLC structure was investigated in the 1990s. It has been found that incorporation of these atoms with amorphous carbons is able to change the structure and properties of the films in a desired way. During the last two decades, numerous papers and reviews have been devoted to synthesizing, characterizing, and developing industrial applications for DLC films. The number of publications on the subject of DLC has increased dramatically since 1990, and it is predicted that this trend will continue, since DLC is a big attraction to both scientists and industrialists [31].

2.6 Plasma assisted DLC deposition

Amorphous carbon has been deposited on different substrates by many techniques, but the films deposited by different methods reveal different mechanical and tribological features. Common DLC coating methods include sputtering [32], Plasma Enhanced Chemical Vapour Deposition (PECVD) [33], direct Ion Beam Deposition (direct IBD) [34], pulsed laser deposition (PLD) [35] and vacuum arc [36]. The plasma source would be chosen based on the intended applications. Each method is considered for a specific application and can have advantages and disadvantages. For example sputtering is an inexpensive technique with the disadvantage of low deposition rate.

Microwave plasma and inductively coupled plasma (ICP) with higher plasma densities (10^{11}–10^{12} cm^{-3}) can provide a higher processing rate. RF capacitive discharge suffers from electrodes contamination and its plasma density is less than those of microwave and inductively coupled plasmas. Moreover, the $sp^3/\ sp^2$ ratio is different in each technique with the highest ratio being achieved in direct ion beam deposition and the lowest in RF sputtering [37]. Graphite sputtering is commonly used in industrial applications [38]. Sputtering in the absence of hydrocarbon gases is the preferable method for hydrogen-free DLC coating. Hot filament or magnetron sputtering can be used in order to increase the deposition rate of the sputtered graphite. For plasma-assisted deposition, plasma density of 10^9 cm^{-3} is needed to achieve a high enough deposition rate. Thus, the glow discharge regime can be used for plasma sputtering in DLC coating [8, 39]. Figure 13 [40] illustrates the current-voltage diagram of plasma discharge in three discharge regimes.

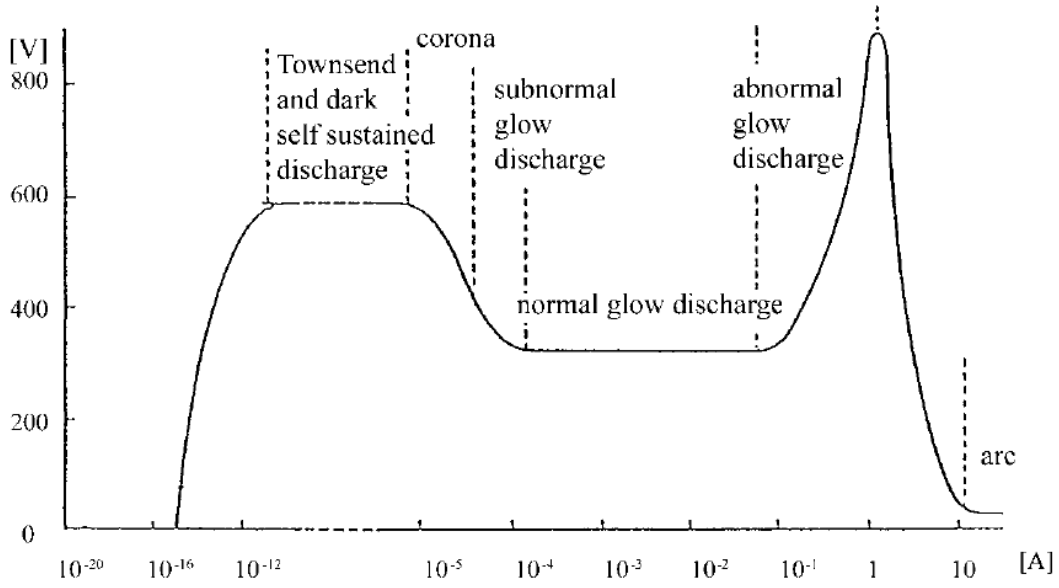

Figure 13. Typical current-voltage diagram of various kind of plasma DC discharges (Ne, 1.3 mbar, flat copper electrodes 10 cm^2 electrode distance 50 cm)

Sputtering is one of the most inexpensive methods for deposition of DLC. In this technique graphite is used as the cathode or sputtering target and Ar plasma is produced by DC or RF discharge. Ion bombardment on the substrate is necessary for formation of sp^3 bonds. A sputtering chamber can have different applications. Many materials can be used as cathodes and be deposited. This versatility plus the simple mechanism and controllable coating conditions, make this method popular in industrial applications [41].

2.7 Nitrogen as a dopant

Incorporation of other elements such as N, O, F, and Si offers improvement in DLC mechanical, tribological and biological properties [42]. It has been demonstrated that nitrogen-doped DLC results in reducing intrinsic stress of the films [43]. It also has been found that doping nitrogen could enhance and stabilize the diamond sp^3 bonds in the DLC structure [44]. Figure 14 [45] shows the possible configurations of nitrogen bonding. Nitrogen can form bonding similar to carbon, since it has 3 valence electrons and one non-bonding electron (lone pair). Nitrogen atoms may form pyrrole, nitrile, or pyridine as shown in Figure 14. Moreover, it can form sp^3 and sp^2 bonding with carbon by substituting for one of the carbon atoms. Thus they can form C=N and C≡N. Nitrogen doped DLC has been investigated since 1990, however, since DLC is a broad class of materials and not a unique material, nitrogen doped DLC has not yet been fully understood.

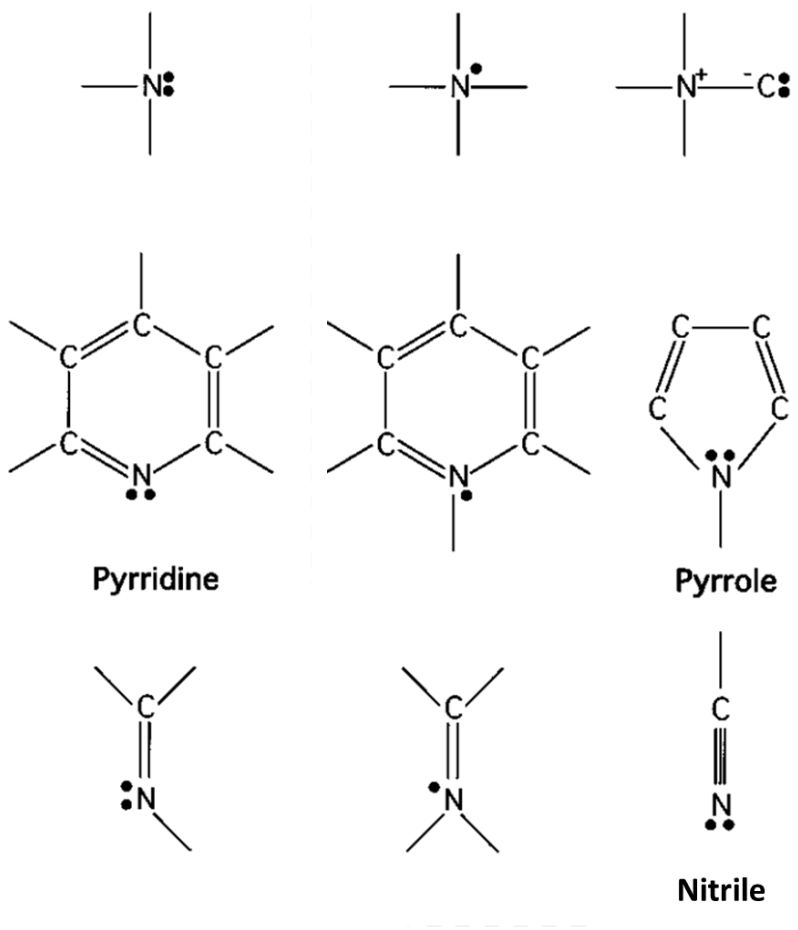

Figure 14. Various nitrogen configurations in a-C and possible doping configuration: (One dot means an unpaired electron and two dots mean a lone pair)

CHAPTER 3

EXPERIMENTAL SETUP

3.1 Hot filament chemical vapour deposition (HFCVD)

3.1.1 Introduction

Chemical vapour deposition (CVD) is the deposition of desired solid material from one or a group of gases. Deposition happens through activation of chemical reactants of gases in the vicinity of a substrate. CVD is widely used for coating thin films in various applications and it is one of the most common methods for coating [46].

The first diamond thin film was produced by Eversole [47] using CVD technique in 1958 and patented in 1962. He grew diamond films on diamond crystals by decomposition of hydrocarbon gases. In 1982, Matsumoto *et al*. [48] introduced thermally activated CVD for the diamond growth using a hot tungsten filament CVD device. They passed a mixture of hydrocarbon and hydrogen gases through a reaction chamber where a hot filament was installed above the substrate.

Two common metals used as the filament are tungsten (W) and tantalum (Ta). They both have very high melting points and emit electrons thermionically. The tungsten filament was used in this research.

In this research projects an HFCVD chamber was used to deposit DLC on PTFE and Si substrates. However, argon and nitrogen were used instead of hydrocarbons and hydrogen gases, since the goal of this project is studying the hydrogen-free amorphous carbons and the films needed to be grown in a hydrogen-free atmosphere.

3.1.2 HFCVD reactor and hydrogen-free plasma sputtering setup

Although CVD is an ideal method for synthesizing a diamond-like coating, the DLC that is made by CVD is hydrogenated amorphous carbon (a-C:H). H-free DLC can be produced by plasma sputtering in the absence of any hydrocarbon and hydrogen gases. Thus, hot filament plasma with sputtering capability was used for this research to deposit H-free DLC on PTFE and Si substrates. Figure 15 illustrates the schematic of the hot filament plasma-sputtering device used in this project.

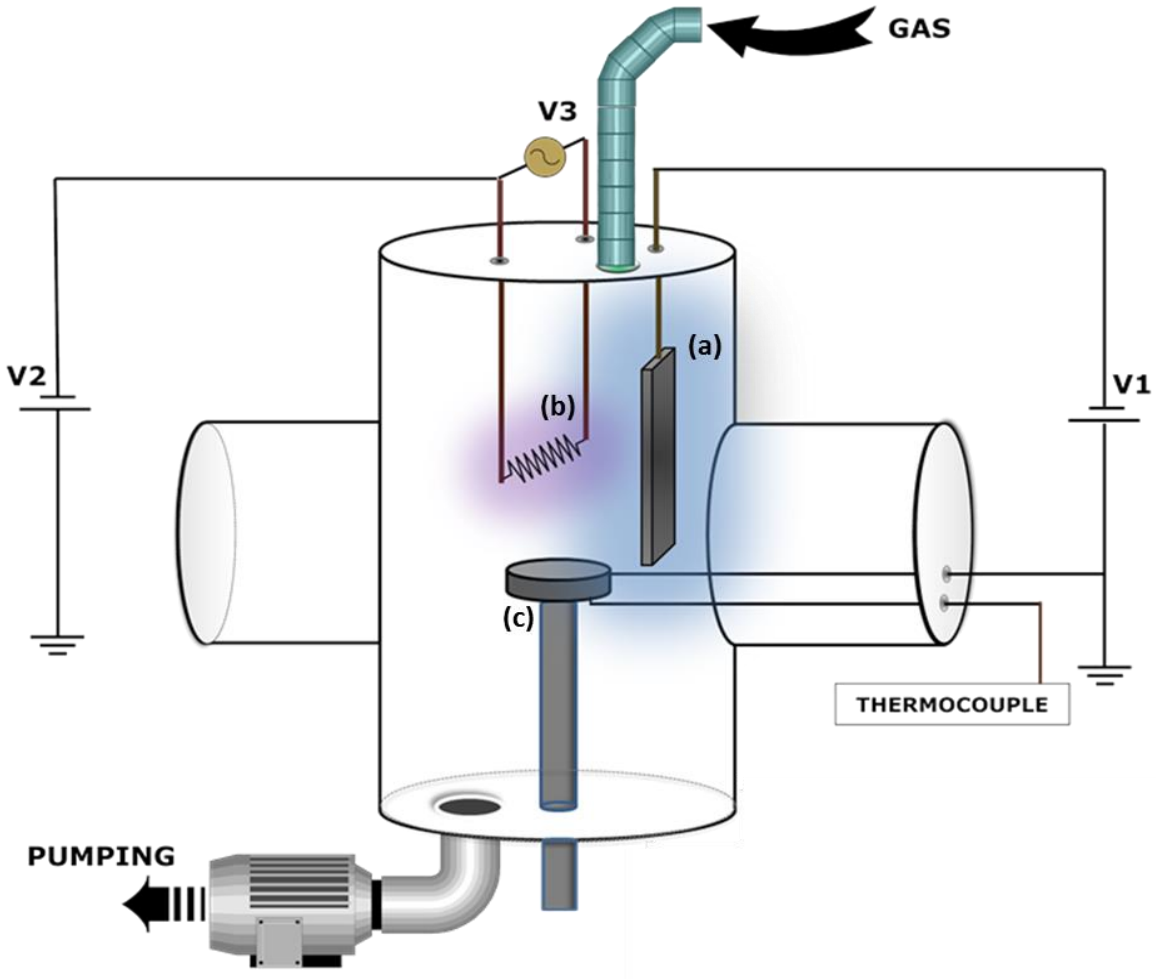

Figure 15. Schematic of hot filament plasma sputtering system.(a): graphite target, (b): hot filament (c): substrate holder

This homemade device is located in the Plasma Physics Laboratory. The graphite plate is the sputtering target and it is connected to a negative DC voltage (V1 in the diagram) power supply. The graphite plate is 15 cm long, 2.5 cm wide and 2 mm thick. There is a circular and grounded substrate holder that is made of steel. The height of the holder, or the distance between the hot filament and substrate, is adjustable, allowing for control of the substrate temperature. A thermocouple is placed under the substrate holder to monitor the temperature of the substrate. A 22 cm long coil of tungsten wire, 280 μm in diameter, has been used as a filament that is heated by an AC power supply (V3 in Figure 15). The voltage between the filament and the substrate holder (V2) is minus 40 V, which maintains a desired glow discharge current. Argon (Ar) has been used as working gas for plasma and nitrogen (N) gas is admitted to the chamber as a dopant. A roughing pump and a diffusion pump are used to achieve a base pressure of 1×10^{-4} torr. Table 1 shows typical discharge parameters used in the experiments.

Table 1. Optimized condition in HF sputtering,
T is the temperature of the substrate, P is the working pressure in the chamber, BP is the base pressure in the chamber, GFR is the gas flow rate (it can be changed by gas flow controller), and D is the distance between the filament and the substrate holder.

V1(DC)	I1(DC)	V2(DC)	I2(DC)	V3(AC)	I3(AC)	T	P	BP	GFR	D
- 800 V	200 mA	- 40 V	1 A	28 V	8 A	180-210 C°	100-200 mTorr	0.1 mTorr	20 sccm	7 cm

The mechanism of hot filament plasma sputtering is simple and well understood. The filament emits electrons through thermionic emission. These electrons are accelerated in the fields established between the filament and substrate holder, collide with argon atoms and ionize them. Electrons with sufficient energy can ionize Argon atoms by stripping their shell electrons. A bias voltage of -800 V applied to the graphite target (cathode). Ions, because of their positive charge,

will be accelerated to the negatively biased cathode (graphite plate) and cause sputtering. The secondary discharge between the graphite target and the grounded substrate and the slightly negatively biased filament also ionize more gases and produce more plasma. The sputtered graphite becomes the source material for the DLC film to be deposited on the PTFE substrates. During these interactions, the cathode atoms are sputtered and deposited on the grounded substrate [8]. Figure 16 illustrates the interactions inside the chamber.

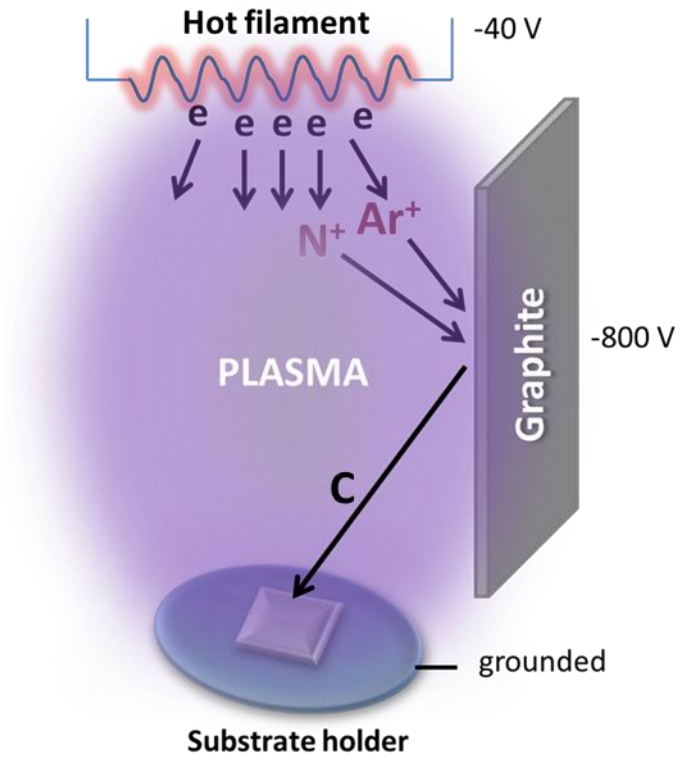

Figure 16. Schematic of interactions inside the chamber

Nitrogen gas was also added to the chamber as dopant to study the effect of doping. Thus, samples of PTFE coated with a-CN are labeled HCN_X where H indicates that the sample is produced in the hot filament (to distinguish between these and the samples made by inductively coupled plasma to be discussed later) device and x is the nitrogen gas flow rate percentage

concentration introduced into the chamber (Table 2). All parameters were kept the same as listed in Table 1 except minor variations of the pressure and temperature, which are affected by the amount of nitrogen added to the chamber. The total gas flow rate was fixed to 20 [SCCM] (Standard Cubic Centimeter per Minute) measured by a gas flow controller that can mix the gases at any desirable rate.

Table 2. Notation of samples coated in the Hot Filament device

label	HCN_0	HCN_5	HCN_{10}	HCN_{15}	HCN_{20}	HCN_{25}	HCN_{30}
N_2 concentration	0%	5%	10%	15%	20%	25%	30%

3.2 Inductively coupled plasma (ICP)

3.2.1 Introduction

Low-pressure high-density plasma (HDP) technology has been improved over the last two decades by industries making thin films, semiconductors and electronic devices. Inductively coupled plasmas (ICPs) as the high-density plasma (HDP) sources are commonly used in plasma processing and its related manufacturing process. Several attempts have been made to study inductively coupled plasma (ICP) over the last century. The first report about the electrode-less inductive discharge was provided by the German physicist, Johann Wilhelm Hittorf, in 1884 [49]. Many scientists tried to extend Hittorf's work but it was left for Babat [50] to give birth to ICP definition in 1947 and present the difference between capacitive discharges (E-discharges) and inductive discharges (H-discharge). Reed (1960) [51] explained the different methods for maintaining the argon, oxygen, helium, and air ICPs in an open vessel (torch). Figure 17 is the schematic and the picture of inductive plasma in a torch. In 1965 Stokes [52] theoretically

described the electromagnetic fields in a cylindrical ICP chamber and the planar coil ICP was introduced in the late 1980s. After that, ICP devices were proposed for plasma processing of semiconductor and electronic chips.

ICP is one of the most effective electrode-less plasma sources, since it has many applications, not only in materials science and the electronic chip industries, but also in atomic emission spectroscopy and mass spectrometric analysis [53]. Relatively high-density plasma and the tunable ion energy are the advantages of ICP. Moreover, it is simpler than other high-density plasma sources such as electron cyclotron resonance (ECR), which need a constant magnetic field.

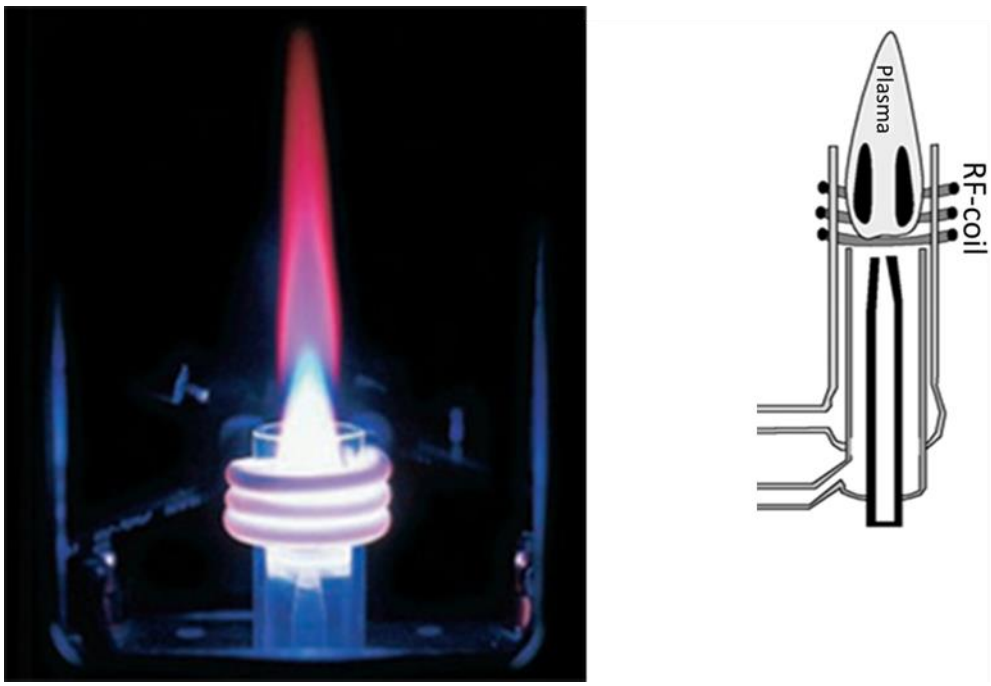

Figure 17. Schematic and picture of inductive plasma torch

3.2.2 RF glow discharge and basic principle of ICP

Inductively coupled plasma discharges are generated by a radio frequency (RF) current. The radio frequency (RF) range is 1 KHz–1 GHz. However, most of the RF generators operate at 13.56 MHz, which is the industrial standard for radio frequency. Compared to the DC glow discharges, RF discharges can operate at lower pressure and the plasma can be sustained, whereas the ions and electrons are continuously removed and lost by various collisions in DC discharges. The major losses happen when particles drift to the electrodes in DC discharges. On the other hand, RF discharges show significantly reduced losses. Thus, lower plasma potential is needed for maintaining the RF discharge [54] and the discharge is more efficient. Moreover, RF plasma can be operated by either conductive or nonconductive electrodes. Interaction of radio frequency with plasma can be performed either capacitively or inductively (Figure 18). They differ in the way that RF current is applied to the plasma. Hence, RF discharge can be classified into two categories: (1) E-discharge or capacitively coupled plasma (CCP), which arises from potential field, and (2) H-discharge or inductively coupled plasma (ICP), which is based on electromagnetic induction. In CCP the discharge occurs between two electrodes with the RF power transferred to the electrons by the electric field between the electrodes. On the other hand, ICPs transfer RF power through ohmic dissipation of induced current in plasma [55]. The electron density in CCPs is in the range of 10^{9} –10^{10} cm^{-3} [54]. In addition, it is difficult to control or adjust the energy and density of particles (electrons and ions) in the plasma.

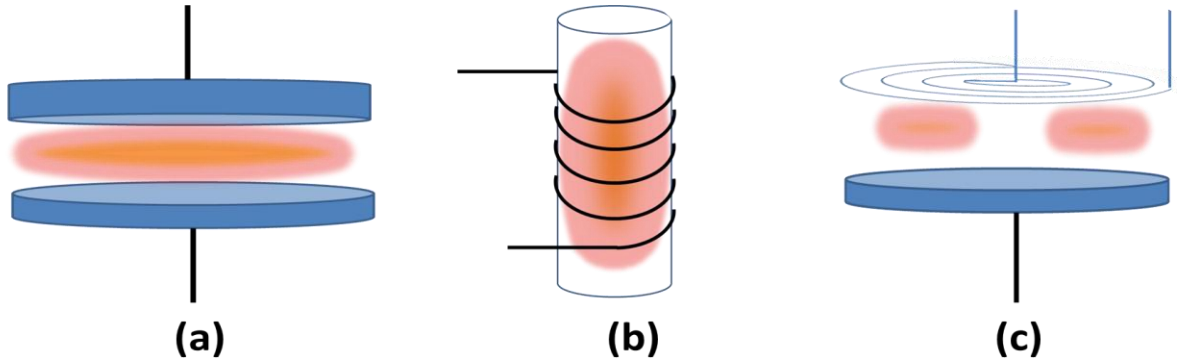

Figure 18. CCP discharge (a), ICP discharge with cylindrical coil (b), ICP discharge with planar coil (c)

To solve the CCP's difficulties, ICPs have been developed. As its name suggests, the RF power should couple to the discharge region inductively. RF current is passed through the coils (antennas), which cause the generation of a time-varying axial magnetic field. As a result, the magnetic field penetrates through the discharge region by passing a dielectric, which is usually a plate of quartz. The time-varying magnetic field can induce an azimuthal electric field through Faraday's law ($\nabla \times E = -\partial B/\partial t$), where E is the electric field and B is the magnetic flux density, which induces RF current in the conducting plasma. The induced current is in the opposite direction of the current through the coil, similar to an electrical transformer. The schematics of the currents and fields are illustrated in Figure 19 [56]. The induced electric field accelerates the electrons and initiates ionization by colliding with ions and neutrals. Heavy particles like ions don't gain enough energy directly from RF due to their large mass. Thus, the electron energy is much higher than that of the ions and neutrals. Consequently, the plasma is in the non-local thermal equilibrium (n-LTE) state. Unlike the CCP, the ion energy can be controlled through an extra biasing in the ICP. This extra biasing can be connected to a conductor substrate holder.

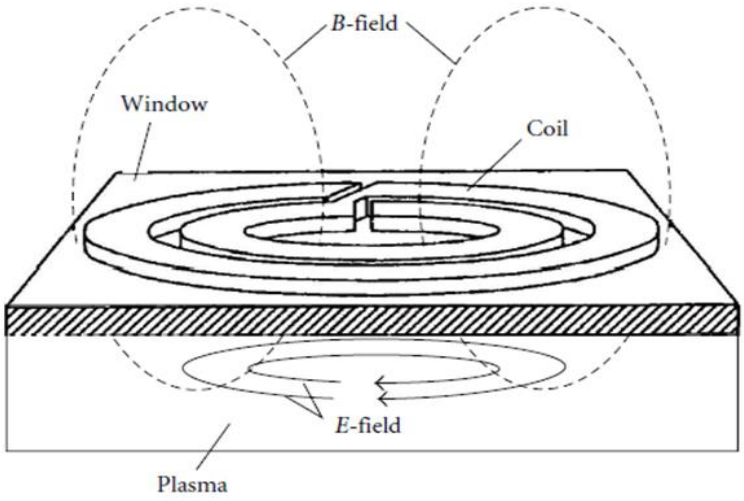

Figure 19. Schematic of Induced current of a planar coil

As depicted in Figure 20 [16], there are two different configurations for an ICP coil: cylindrical (Figure 20-a) and planar (Figure 20-b) coil. The planar coil is a flat spiral wound form (like a stovetop heating coil) that is placed outside (usually on top) of the discharge chamber and isolated from the chamber by a dielectric (quartz) window. In the cylindrical configuration, the coil is wound around the chamber and the wall of the chamber should be made of dielectric materials.

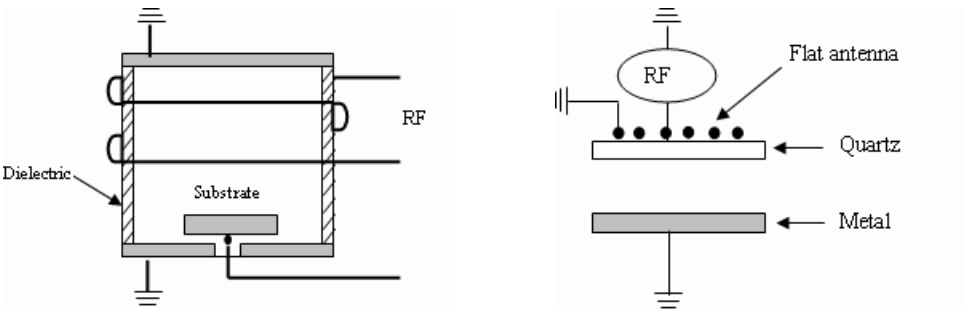

(a) (b)

Figure 20. Two different ICP coil configuration; Cylindrical (a). Planar (b)

The ICP advantages are summarized as follows: The high ion density (10^{10}–10^{12} cm^{-3}), low pressure (typically < 50 mTorr) plasma can be produced in ICPs. The higher ion density leads

to more uniform plasma, which is required for plasma processing. Moreover, there is not any electrode contamination of plasma in the ICP, since it is an electrode-less discharge. In addition, it is possible to independently control the ion energy and plasma density.

3.2.3 ICP in the Plasma Physics Laboratory

The ICP reactor used in this research is located in the Plasma Physics Laboratory of the University of Saskatchewan. It is a planar coil ICP that has a vertical, cylindrical stainless steel chamber with 20.8 cm of inside diameter and 37.5 cm of height from the bottom to the quartz plate. A 2.5 cm quartz plate seals the top of the chamber and isolates the discharge chamber from the RF coil. A planar spiral coil, which is placed on top of the quartz plate, couples the RF power of 13.56 MHz into the plasma. This power applies to the plasma through a matching network that is used to match the impedance of the generator to that of the discharge. Usually the capacitive coupling occurs in the chamber at the same time as induction. To minimize the capacitive coupling in the system, a Faraday shield is introduced between the coil and the quartz plate. The Faraday shield and matching network in the ICP chamber are explained later in this chapter. Figure 21 shows the ICP and the control cabinet used in this research.

Four gas injection lines are available with a gas flow controller for each line making it possible to inject four different gases simultaneously with desirable flow rate into the chamber. Argon and nitrogen were used as working and doping gases respectively in the current project. In addition, a rough and a turbo pump are used to reach the ultimate 10^{-8} Torr base pressure. However, the working pressure can be adjusted by opening and closing a throttle valve as well as tuning the gas flow rate.

Figure 21. The ICP system used in this thesis project.

3.2.4 Matching network

The induced RF power would be at maximum only if the equivalent impedance of the system was equal to the impedance of the power source. It almost never happens due to impedance mismatch RF power are reflected to the source. Consequently, in order to protect the power supply and increase the power dissipation into the discharge chamber, a so-called matching network (Figure 22 [54]) was introduced between the RF source and the discharge (plasma). In order to avoid RF power reflected back to the power source, the matching unit impedance (Z_m)

should be chosen in a way that the overall load impedance $((Z_p \times Z_m)/(Z_p + Z_m))$ equals conjugate impedance of the RF source [54]. Thus, the Z_m is

$$Z_m = \frac{Z_0^* \times Z_p}{Z_p - Z_0^*} \tag{3.1}$$

Where Z_m is the matching unit impedance, Z_p is the plasma impedance and Z_0^* is the conjugate impedance of the power supply.

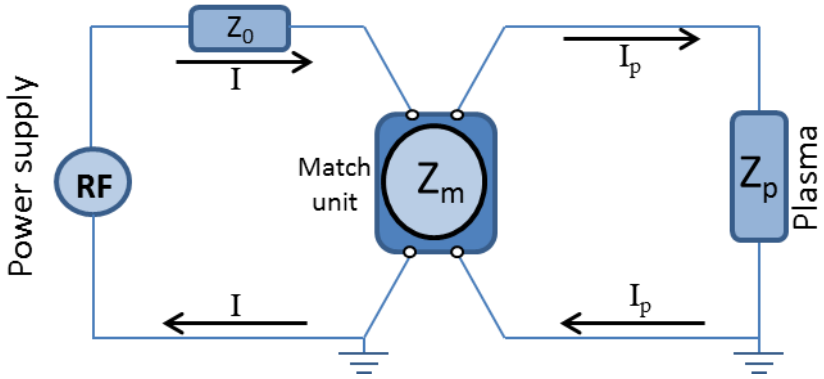

Figure 22. Schematic of impedance matching principle

The characteristic impedance of the RF source has been adjusted to 50 Ω in the ICP power supply. The common configuration for an ICP matching circuit is an L-type matching network including two capacitors and a series inductor for matching the impedance to 50 Ω and forming the resonant circuit at 13.56 MHz. The impedance matching network used for this ICP set-up is a commercial (Match Pro CPM1000, Comdel, Inc.) L-type matching circuit, which is an automatic matching network.

3.2.5 Faraday shield

For minimizing the capacitive coupling in the discharge chamber, a stainless steel Faraday shield is introduced between the antenna and the quartz window. The Faraday shield, as shown in Figure 23 [57], consists of star-shaped radial spikes. It is grounded to reduce capacitive coupling by shorting-out (attenuating divergent) the RF electric fields between the antenna coil and plasma [57]. However, the electromagnetic fields (inductive coupling), which are divergent-free, can pass through the shield without attenuation. Moreover, self-bias charging may happen in the quartz window, and it may damage the window by ion bombardments. The Faraday shield also helps to avoid this damage [58].

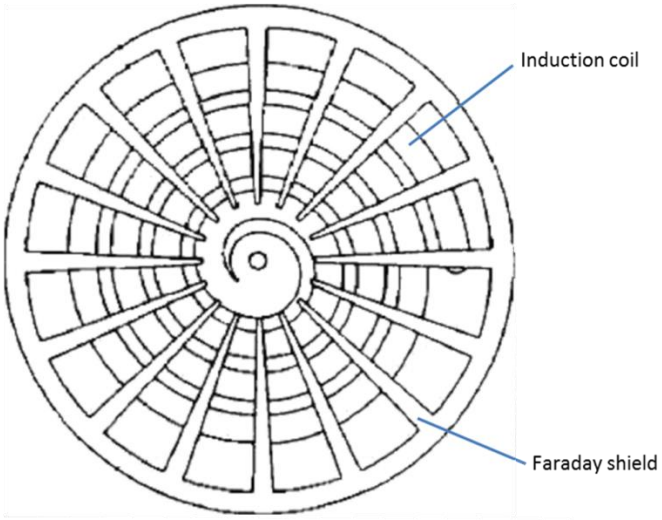

Figure 23. Schematic of the Faraday shield and antenna coil viewed from bottom

3.2.6 Experiment set up with ICP plasma

The research aims to develop a new sputtering technique in the ICP for coating hydrogen-free DLC. The ICP gives us the advantages of low pressure, high-density plasma (HDP). Generally, the plasma density of DC discharges is in the range of (10^7–10^9) cm^{-3}, which is much lower than

the density in ICP plasmas (10^{10}–10^{12} cm^{-3}). The base pressure of the ICP reaches to 10^{-8} Torr while in the HFCVD used in this project, the base pressure is 10^{-4} Torr. In addition, because of the better vacuum system, a higher gas flow rate can be adjusted in the ICP system (maintaining the same pressure). Moreover, the ICP system has a real advantage in the possibility of low temperature coating, which is perfectly suitable for polymer substrates with low melting temperatures. Thus, ICP has been chosen as an effective technique, since the objective of this research project is coating on a polymer (PTFE).

A graphite plate, which is the source of carbon, is the sputtering target and it is biased to a negative DC voltage with respect to the chamber wall using a 1250 V power supply. So the system is a combination of an inductively coupling and DC discharge plasma. The graphite plate is 8 cm long, 6 cm wide and 2 mm thick. There is a circular and grounded substrate holder that is made of steel and adjustable in height. Its height is normally adjusted to the level of the graphite target. The temperature of the substrate can be carefully monitored by the thermocouple placed under the substrate holder. After forming inductively coupled discharge in the chamber, the negative bias voltage of the sputtering target causes acceleration of the ions to the graphite plate. High-energy ions bombard the graphite plate and causing sputtering of the atoms (or clusters) from the target plate. Graphite atoms, through a ballistic movement, can be deposited on the substrate.

Similar to the previous method (HFCVD), various amounts of nitrogen have been doped to the chamber to study the effect of different amounts of nitrogen on DLC thin films. The samples produced are labeled "ICN_X" according to the coating conditions where "I" indicates that the samples are made by ICP and "x" indicates the percentage of nitrogen doping for specific samples. The sample designations are shown in the Table 3.

Table 3. List of ICP samples

Label	ICN_0	ICN_{10}	ICN_{20}	ICN_{30}	ICN_{40}
N_2 concentration	0%	10%	20%	30%	40%

Mixtures of argon and nitrogen are injected to the chamber with the total gas flow rate of 100 SCCM. The nitrogen flow rate varies (by the step of 10) from 0 to 40 SCCM. All experimental parameters were carefully chosen to keep the substrate temperature below 50℃ and the working pressure around 100 mTorr. The RF power was set to 300 Watts and the bias current of 70 mA. The parameters value are listed in Table 4.

Table 4. Parameter values for ICP samples'

RF power	Bias voltage	Bias current	Substrate temperature	Total gas flow rate	Working pressure	Deposition time
300 [Watt]	1250 [V]	65-70 [mA]	45-48 [℃]	100 [SCCM]	90-110 [mTorr]	30 [min]

Experiments show that the growth rate of DLC is faster in the ICP than in HFCVD due to the difference in the densities in the two kinds of plasma. The deposition time was set to 30 minutes in the ICP, while it takes 120 minutes for HFCVD to deposit the films with the same thickness. Furthermore, increasing the nitrogen flow rate may cause minor changes in the bias current, substrate temperature, and working pressure. These minor fluctuations are indicated in Table 4.

Images of ICN_X samples are shown in Figure 24. The samples clearly show different colours possibly associated with effect of nitrogen. Surprisingly, the ICN_0 has a metallic-silver colour. Nitrogen-doped samples are brown-gold in colour. Another possible interpretation for silver colour ICN_0 might be the existence of iron in ICN_0. This fact will be discussed in detail later in the X-ray photoelectron spectroscopy (XPS) characterization.

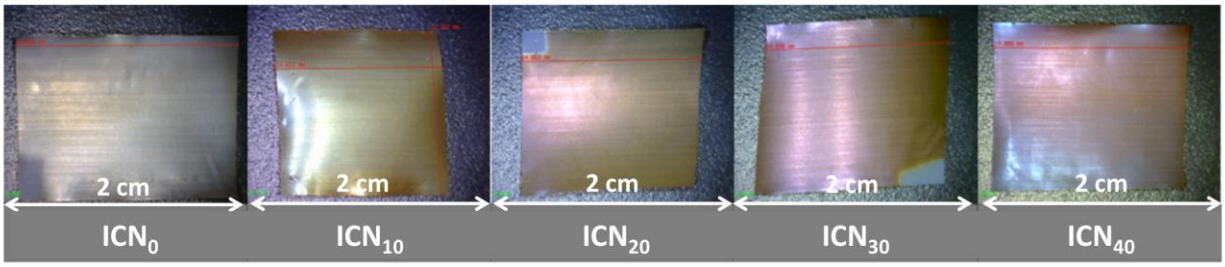

Figure 24. Images of ICN_X samples

3.3 ICP versus HF sputtering

In this study the DLC films are produced by sputtering in two different plasmas: ICP and hot filament. ICP sputtering for DLC deposition is a new technique developed in this work. ICP plasma has some clear advantages over HF plasma for DLC coating. First of all, the turbo pump used for ICP makes a significantly cleaner atmosphere for deposition than the diffusion pump used for the HF reactor. It also makes it possible to use a higher gas flow rate for deposition. Secondly, plasma density produced in ICP is much higher than that in the HF plasma, leading to significantly reduced deposition time for similar film thickness. Another advantage of the ICP system is the low temperature deposition, preferable for plastics and polymer-like substrates. On the other hand, the ICP system is more complex and expensive compared to the simple HF reactor. Parameters discussed above are summarized in Table 5.

Table 5. Parameters in ICP and HF sputtering plasmas

	HF sputtering	**ICP**
Pressure [Torr]	10^{-4}	10^{-8}
Plasma density [cm^{-3}]	~10^{8}-10^{9}	~10^{12}
Deposition time [min]	120	30
Gas flow rate [SCCM]	20	100
Temperature [°C]	~200	<50

CHAPTER 4

CHARACTERIZATION

Reliable characterization tools are required to analyze the surface structures and other properties of the coated films. The morphology and chemical composition of the deposited films are investigated using X-ray diffraction (XRD), scanning electron microscopy (SEM), atomic force microscopy (AFM), Raman spectroscopy, X-ray absorption spectroscopy (XAS), and X-ray emission spectroscopy (XES). The basics of each technique are described in this chapter and results are presented at the end of each section devoted to a particular characterization tool.

4.1 X-ray diffraction

4.1.1 Introduction

X-ray diffraction (XRD) is a non-destructive characterization method used in many fields of science and industries. Studying chemical composition and crystallographic structure of crystalline materials, identification of new compounds and unknown materials, unit-cell calculation of crystalline materials, determination of phases, and other analysis of crystals are the most common applications of XRD. In this method, an X-ray beam is irradiated onto the surface of a material with varying incident angle θ. X-ray diffraction occurs because of the periodic or quasi-periodic spacing between crystalline planes. X-ray beams can be diffracted by crystalline structures, since the wavelength of the X-ray is on the same order as the interatomic spacing of the atoms (~ 1 Å). The plots diffracted beam intensity against the diffraction angle is called XRD pattern.

4.1.2 Diffraction peaks

Constructive and destructive interference of x-radiation waves is the key principle for the X-ray diffraction techniques. Planes of atoms in a crystalline material diffract the incoming X-ray beam. A detector detects the intensity of the diffracted X-ray as a function of radiated angle. High intensity peaks of the diffracted X-rays are detected only if the waves received from different planes are in phase (constructive interference). The intensity is very low if the waves are off phase (destructive interference). The diffraction pattern can be described in terms of Bragg's law. W.L Bragg considered crystals as parallel planes of atoms. If two monochromatic waves are incident on a 2-D crystalline structure, they would diffract off those parallel planes of the crystal (Figure 25). In order to keep the waves in phase after they are diffracted, the different distance travelled by waves must be equal to integer multiples of the wavelength of the X-ray.

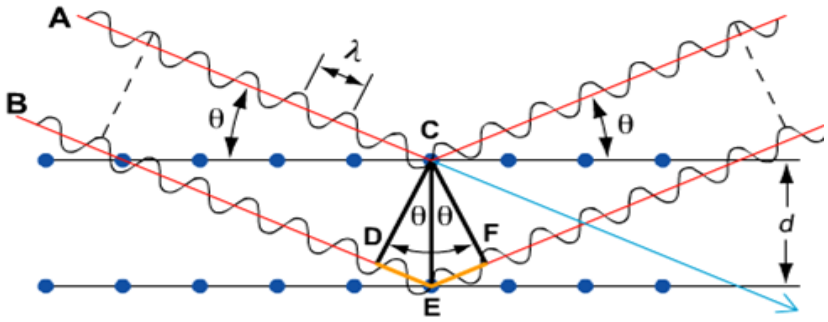

Figure 25. Bragg diffraction

As illustrated in Figure 25, the path difference is given by: DE + EF

Thus, the Bragg's law can be written as:

$$\lambda = 2d_{hkl} \sin \theta \tag{4.1}$$

where λ is the wavelength of the X-ray, d_{hkl} is the interplanar spacing between adjacent, parallel planes, and θ is the incident (also diffract) angle.

Various incident angles (θ) or a range of X-ray wavelengths are used to satisfy the Bragg's equation, since the constructive interference only occurs when the Bragg's law is satisfied. Rotating the crystal is one of the common methods for studying the crystal structure. By rotating a crystal, the X-ray is irradiated to the sample at various angles. Intensity peaks that appear at particular angles are unique for each crystal structure. The XRD pattern can be affected by two factors:

(1) Relative positions of the diffraction peaks are determined by the size and shape of the unit cells.

(2) Intensity of the diffraction peaks varies due to the arrangement of atoms within the unit cell.

4.1.3 Experimental details

XRD data were collected using a Rigaku CN2182D6 theta-theta wide-angle goniometer and Co Kα radiation. This machine is located in the Plasma Physics Laboratory of the University of Saskatchewan. A schematic of the device is illustrated in Figure 26 [59].

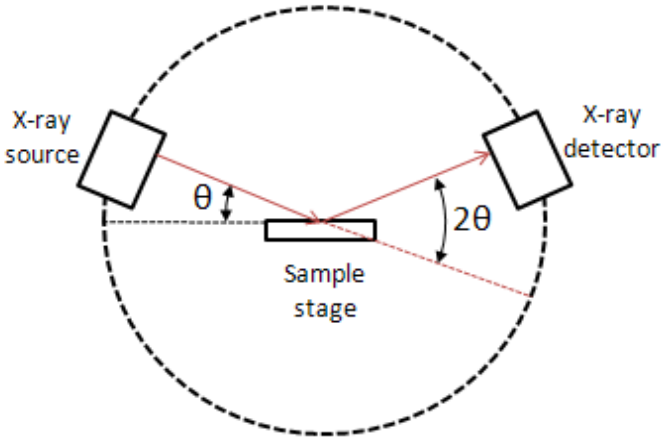

Figure 26. Schematic of theta-theta wide angle X-ray diffraction goniometer

The sample stage, in theta-theta goniometers, remains at the horizontal position. The X-ray tube and the detector rotate simultaneously at the constant angular velocity. If the incident beam has an angle θ with respect to the sample plane, the reflection occurs at an angle 2θ from the incident beam. Thus, the XRD patterns (spectrum) are usually plotted at 2θ instead of θ.

4.1.4 Result and discussion

DLC is an amorphous carbon (a-C) and PTFE is a polymer. However, as Figure 27-b shows, strong peaks in the XRD analysis of the samples "HCN_X" suggest the existence of a crystalline structure in the samples. The measurements were performed in the 2θ angle ranging from 4° to 150°, but the main features are in the range 10° to 70° as shown in Figure 27. The XRD patterns are all the same, regardless of the nitrogen concentration and DLC structure for the samples made by hot filament sputtering. These patterns (Figure 27) suggest that the XRD peaks are not related to the coated films, but to the PTFE substrate. As expected for DLC films, the XRD pattern confirms that the coated film is an amorphous material. A typical peak is observed at 21° and the amorphous phase of PTFE can be seen around 20° and 45°. These two broad peaks in the background identify the amorphous state of the PTFE. The intensity of these broad peaks is related to the degree of crystallinity [60].

This can be explained by the polymer crystallization that may happen while the samples are cooling from near melting point to the room temperature, since the patterns match very well with the standard values from the Joint Committee on Powder Diffraction Standards (JCPDS) data card number 047-2217 (Figure 27-a), which is assigned for crystalized Teflon (PTFE). These kinds of crystals are called semicrystalline or partially crystalline polymers. [61, 59]. The rate of crystallization depends on two temperatures: melting point (Tm) and glass transition temperature

(Tg) which are 327° and -110° for PTFE respectively. The maximum rate of crystallization occurs at a temperature between Tm and Tg (about the middle). Hence, the crystallization of PTFE is expected to occur even at low temperatures near to room temperature.

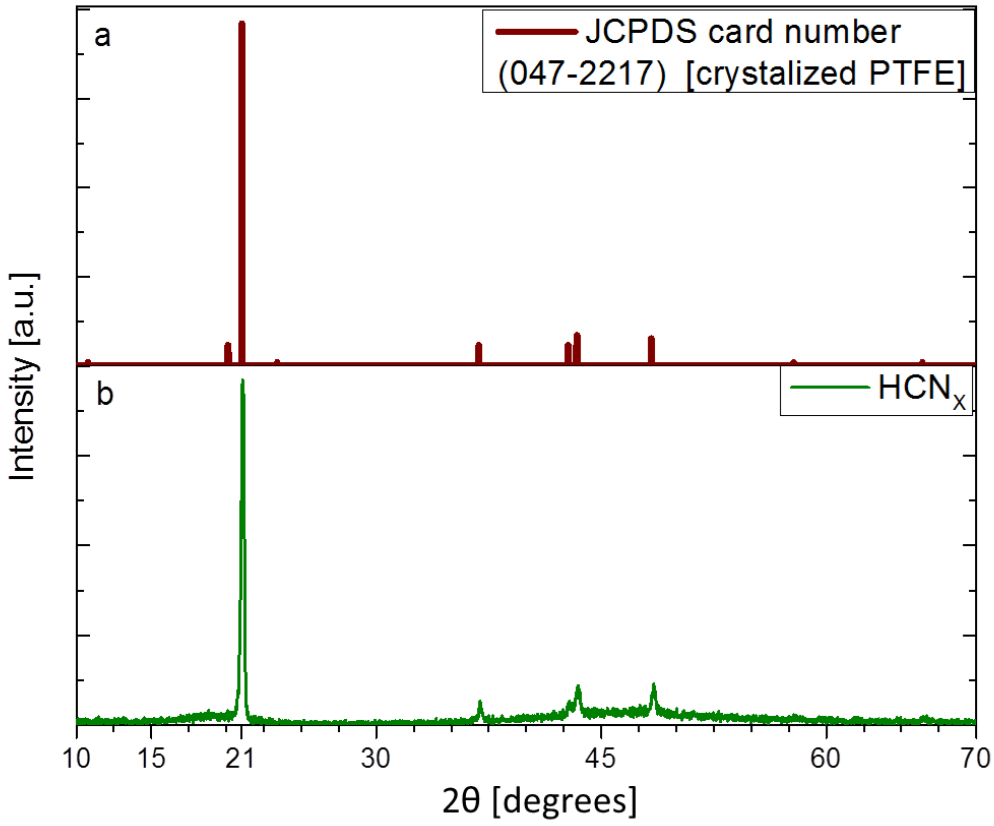

Figure 27. a) XRD pattern from the data base JCPDS card number (047-2217), b) XRD pattern of the sample HCN_{15}

4.2 Scanning electron microscopy

4.2.1 Introduction

Scanning electron microscopy (SEM) is used as a method of investigating the surface properties of materials with high spatial resolution. It can yield information about the topography, morphology, composition, and crystallographic nature of a specimen:

1) Topography refers to the surface shape and features and the texture. SEM can detect features larger than a few nanometers.
2) Morphology gives information about the size and shape of the particles on the surface. The information is limited to a few micrometers.
3) Chemical composition reveals the elements and compounds on the surface and the relative ratios of elements.
4) Crystallographic information refers to the arrangement of the atoms in the sample, which can be related to its conductivity, strength, and other material properties.

The difference between SEM and the optical microscopy is the usage of electrons (for SEM) instead of photons (for optical microscopy). The SEM consists of three main parts: a) electron optical column, b) vacuum system, c) signal detection and display. The optical column is illustrated in Figure 28. The electron beam is produced by an electron gun, which is usually a filament that emits electrons (thermionically) when it gets hot enough. An electric field between the filament and the anode plate accelerate the electrons towards the anode plate and eventually to the sample. In order to form a thin, fine, tight, and coherent electron beam, a set of condensers, objective lenses and apertures are used to focus the electron beams. The objective aperture is adjusted to eliminate high angle electrons. A set of scanning coils makes the electron beam scan

the surface of the sample. The electron energy is typically in the range of hundreds of eV to 30 keV. Interactions between the electrons and the sample produce secondary electrons (SE), backscattered electrons (BE), auger electrons, and even characteristic X-rays. Secondary and backscattered electrons can be detected by specific detectors and used for imaging. The detected electrons can be shown on a screen by a cathode ray display tube (CRT) that is synchronous with the scan coils. Scan coils cause the beam line to scan the surface of the specimen back and forth. Thus, the monitor displays the surface image of the sample with known and calculable magnification.

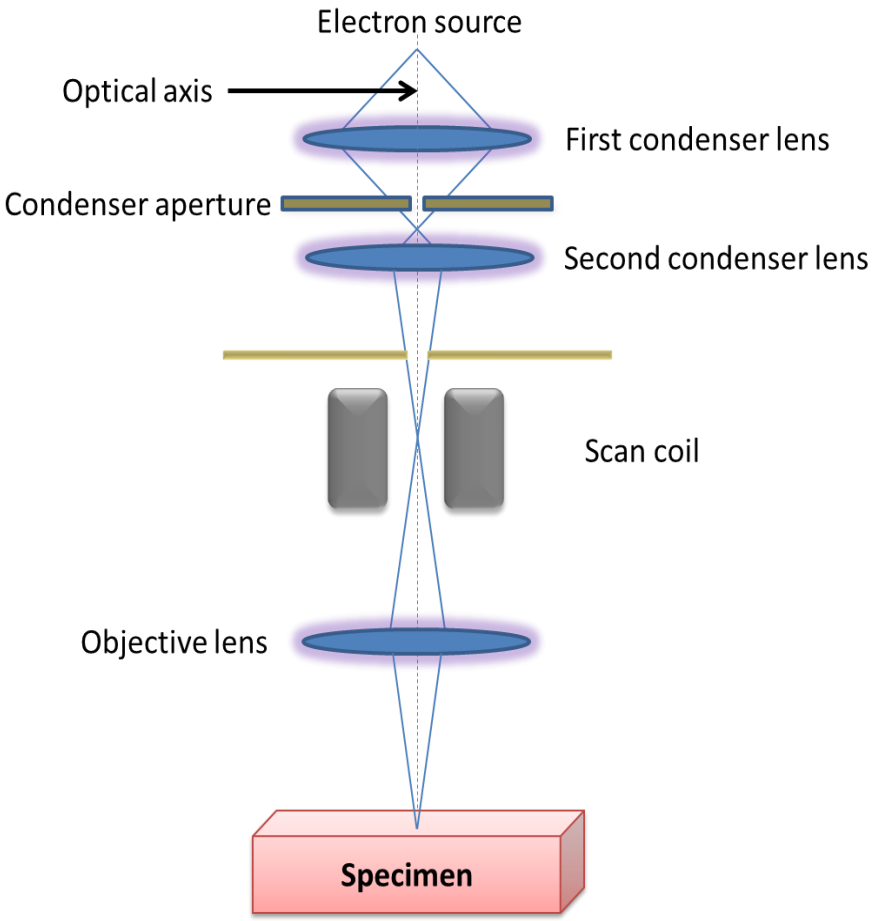

Figure 28. Schematic of the electron optical column in SEM

In order to reduce the chance of interaction of electrons with gas molecules, the SEM needs to be operated in a high vacuum. The typical pressure for SEM is 2.5 x 10^{-5} Pa.

4.2.2 Experimental results and discussion

The model of the SEM used in this research was Hitachi SU6600 located in the engineering building at the University of Saskatchewan.

A uniform SEM images is expected for the deposited DLC films [8]. A low-magnification SEM image of HCN_X (Figure 29-b) shows that the DLC is coated uniformly on the thin (0.05 mm thick) PTFE substrate.

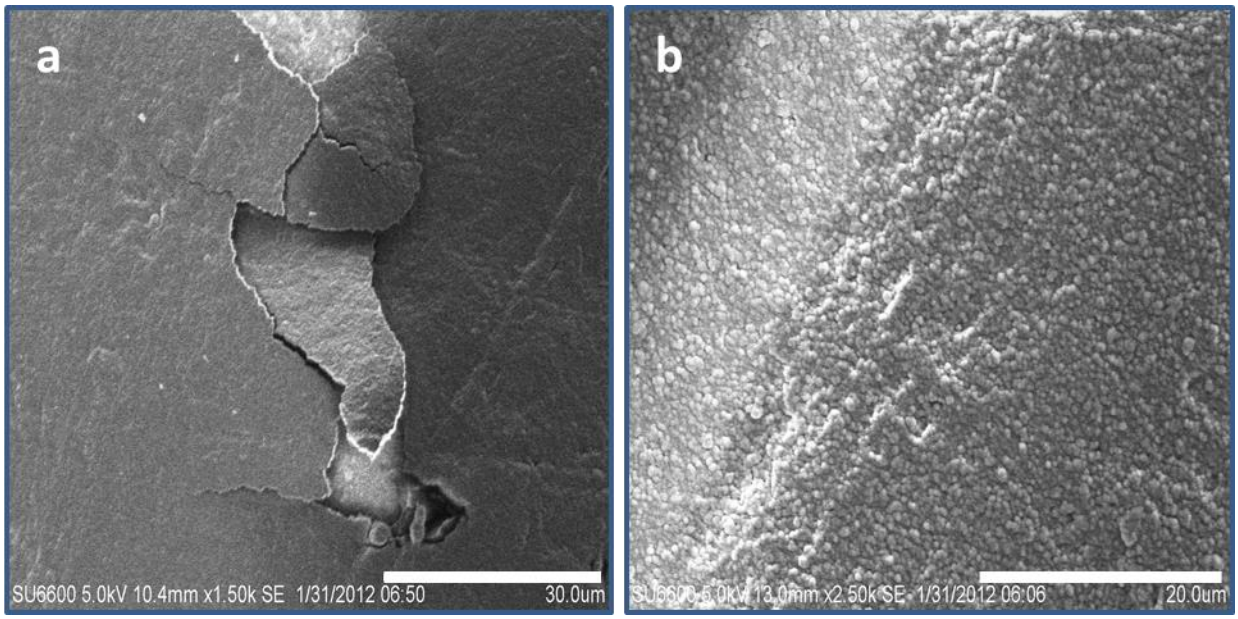

Figure 29. SEM images of DLC films (HCN_{10}) coated on ordinary skived (1.6 mm thickness) (a) and sintered extruded (0.05 mm thickness) (b) PTFE substrates under the same conditions.

It is interesting to notice that the DLC film on the thicker substrate cracks (Figure 29-a) and those on the thinner substrate (Figure 29-b) does not crack. This phenomenon may be by different thermal expansion coefficients for substrates with different thickness. Studying the

effect of substrate thickness on DLC deposition remains as a subject for future investigation. Moreover, the thickness of real stents (50 μm – 100 μm) is around the thickness used in our experiment.

Figure 30 shows the SEM image of HCN_{15}. With higher resolution compared with Figure 29. The carbon grain size is large enough to be observed by SEM in the HCN_X samples. Based on Atomic force microscopy (AFM) images, carbon clusters (grains) in samples produced by ICP are much smaller than clusters of HCN_X films. Note that though the clusters shown in SEM and AFM images may not be the smallest carbon clusters in the sample, the smallest features can be seen in these images. This is due to the AFM and SEM limitations.

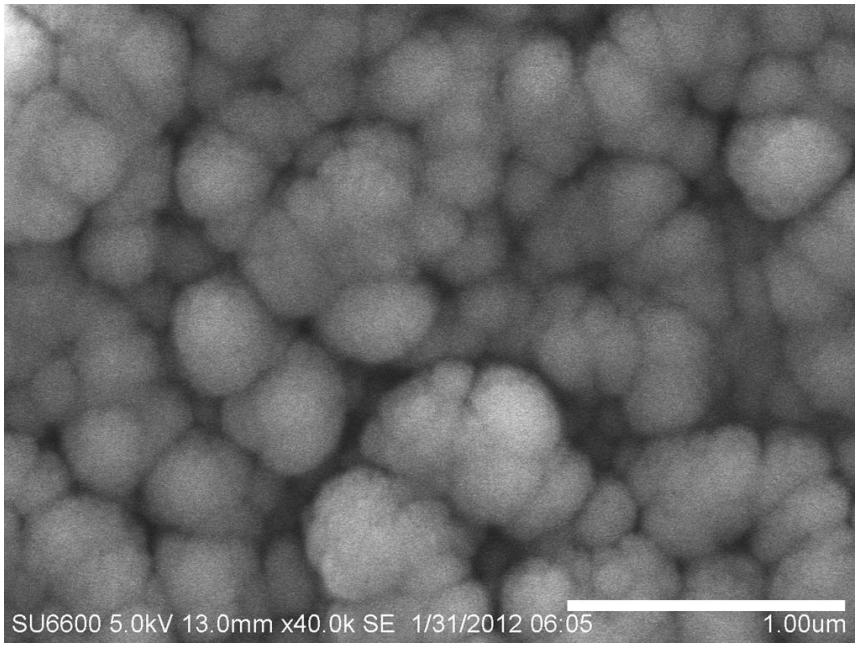

Figure 30. SEM image of HCN_{15}

SEM images for all samples look similar except for the grain size of the carbon, which will be discussed in more detail in AFM images. Compared to HCN_X, the carbon grain size are smaller in ICN_X samples. Analysis of The Roughness and cluster size of the ICN_X and PTFE samples

will be discussed in the section 4.3.2. Figure 31 illustrates the SEM images of the ICN_X samples. Since the coated films are thin respect to the roughness of the substrate, the non-uniform surface of the PTFE substrate can still be detected in these images. The DLC film coated under similar conditions on a polished Si substrate is more uniform compared to the coating on the rough PTFE.

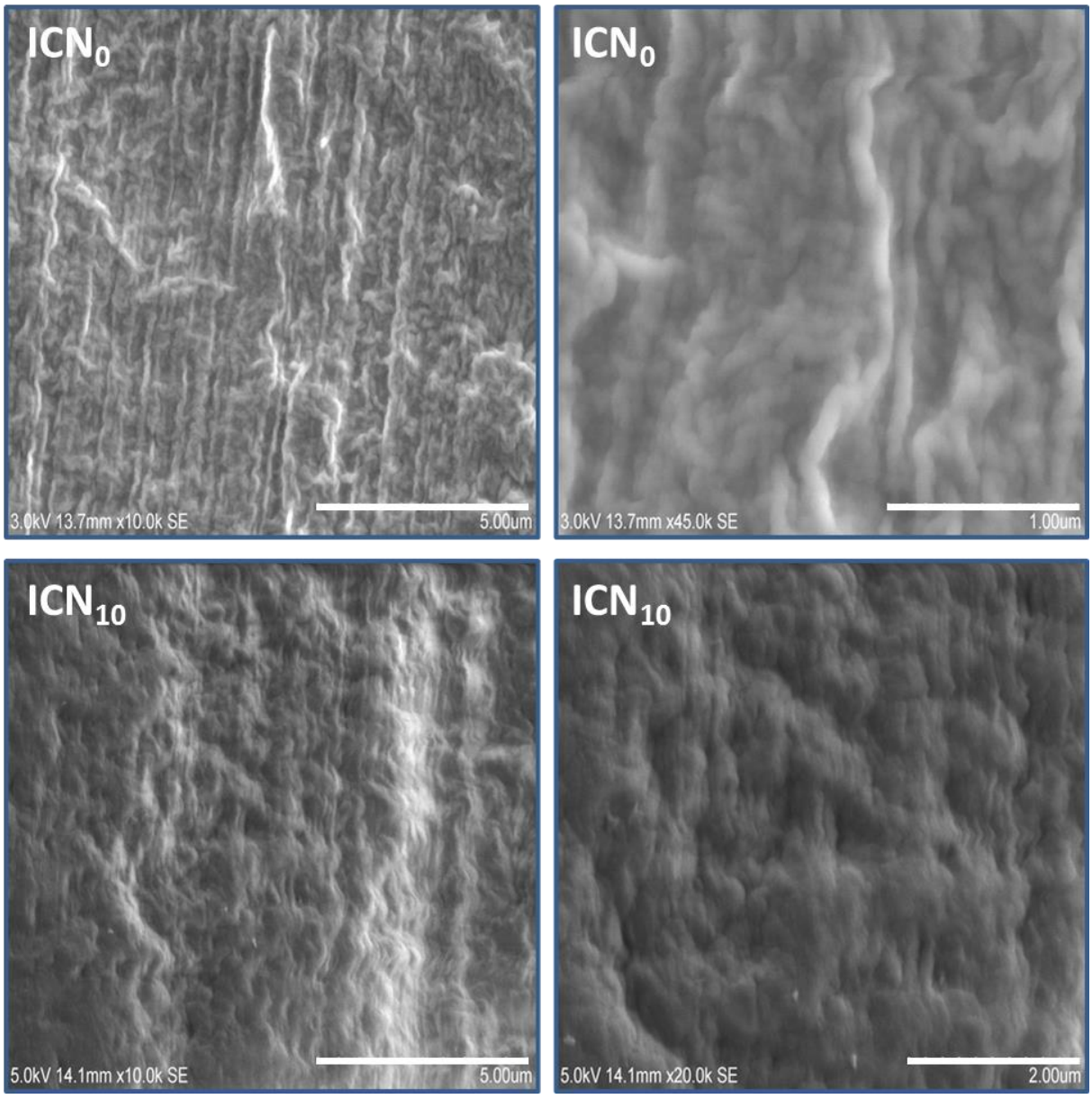

Figure 31. SEM images of ICN_0 and ICN_{10} in different magnifications.

4.3 Atomic force microscopy

4.3.1 Introduction

Atomic Force Microscopy (AFM) is an effective technique for studying three dimensional surface topography and morphology. AFM works with both conducting and insulating surfaces with high resolution in nanometer and angstrom scales. Vacuum conditions and special sample preparation are not required for measurement by AFM. In addition, it is a versatile device and simple in principle. As shown in Figure 32 [62], an AFM consists of a sharp tip (probe) that is mounted to a flexible cantilever and is usually made of silicon or silicon nitride, a laser beam, a photodiode detector, a piezoelectric tube, and a display monitor.

The system works based on the force between the tip and the sample. The tip is brought very close to the sample and is scanned over its surface. The force between the tip and the surface might be attractive or repulsive, which causes bending of the cantilever. Because the bending is too tiny to be observed by eye, a laser beam and a photodiode detector are used to detect the cantilever's oscillation. The beam is reflected from the back of the cantilever and then strikes the position sensitive detector, which is a quad (four-segment) photodiode. This detector can measure both the lateral and vertical deflections. The signal is sent to the piezoelectric tube, which changes its height in order to either keep the tip-sample distance (non-contact mode) or cantilever deflection (contact mode) constant. The piezoelectric tube can also move horizontally (in x and y directions) to scan specific areas of the sample. By tracking changes of the piezoelectric tube, a three dimensional topographic image can be plotted [63].

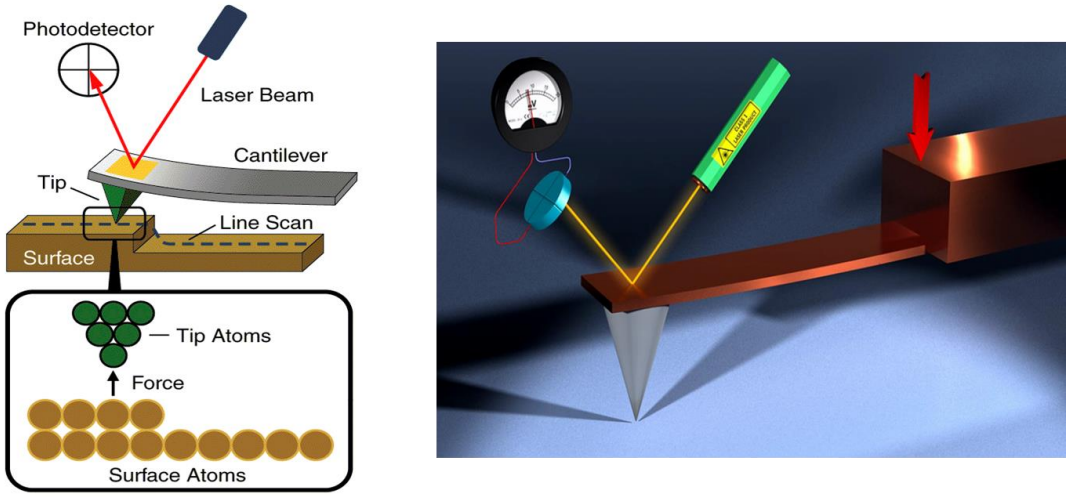

Figure 32. Schematic of AFM

There are three modes of operation for the AFM: (1) contact mode (2) non-contact mode (3) tapping mode [64]. In contact mode, the tip makes a physical interaction with the sample. Using Hook's law, cantilever deflection is proportional to the force applied on the cantilever. Although this mode has an atomic resolution, it is a destructive method and also has the disadvantages of tip contamination and damage. Moreover, a liquid layer on the surface could distort the image. In the non-contact mode, attractive forces play the main role. In this mode, the tip-sample force is kept constant and the interaction between them is minimized. It is a non-destructive mode and the tip lasts longer since there is a distance between the tip and the surface. However, it suffers from slower scan speed and lower lateral resolution. In tapping mode, the cantilever oscillates at or near to its resonance frequency and has intermittent contact with the sample. Thus the tip-sample interaction is constant while it is scanning the surface. The forces between the tip and the sample change the oscillation amplitude, frequency, and the phase of the cantilever. These changes are used to measure the surface features. This mode allows higher image resolution than the other modes. Furthermore, it reduces the problems associated with contact mode such as

friction and adhesion. Tapping mode is used for soft and fragile biological samples. On the other hand, the tip might be damaged during the oscillation and the scanning speed is slow [64].

4.3.2 Experimental results and discussion

The AFM images and roughness measurements were done with the atomic force microscope located in the Saskatchewan Structural Science Center (SSSC) at the University of Saskatchewan. Tapping mode was used for our samples since the films are soft and fragile.

Figure 33 shows the AFM (2D and 3D) images of a bare PTFE substrate. They suggest that the surface of the PTFE is rough with the RMS roughness of 662 nm in the area of 1024 μm^2 and 420 nm in the area of 1 μm^2.

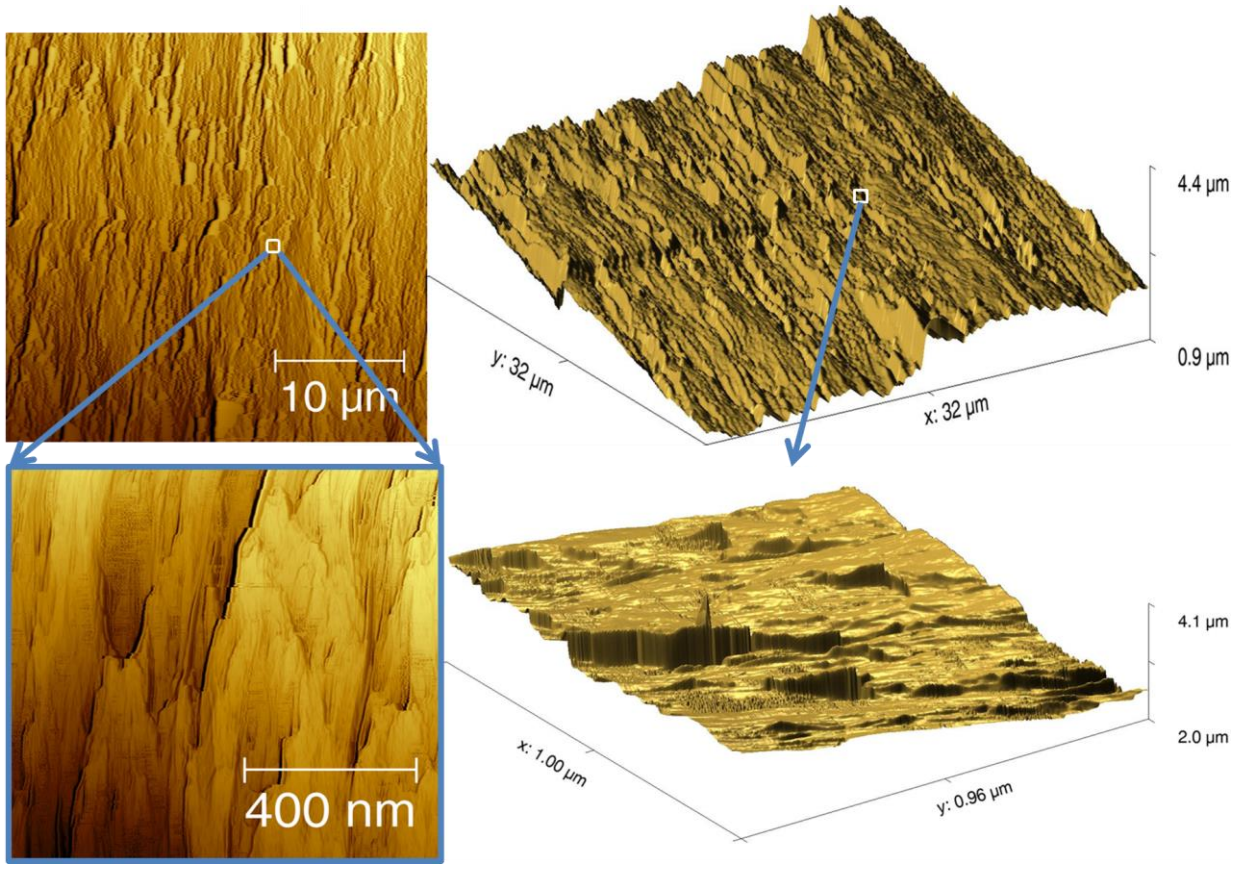

Figure 33. AFM images of a bare PTFE substrate used in this experiment

AFM images of coated samples are shown in Figure 34. The roughness is expected to be reduced in the coated films. However, the DLC film is not thick enough to cover all non-uniform PTFE surfaces and in some images the same pattern of the PTFE surface is visible beneath the DLC film. Thus, non-uniform backgrounds can be seen in AFM images.

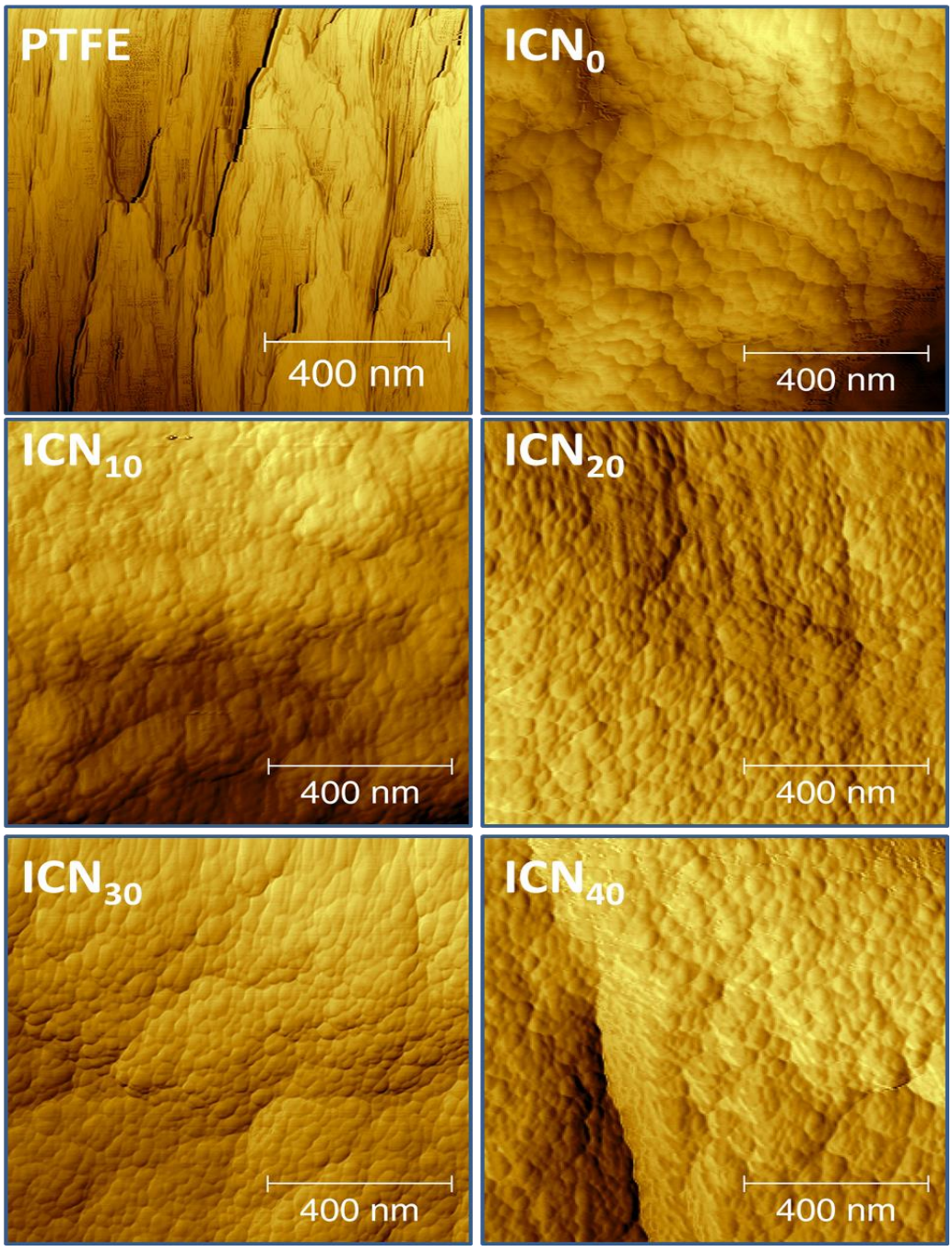

Figure 34. AFM images of a bare PTFE and ICN_X samples

It is interesting to notice that the amorphous carbon grain size decreases with the increasing nitrogen doping. The average diameter of grains was measured for each film using AFM images. The average grain diameter in ICN_0 was 57.6 nm while the grain diameter reaches to ~40 nm after adding nitrogen and it is not sensitive to the amount of nitrogen flow inside the chamber. The ICN_X grain diameters are listed in Table 6.

Table 6. Grain sizes of ICN_X samples measured from AFM images

	ICN_0	ICN_{10}	ICN_{20}	ICN_{30}	ICN_{40}
Grain size [nm]	57.6	40.6	39.2	40.4	41.3

The surface roughness is another characteristic that can be measured by AFM. In the present study the root mean square (RMS) roughness values of ICN_X samples were measured over larger scale (10 × 10 μm) AFM images. The R_q roughness values of ICN_X samples are shown in Table 7. It can be seen that the roughness of films decreases dramatically with coating, but not sensitive to the percentage of nitrogen dopant. Smoother surface is expected to have a lower friction coefficient and allow a better blood flow inside the arteries. Since the PTFE surface is not very uniform, the roughness depends on the surface area, and roughness data are more representative representative if the studied surface is larger. Three different sizes of AFM images have been studied in order to investigate the dependence of the roughness within different sizes images. The roughnesses listed in Table 7 are the average over three selected areas. It is possible to produce 3D images of a surface by AFM. Figure 35 - Figure 39 are 3D images of ICN_X samples.

Table 7. RMS roughness of ICN_X samples in three different probing area sizes measured by AFM

	PTFE	ICN_0	ICN_{10}	ICN_{20}	ICN_{30}	ICN_{40}
R_q [nm] area of (10 x 10 µm)	662	179	173	160	158	159
R_q [nm] area of (2 x 2 µm)	423	92	72	80	84	74
R_q [nm] area of (1 x 1 µm)	420	73	69	70	71	72

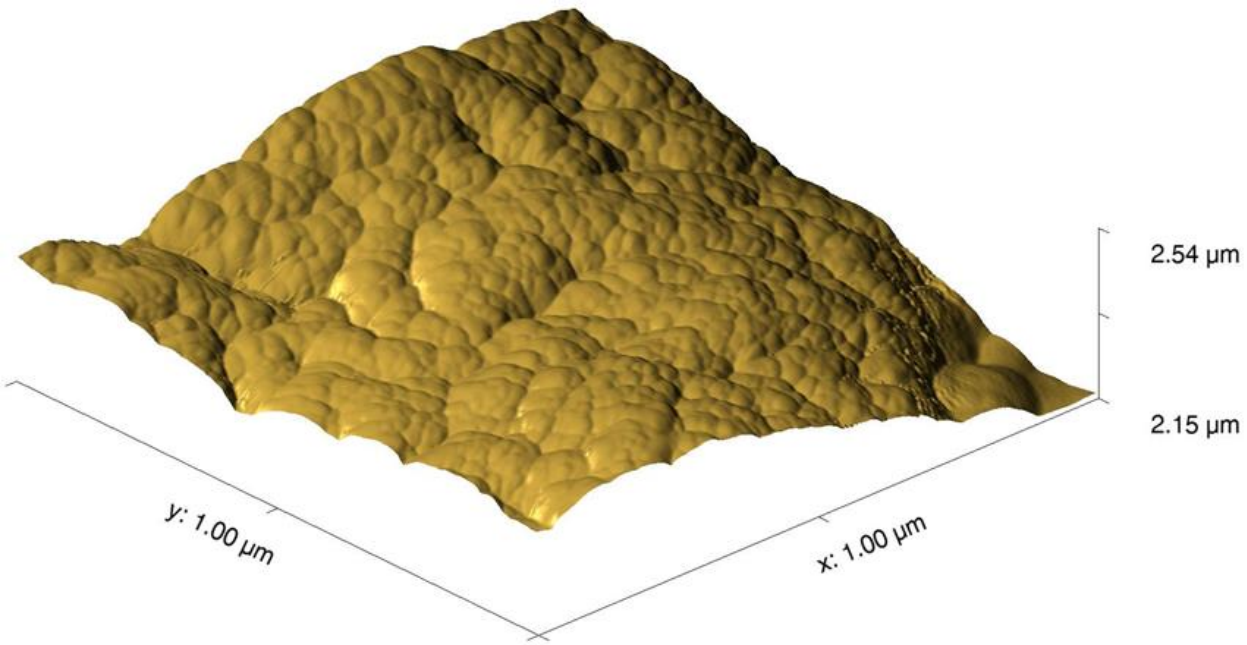

Figure 35. 3D AFM image of ICN_0

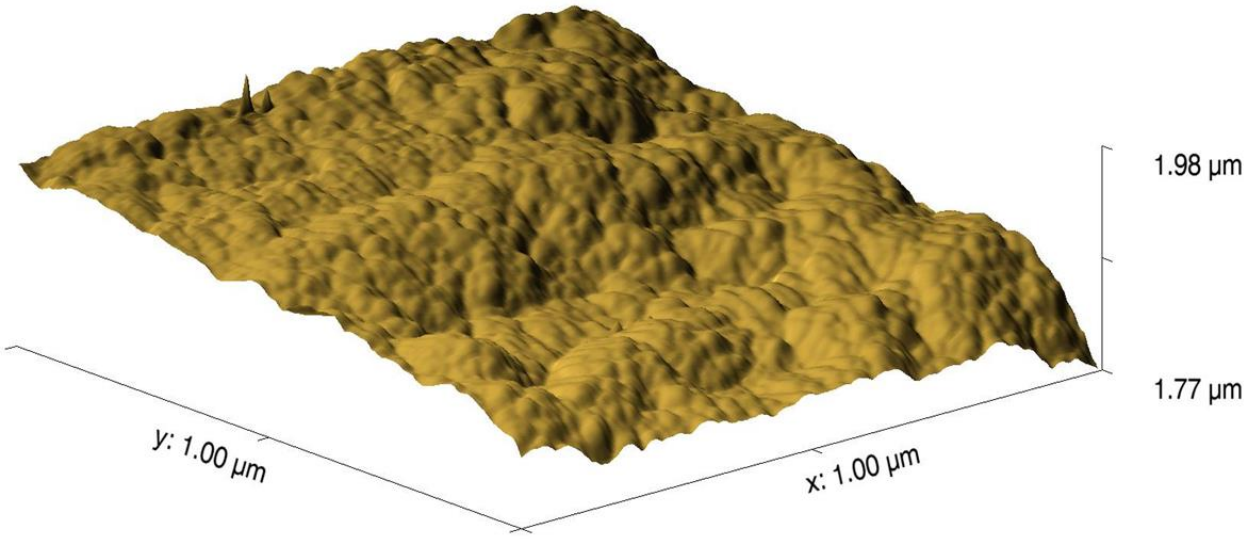

Figure 36. 3D AFM image of ICN_{10}

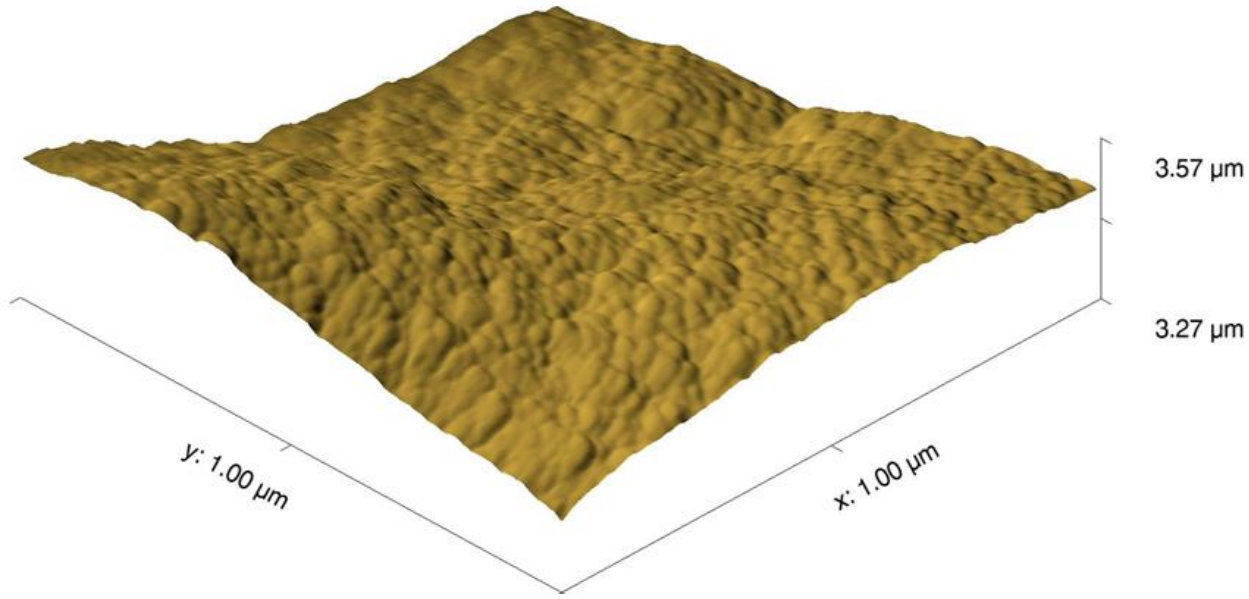

Figure 37. 3D AFM image of ICN_{20}

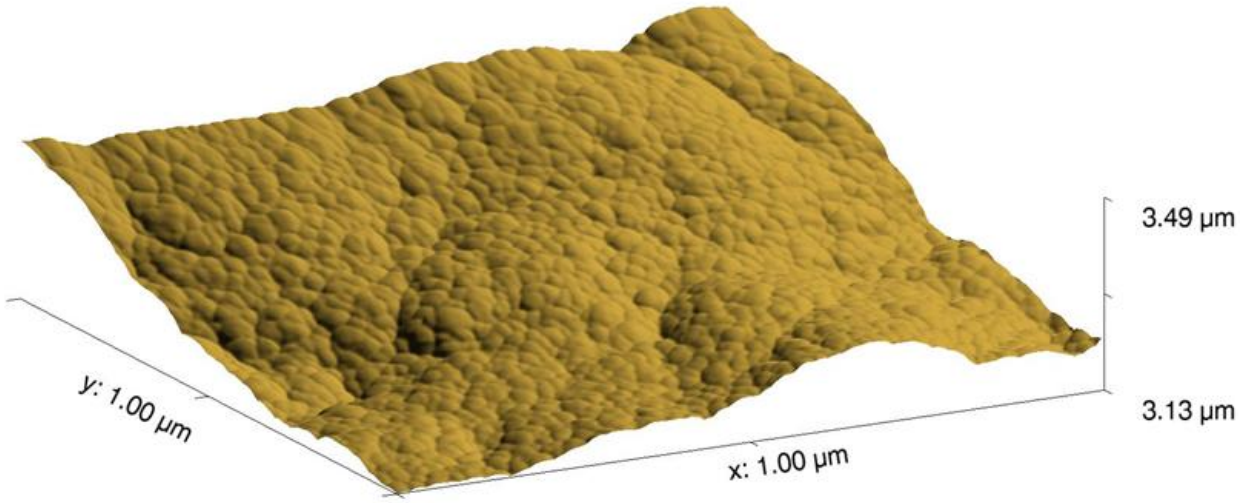

Figure 38. 3D AFM image of ICN_{30}

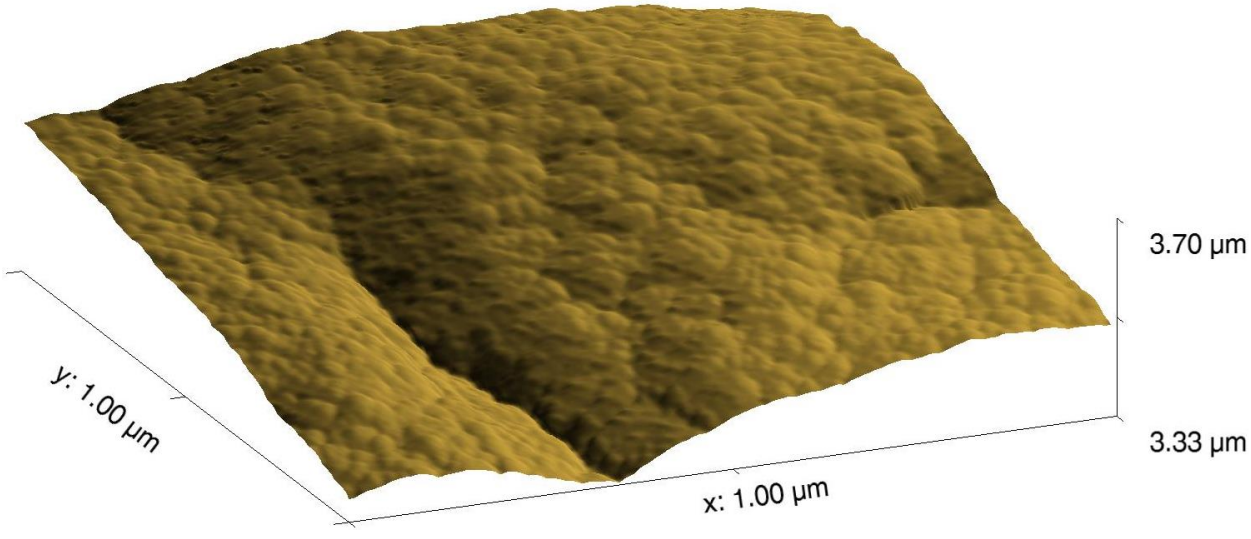

Figure 39. 3D AFM image of ICN_{40}

4.4 Raman spectroscopy

4.4.1 Introduction

Raman spectroscopy works based on the inelastic scattering of a monochromatic light. Monochromatic laser sources are usually used in Raman spectroscopy. Inelastic scattering happens when the frequency of an incident photon is changed after interaction with a specimen. A small fraction of photons are scattered inelastically (Raman Scattering). In Raman scattering, photons that strike the sample, are absorbed by its molecules and reemitted with a different frequency. The shift in frequency is the so-called Raman shift or Raman effect. Deformation of molecules occurs when molecules are struck by oscillating electromagnetic waves (laser beam). This deformation makes the molecules vibrate with characteristic frequency "ν_m". If the frequency of the incident laser beam is ν_0, then we can consider excited molecules as oscillating dipoles which can emit light with three different frequencies (Figure 40 [65]): (1) ν_0: It means the molecule emits light with the same frequency as the incident light without any shift. It happens most of the time (99.999%) and is called elastic Rayleigh scattering. (2) $\nu_0 - \nu_m$: Molecules absorb the photon energy when they are at the ground vibrational state. A fraction of the photon's energy is transferred to the vibrational energy of the molecule and causes it to vibrate with frequency ν_m so the light is scattered with the frequency of ($\nu_0 - \nu_m$) called the Stokes frequency. (3) $\nu_0 + \nu_m$: This happens if the molecule, at the time of the interaction, is in a higher vibrational state with an excessive energy that causes the molecule to return back to the ground state and emit light with ($\nu_0 + \nu_m$) frequency. This type of Raman frequency is called Anti-Stokes frequency. The differential energy (frequency) is exactly equivalent to the vibration energy of scattering molecules. Hence, these shifts can be used for providing information about vibrating molecules.

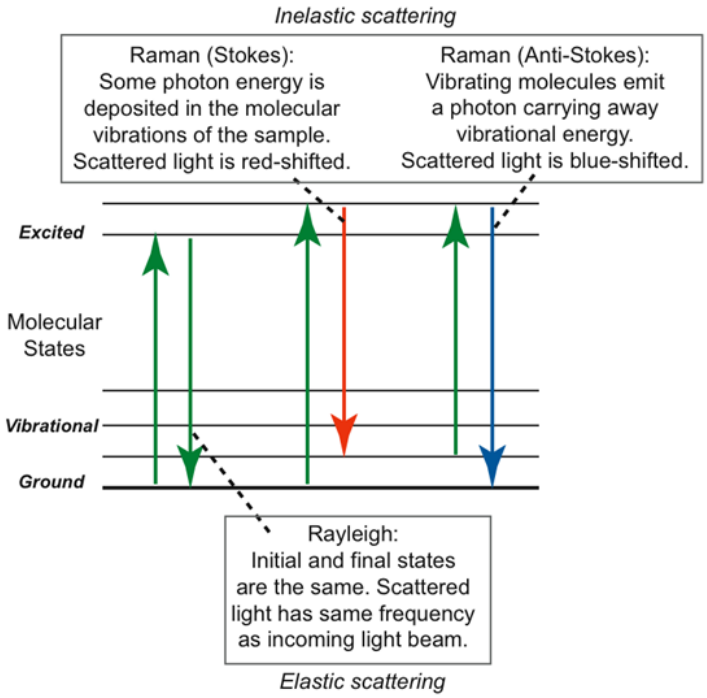

Figure 40. Raman energy levels

Raman spectrum is the plot of the intensity of the scattered light versus the energy difference in terms of the wavenumber (Raman shift). Raman spectroscopy is one of the most common and non-destructive characterization methods for carbon materials [66] since the different C-C bonds are made distinguishable. As shown in Figure 41 [41], Raman spectra of the relevant carbon materials are well known. For example, diamond has a single peak in the Raman spectrum around 1332 cm^{-1}, corresponding to the stretching vibration of the C-C bond; The Raman peak of graphite is around 1580 cm^{-1}. However, disordered graphite has a second peak around 1350 cm^{-1}. These graphite peaks are labelled G and D respectively.

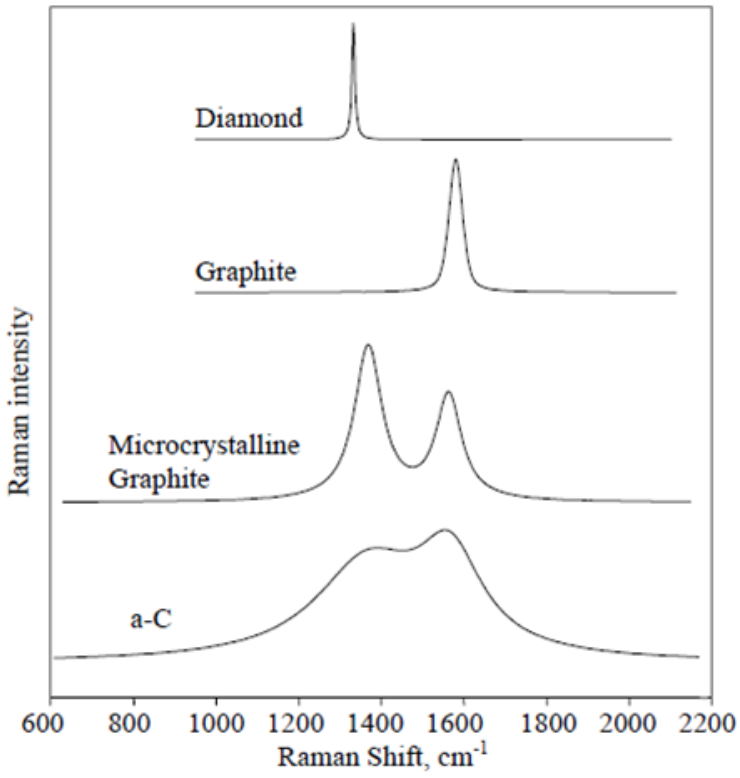

Figure 41. Comparison of typical Raman spectra of carbons

The Raman spectrum of an amorphous carbon (a-C) has two D and G broad peaks around 1350 cm^{-1} and 1520-1580 cm^{-1} [67] as shown in Figure 42 [41]. The G peak is related to stretching mode of both the ring bond and chain bond of sp^2 contents, while the D peak corresponds to the breathing mode of sp^2 sites in rings. Basically there are four factors that can alter the Raman spectra of amorphous carbons [67]: (i) Clustering of the sp^2 sites, (ii) bond-length and bond-angle, (iii) presence of sp^2 rings or chains, (iv) the sp^3 / sp^2 ratio. These factors and how they affect the D and G peaks in terms of height and position are summarized in Figure 42. Complicated relations between these factors, as shown in Figure 42, indicate the difficulty of the task estimating sp^3 content. Beside the structural information, sp^3 fraction is one of the important key parameters of interest in amorphous carbons. Several studies investigating sp^3 fraction of

DLCs have been carried out using Raman spectroscopy [68, 67, 69]. In the visible excitation range, sp^2 sites are dominant and its cross-section is 50-250 times higher than that of the sp^3 sites. However, there is also an independent peak related to C-C sp^3 vibration, which can be seen only in ultraviolet (UV) Raman excitation [67].

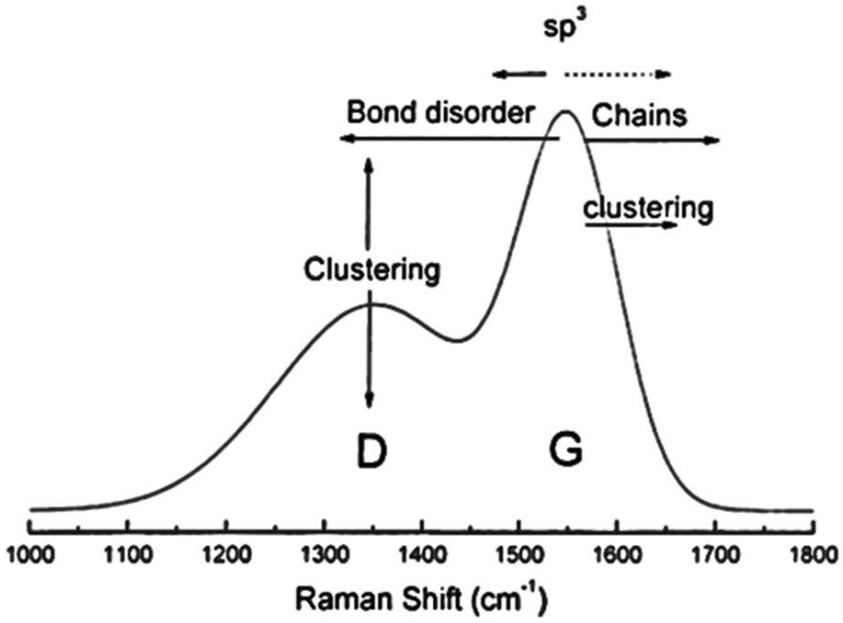

Figure 42. Schematic of an amorphous carbon (a-C) D and G peaks. Arrows show the factors affecting the height and position of Raman D and G peaks of amorphous carbons. Dotted arrow indicates the indirect influence of the sp^3 content on increasing G position

By studying the Raman spectra of DLCs, qualitative and quantitative information about the samples can be extracted. Although the D and G peaks are both related to the sp^2 content, information about formation of the sp^3 bonds can be extracted from the position, area, full with half maximum (FWHM), and the relative intensity (I_D / I_G) of these peaks. As these peaks are overlapped on each other, they need to be de-convoluted by two Gaussians or Lorentzians or the mixture of these two functions [70].

4.4.2 Experimental results and discussion

Raman Spectra were obtained using a Renishaw model 2000 spectroscope equipped with 514 nm Ar ion laser located in the Saskatchewan Structural Sciences Centre (SSSC) at the University of Saskatchewan.

Raman spectra of PTFE coated with nitrogen-doped DLC and nitrogen-free films confirm that a-C is deposited since two wide D and G peaks can be seen in Figure 43 at 1377 cm^{-1} and 1585 cm^{-1} respectively.

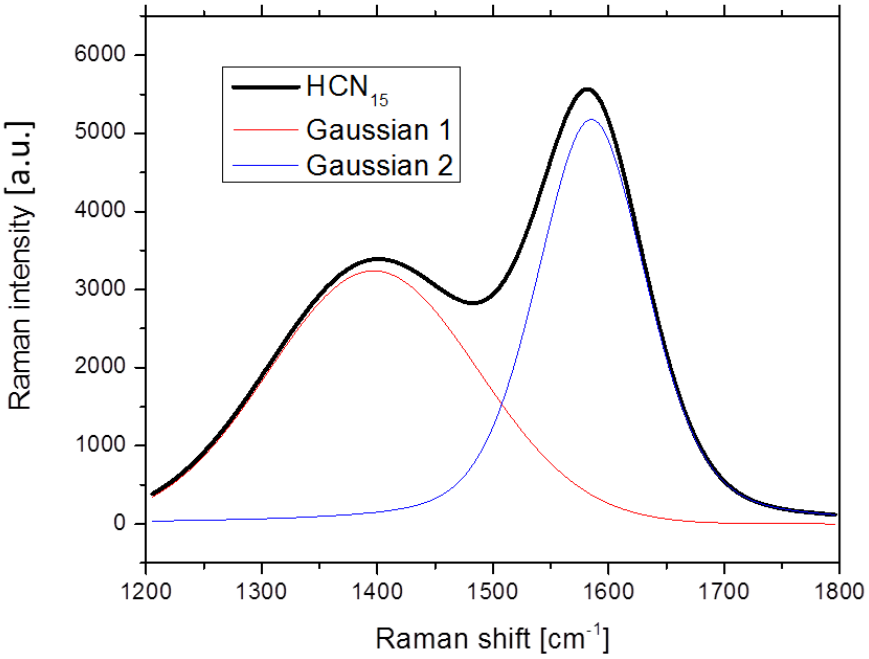

Figure 43. Raman shift of PTFE coated with DLC by hot filament sputtering for 2 hours with 15% nitrogen doping and the pressure of 200 mTorr.

Both HCN_X and ICN_X samples were measured by Raman spectroscopy to study the nitrogen effect on DLC parameters. Two different substrates (PTFE and Si) for ICN_X samples were used to study the effect of substrates on Raman spectra. Figure 44 shows the Raman spectra of ICN_X samples.

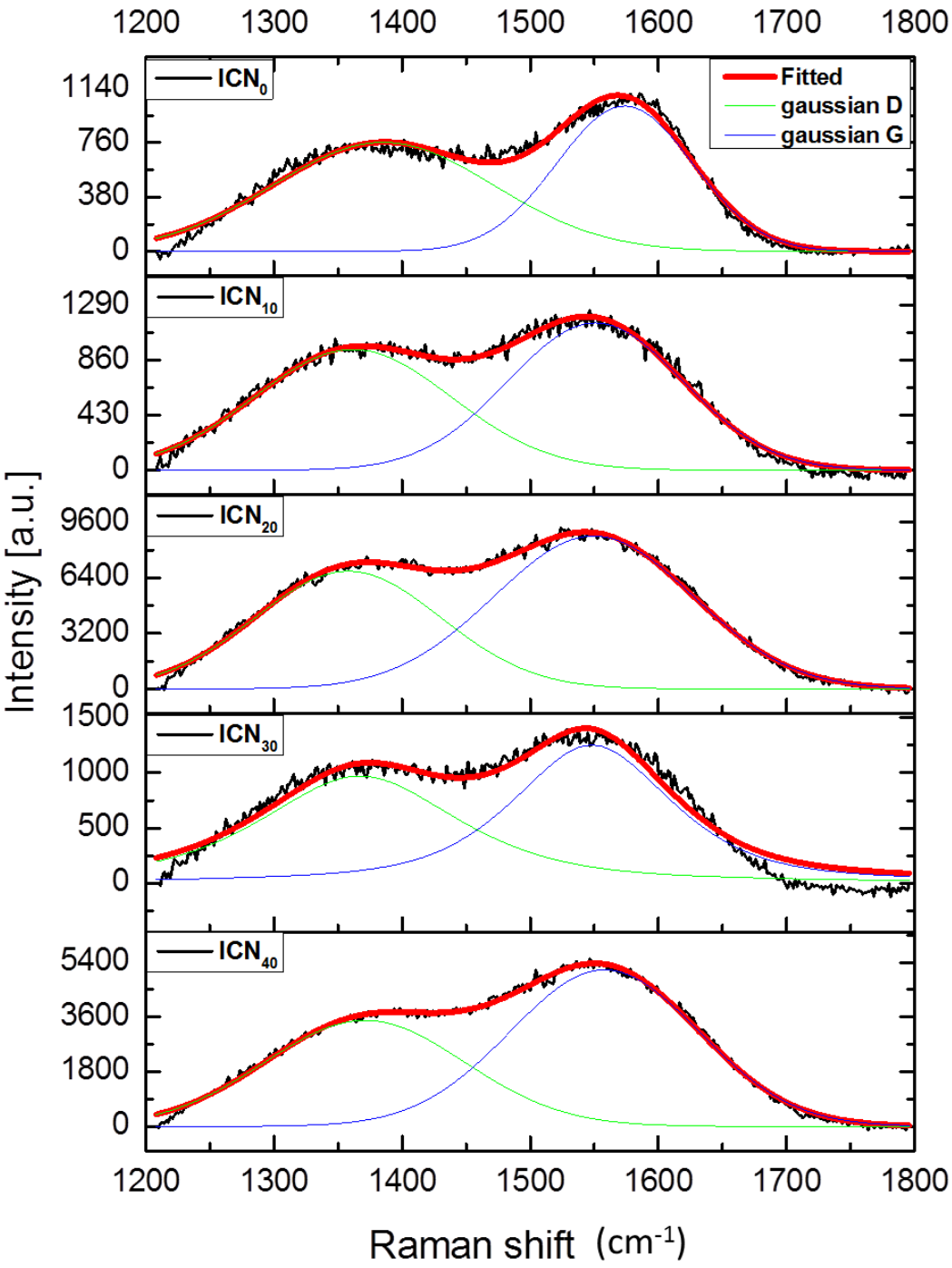

Figure 44. Raman spectra of ICN_X samples

By extracting information from fitted diagrams and measuring and comparing the relative intensity of peaks, G positions, and full with half maximum (FWHM) of G peaks the structural

information and quantitative sp^3 fraction of DLC samples can be obtained. As shown in Figure 45, the G positions in ICN_X Raman spectra indicate that the G position decreases with increasing N contents up to 20% nitrogen and then it slightly increases up to ICN_{40}. Introducing nitrogen to the chamber caused a sharp drop in the G position.

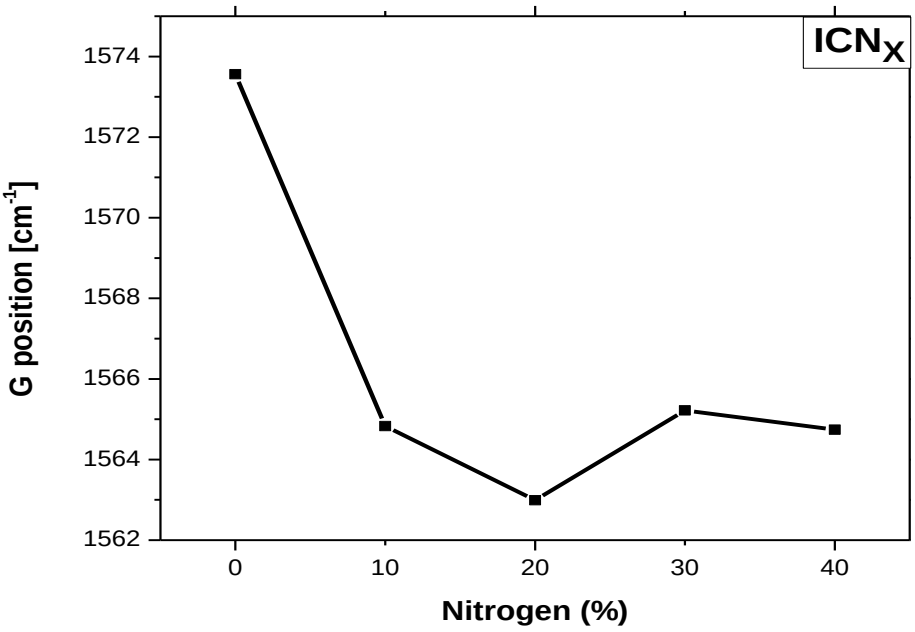

Figure 45. Raman G positions comparison for ICN_X samples

Further analysis (Figure 46) on samples produced by ICP with various conditions and different substrates confirms the same trend: a decrease in the G position of the Raman spectra after doping the nitrogen. Figure 46 shows G position versus nitrogen concentration for 3 different sample series; IC_2N_X samples were made by ICP with higher RF power (450 [W]) and the same ICN_X on Si substrate (labelled ICN_X-Si). No significant differences were found in the trends of the G position diagram of these three sample series. However, the minor variations of G position after 10% nitrogen was introduced. Quantitatively, the G position of IC_2N_x samples, produced by higher (450 W) RF power, is shifted to a lower position. This finding further supports the idea

that more energetic ions could increase the disorder of graphite molecules and decrease the clustering.

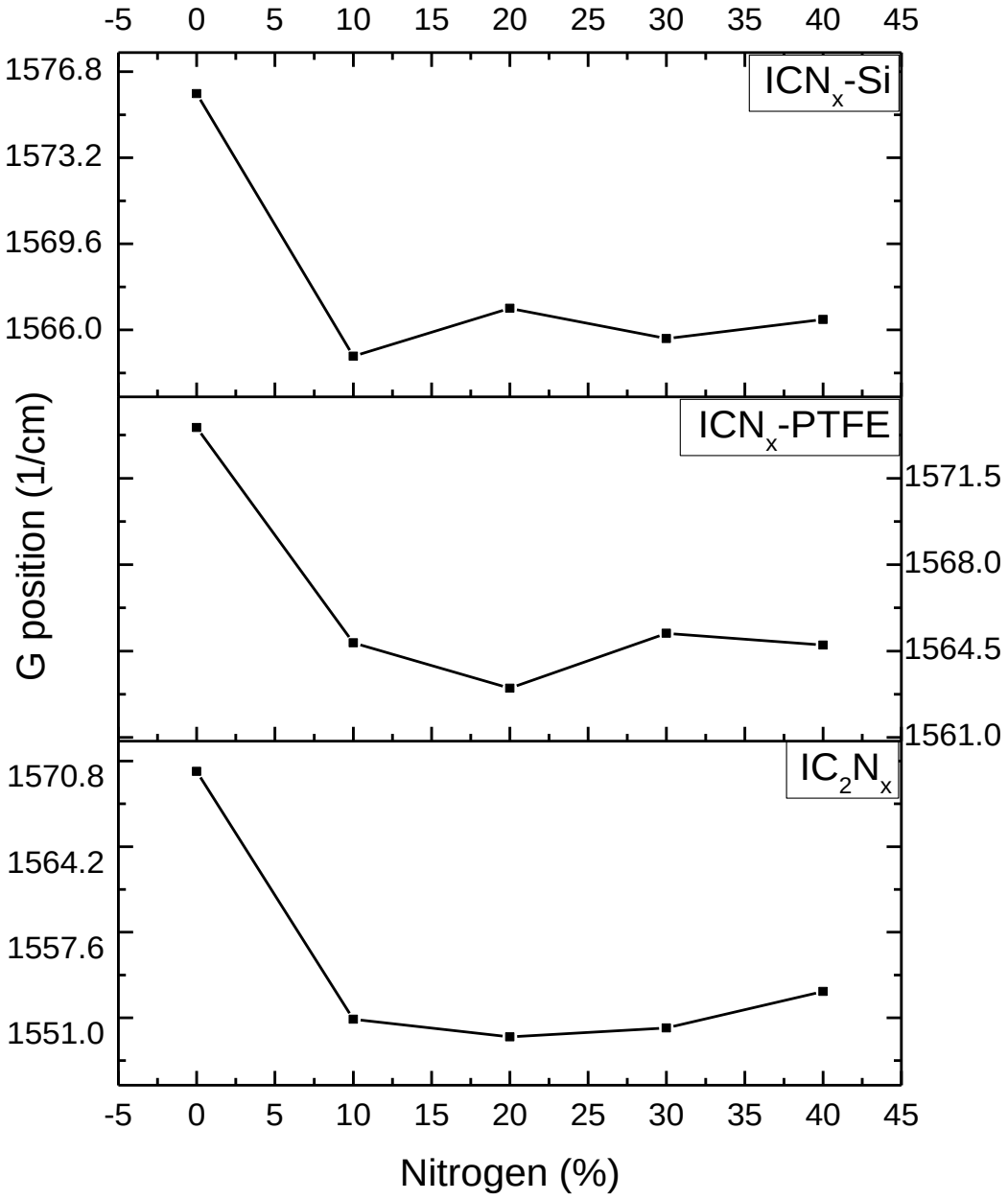

Figure 46. G position of Raman spectra versus nitrogen concentration in ICN_X with PTFE and Si substrates and IC_2N_X produced with an RF power of 450 W

Relative peak intensity (I_D / I_G) was also measured and plotted as a function of nitrogen concentration and shown in Figure 47. It is apparent that the relative intensity (I_D / I_G) versus nitrogen fraction diagrams of ICP samples (ICN_X-Si, ICN_X-PTFE, IC_2N_x) follow the similar pattern and reach their minimum at 20% nitrogen concentration.

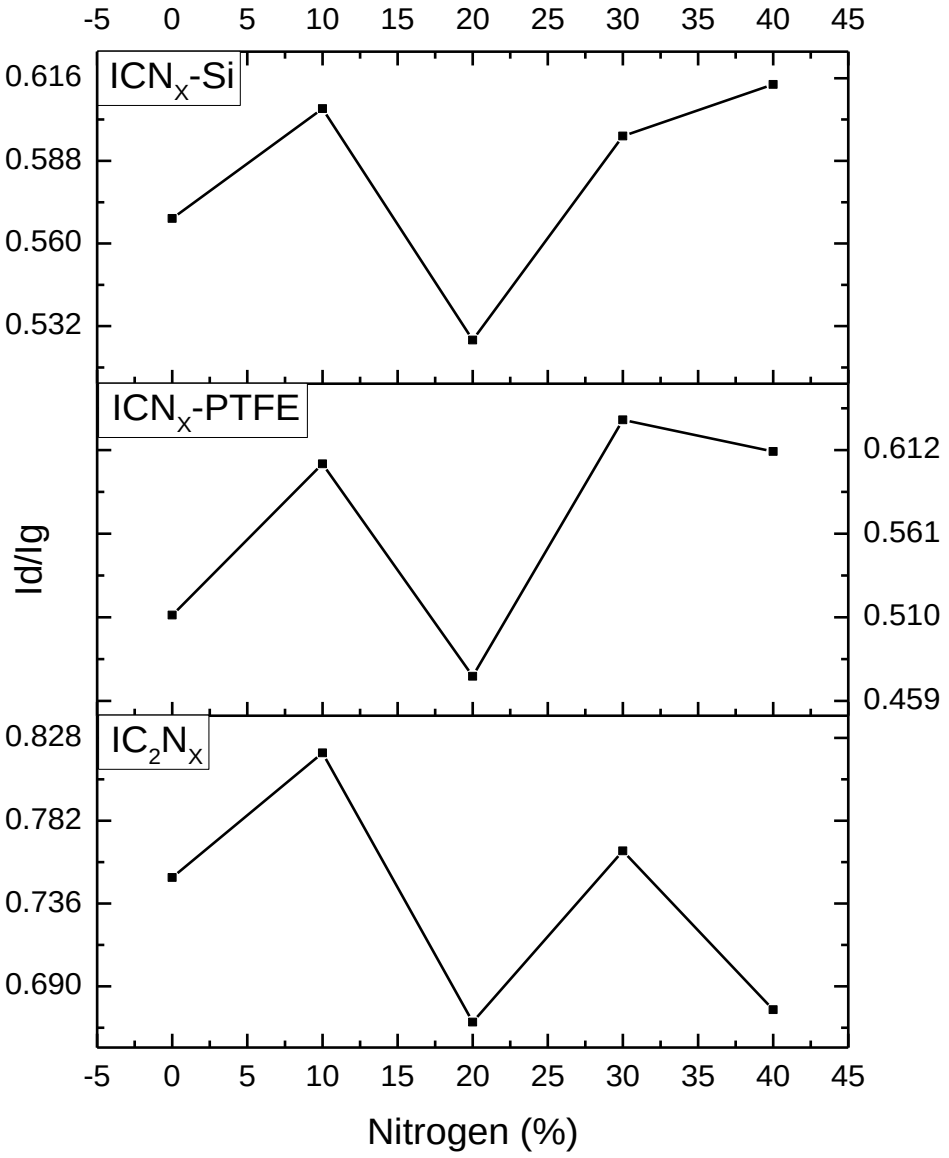

Figure 47. Relative intensity of Raman spectra versus nitrogen concentration in ICN_X with PTFE and Si substrates and IC_2N_X produced by an RF power of 450 W

Ferrari and Robertson [67] analysed the Raman data from amorphous carbon films produced with different methods and concluded that the sp^3 fraction of amorphous carbons is related to G position and I_D / I_G. They showed this relationship in three stages, shown in Figure 48 [67]. Comparing Figure 48 with the current study shows that our samples are in the stage 2 (indicated in blue circles), which means the sp^3 fraction is less than 20%. Our data might match the diagram (Figure 48) in stage three and stage one for G position and intensity ratio respectively. However, the G position and intensity ratio of our samples are agree with each other in the stage two. This finding is in agreement with the idea that sputtered DLCs have less than 20% sp^3 contents (ternary diagram Figure 11-b) [21]. However, in contrast to the G position diagram, D to G intensity ratio goes up with adding nitrogen up to 10%. This rather contradictory result may be due to the fact that nitrogen doping causes an increase in disorder and may not necessarily change the sp^3 contents [21].

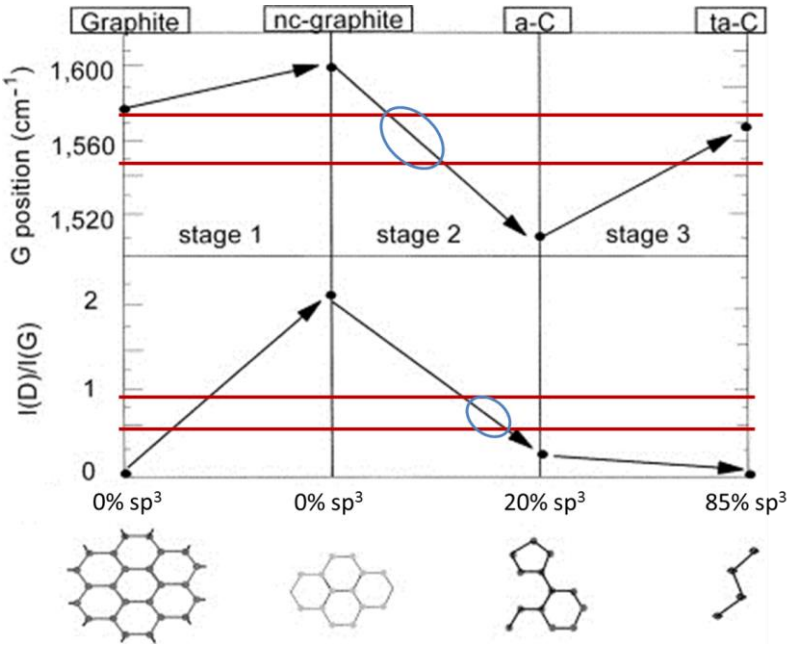

Figure 48. Three-stage model of the variation of G position and D to G intensity ratio. Red lines indicate the range of data collected from ICN_X samples, and blue circles show the points that our data match Ferrari and Robertson's diagram in stage 2.

Figure 49 shows the variation of G peak FWHM with increasing N fraction. Variation of FWHM of the G peak is another helpful mensuration for understanding the structure of amorphous carbons. The FWHM of the G peak is related to the drgree of structural disorder of amorphous carbon films. There is a significant difference in G peak FWHM between nitrogen-doped and nitrogen-free samples.

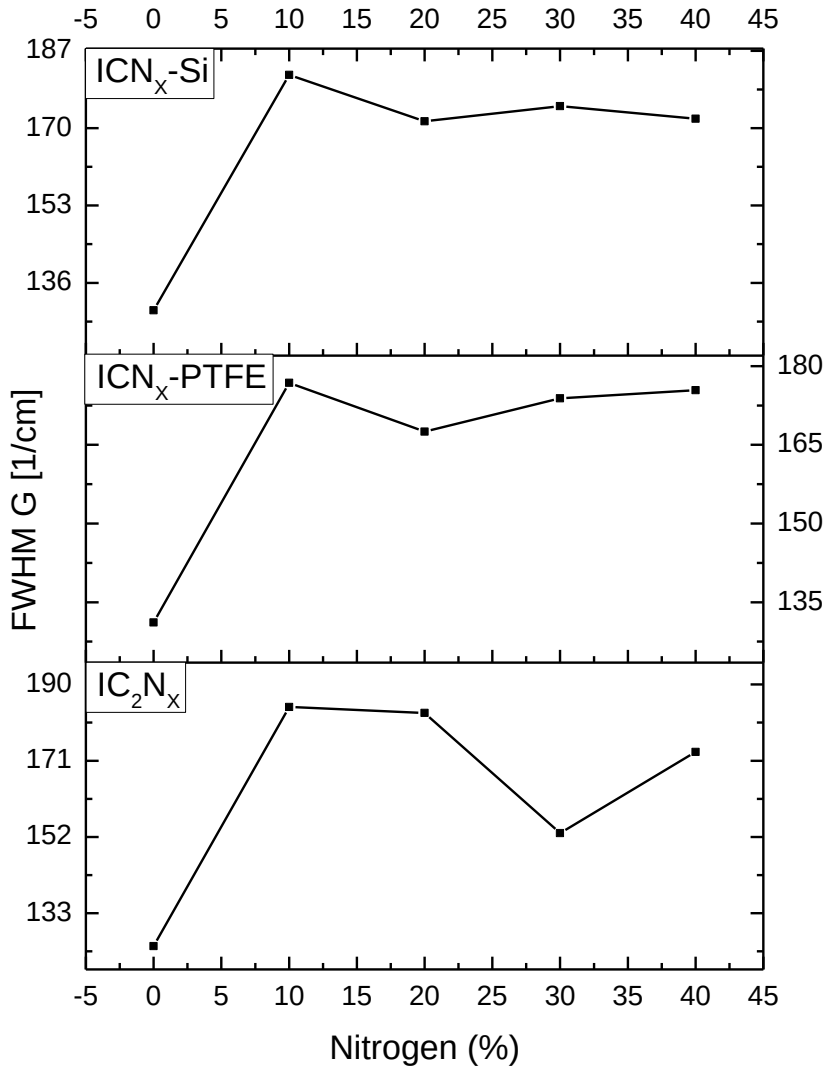

Figure 49. Variation of G peak FWHM with increasing nitrogen concentration in ICN_X with PTFE and Si substrates and IC_2N_x produced by an RF power of 450 W

Increasing G peak FWHM might be caused by an increase in bond-angle disorder and amorphization. Hence, adding nitrogen increases the G peak FWHM, indicating that the sp^3 content is increased. Nonetheless, increasing nitrogen doesn't produce any significant differences in G peak FWHM.

Visible Raman spectroscopy is not an accurate method for quantitative measurement of sp^3 fractions since the T peak, which corresponds to the sp^3 bonds, does not appear in visible Raman. Although there are some models for calculating the sp^3 content in DLC films based on Raman studies, they are not accurate enough to use for all amorphous carbon films, since the DLC is not a unique material but rather a broad class of amorphous carbons with a variety of fraction of sp^1, sp^2, and sp^3 carbon hybridization. Thus, it is hard to generalize the models to all kinds of DLCs.

Visible Raman spectra for HCN_X samples were also taken and the variation of G peak position, D to G peak intensity, and G peak FWHM versus nitrogen concentration were measured and are shown in Figure 50. The trends shown in these diagrams are very similar to the previous samples, while the effect of nitrogen can be studied with more detail here, since the nitrogen is introduced to the chamber by the step of 5%. However, it couldn't exceed 25% due to the device limitations. These results further support the idea of increasing sp^3 bonds with introducing nitrogen. However, the D to G peak intensity ratio increases with adding nitrogen up to 10%. Although the change is not significant, it is in contradiction with the increasing sp^3 content. The seemingly contradictory results may be explained by interpreting the I_D/I_G diagram. Lower I_D/I_G indicates fewer rings (more disordering) and more chains in the structure. However, the rate of change in I_D/I_G with disordering is less sensitive than the rate of change in the G position and the FWHM (G). Thus there may not be enough changes in the sp^3 content to alter the I_D/I_G ratio.

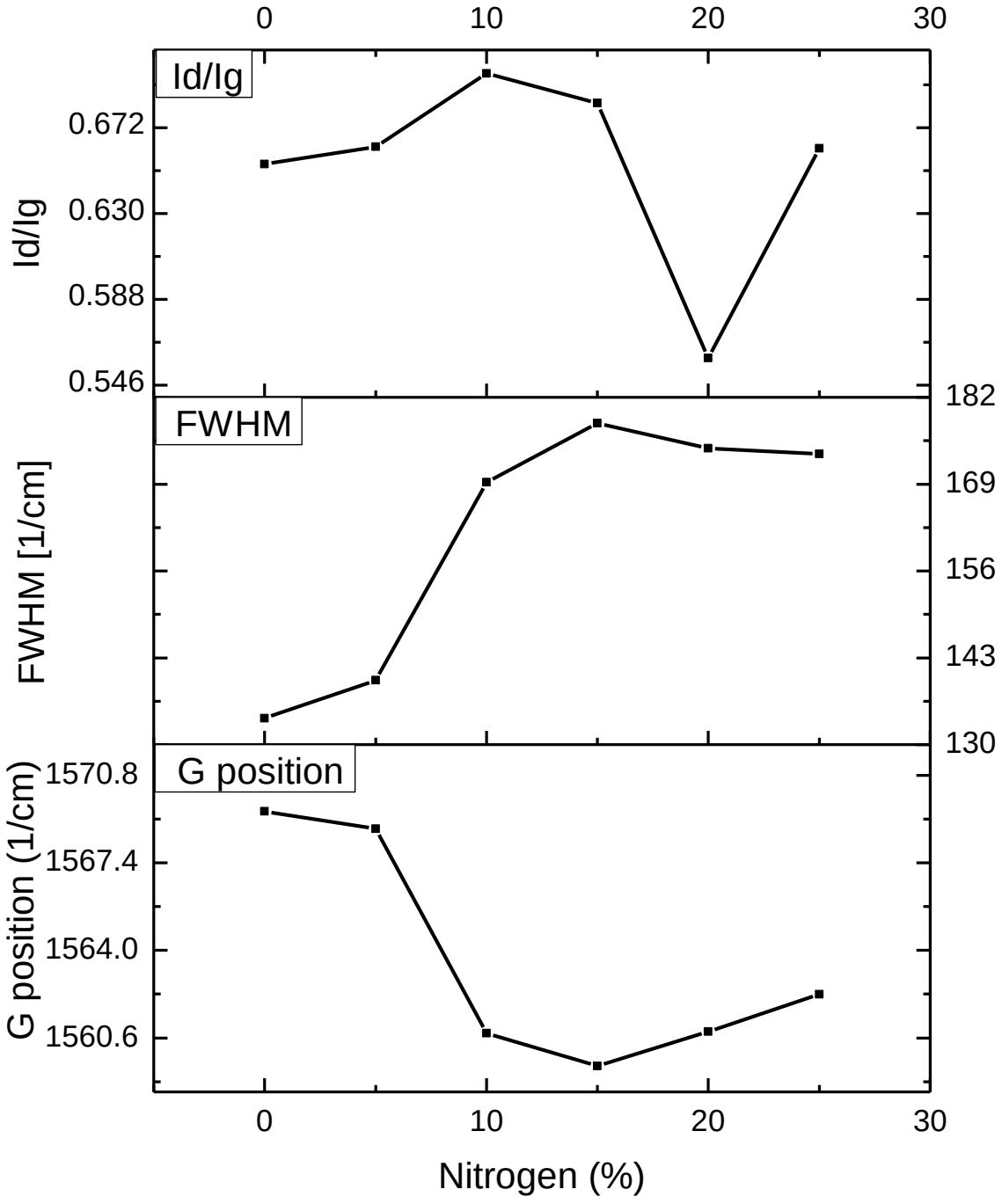

Figure 50. Variation of G position, G FWHM, and D to G intensity ratio with increasing N in HCN_X samples

4.5 X-ray photoelectron spectroscopy

4.5.1 Introduction

X-ray photoelectron spectroscopy (XPS) is a useful method for chemical analysis of materials. XPS works based on the famous phenomenon called photoelectric effect. An X-ray with sufficient energy (usually 1-2 KeV) hits the sample, excites the core electrons and knocks the core or valence electron out with a measureable kinetic energy. The ejected photoelectron is guided by some magnetic fields to reach the detector. The detector measures its kinetic energy. The photoelectron's kinetic energy is less than the energy of the absorbed photon, which is equal to the binding energy and can be calculated using this equation:

$$IP = E_B = hv - E_{kin} - \Phi_{work} \tag{4.2}$$

where IP is ionization potential, which is equal to binding energy, (E_B), E_{kin} is the kinetic energy of the ejected electron, Φ_{work} is the work function of the sample, and "hv" is the energy of the photon.

Since the electron binding energy (E_B) is characteristic of each element and each element has a unique set of binding energies, chemical analysis can be done by calculating the binding energies. An XPS spectrum is a plot of intensity versus binding energy. So the XPS counts the number of electrons ejected from the sample's surface at a sequence of energies. The peak position corresponds to the element from which the photoelectron came. Intensity of peaks represents the elements' concentrations on the sample's surface. Shapes of the peaks also provide information about chemical states for particular elements. Generally, XPS is very surface sensitive because of the low mean free path of photoelectrons. The depth of the sample that can

be probed by XPS is usually less than 20 nm, while the penetration depth of the photon in a solid is in the order of 1-10 micrometers.

In the photoelectric process, the photoelectron is not the only electron emitted from an atom. After creation of a vacancy because of photoelectron emission, relaxation of the ion might cause emission of another electron, a so-called Auger electron. Figure 51 shows the Auger electron process, in which an outer electron (electron in a higher energy level) may fill the vacancy by dropping down. This gives an atom the energy that can be transferred to another electron, moving it up to a higher energy level or providing it with sufficient energy to escape the atom. The auger electron kinetic energy is the same as the difference between the energy of the initial ion and the final doubly charged ion. However, the sum of the kinetic energy of the photoelectron and the Auger electron cannot exceed the initial photon energy. The Auger electrons are labeled with three letters. These three letters are the electron's levels involved in the process. For example, one of the most common Auger transitions is KLL. It means that the process starts with a K shell vacancy followed by an L shell electron dropping down, which causes another L shell electron to escape the atom.

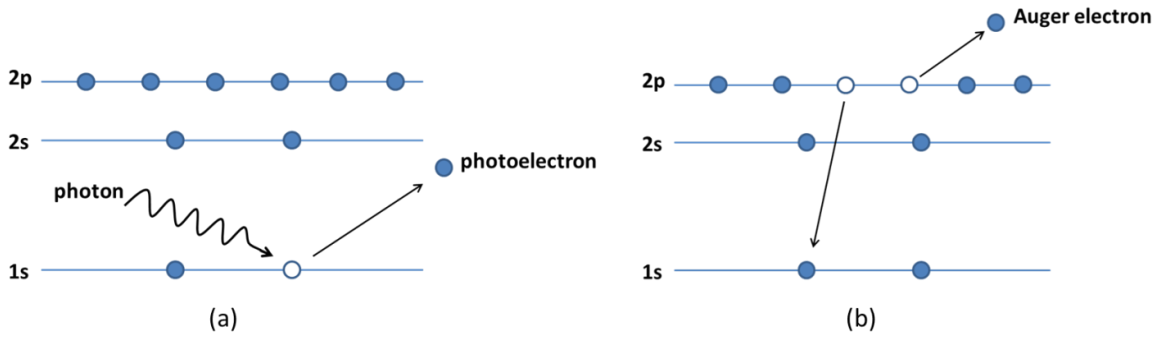

Figure 51. XPS emission processes, (a) ejection of a photoelectron, (b) Auger electron process

4.5.2 Experimental results and discussion

XPS measurements were performed in the Omicron Multiprobe system of the REIXS surface science facility at the Canadian Light Source (CLS) using a monochromatized Al K(alpha) x-ray source and a Sphera EA 125 hemispherical electron energy analyzer with the kinetic energies from 250 to 1000 eV.

Wide spectra were taken with energy steps of 0.5 eV and higher resolution data were taken with 0.1 eV energy steps. The measurements were performed in 2 different emission modes: (I) Glance emission, and (II) Normal emission. In both modes the X-ray source and the detector are fixed but the sample can be rotated. In glancing emission (GE) mode the sample has a 37° angle with the detector making it more surface sensitive (Figure 52-b). On the other hand, the detection of photoelectrons is normal to the surface in normal emission (NE) mode and the escape depth is increased (Figure 52-a).

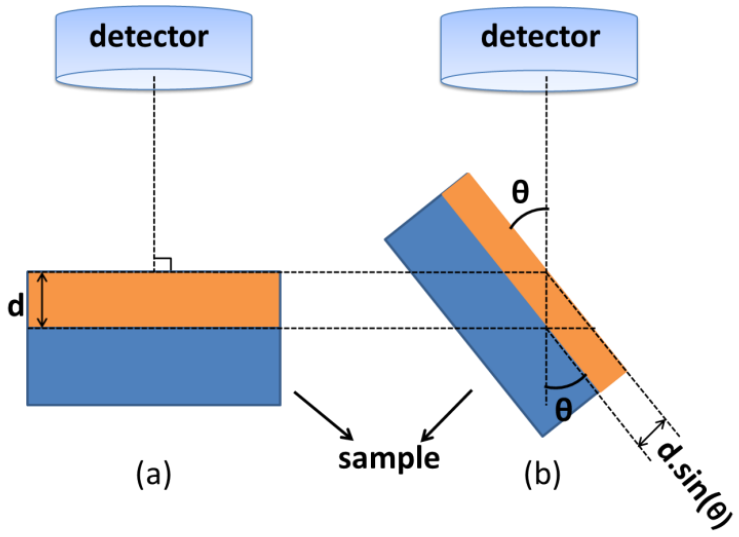

Figure 52. The effect of varying angle in XPS; (a) is the demonstration of normal emission (NE) and (b) shows the glancing emission; where *d* is the escape depth of electrons and θ is the glancing angle

Figure 53 compares the wide scan of XPS experimental data in glancing emission (GE) mode for ICN_X samples with various nitrogen concentrations. Intense photoemission peaks of C 1s, N 1s, and O 1s were detected, indicating their presence as the major species on the surface. As we expected, there is a significant difference between the spectra of nitrogen-doped and nitrogen-free samples. The N 1s peak almost disappears in ICN_0 except for a small intensity that might be related to the contamination of samples with air. Another possible explanation for this is that nitrogen was implanted into the graphite target during sputtering of nitrogen doped samples and as we used the same target for all depositions, a small amount of nitrogen may have been sputtered from the contaminated target onto the nitrogen-free samples. Moreover, oxygen is an unexpected element found in all samples. Since the sputtering chamber was operated under vacuum with an almost free oxygen condition (base pressure of 10^{-8} torr), the high intensity oxygen peaks can be explained by reaction of samples with atmospheric air after the deposition process. Since the fluorine atoms exist only in the PTFE substrate, detection of fluorine in the XPS spectrum (F 1s peak) indicates that the thickness of the coated film is less than the escape depth of photoelectrons. Unexpectedly, a small trace of iron was also observed in the ICN_0. A possible explanation for this might be originated from the stainless steel ICP chamber and substrate holder. Although the chamber and the substrate holder were grounded during deposition, argon ions might have caused sputtering of Fe atoms. As can be seen in nitrogen-doped XPS spectra (Figure 53) there is not any evidence for the existence of iron after adding nitrogen to the chamber. It is difficult to explain this result, but it might be related to the effect of nitrogen ions on removing iron atoms from the surface. Moreover, the peaks (C 1s, N 1s, and O 1s) are gradually broadened with increasing nitrogen content. This effect will be discussed later in this section by studying narrowed-scan C 1s peaks individually.

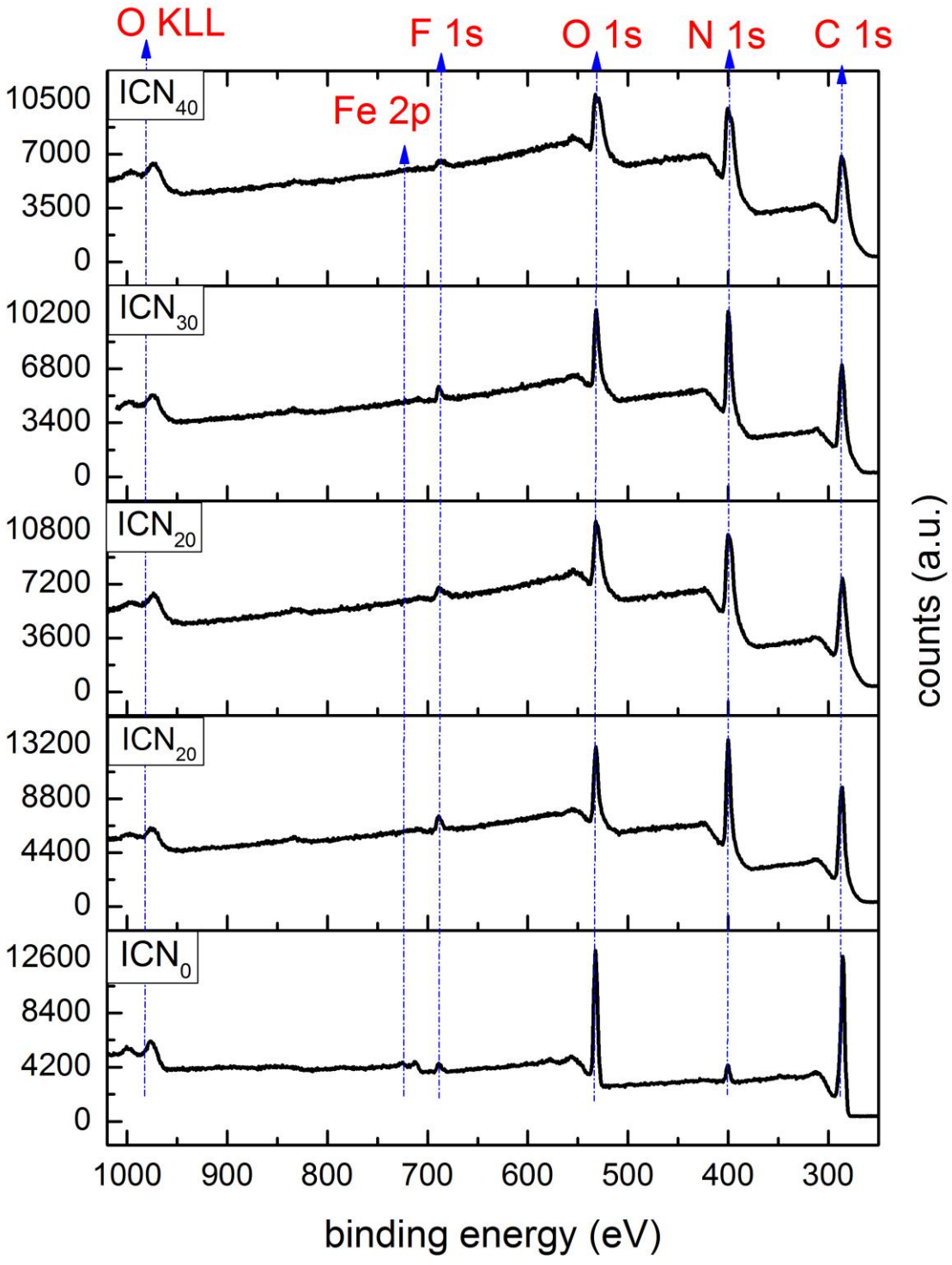

Figure 53. Wide scan of XPS spectra of ICN_X samples in GE mode

Figure 54 illustrates the nitrogen and oxygen concentrations on the surface of ICN_X samples. XPS quantification in terms of atomic concentration is performed by measuring the relative integrated intensity of each peak. The quantitative measurement of integrated intensities indicates that the nitrogen concentration in ICN_X samples increases rapidly from ~5% in the ICN_0 to ~35% in the ICN_{10} and remains roughly stable up to the ICN_{40}. On the other hand, the oxygen decreases from ~42% in ICN_0 to ~26% in the ICN_{10} and remains almost constant until the ICN_{40}.

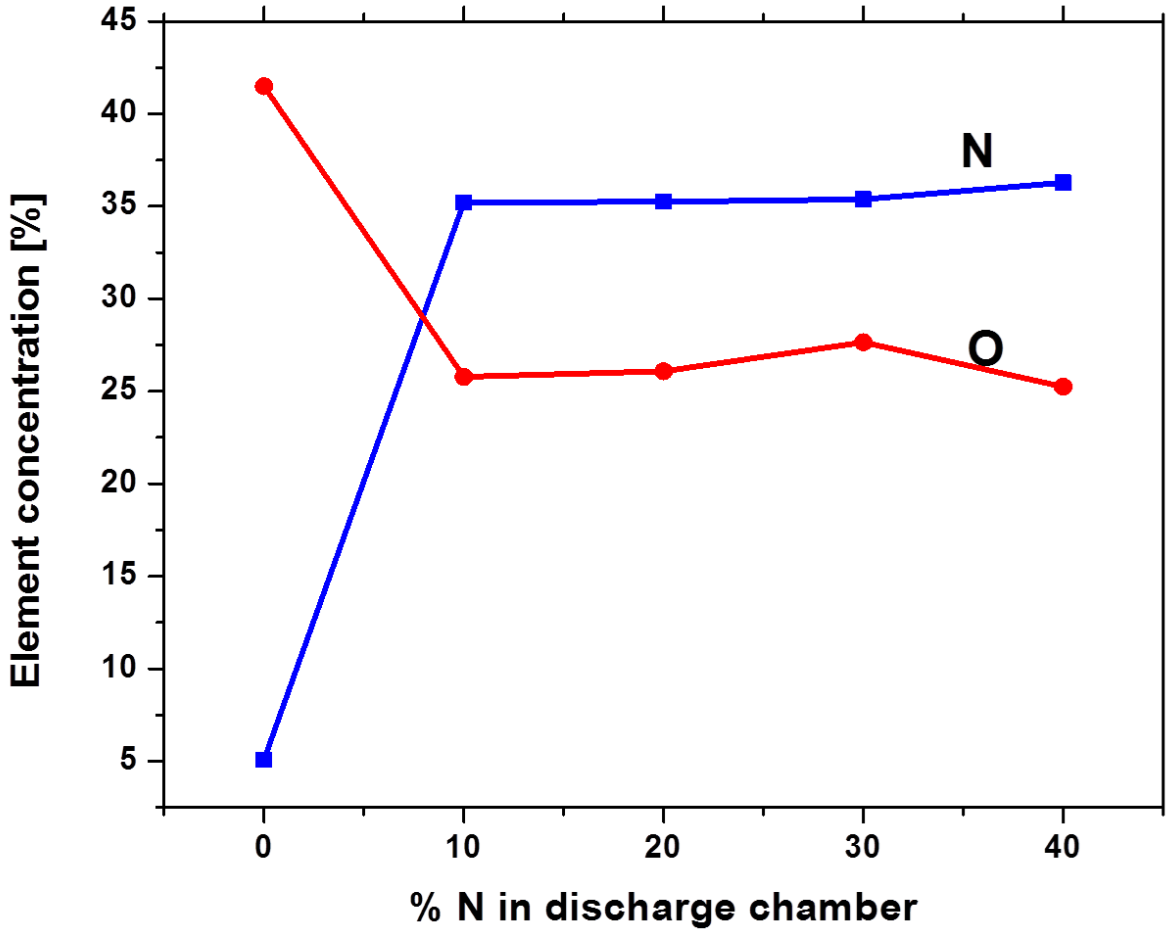

Figure 54. Surface concentration of nitrogen and oxygen in ICN_X samples

The XPS spectrum of PTFE used in this research is shown in Figure 55. The carbon 1s peak intensity is low but still might affect the C 1s spectra of the coated films.

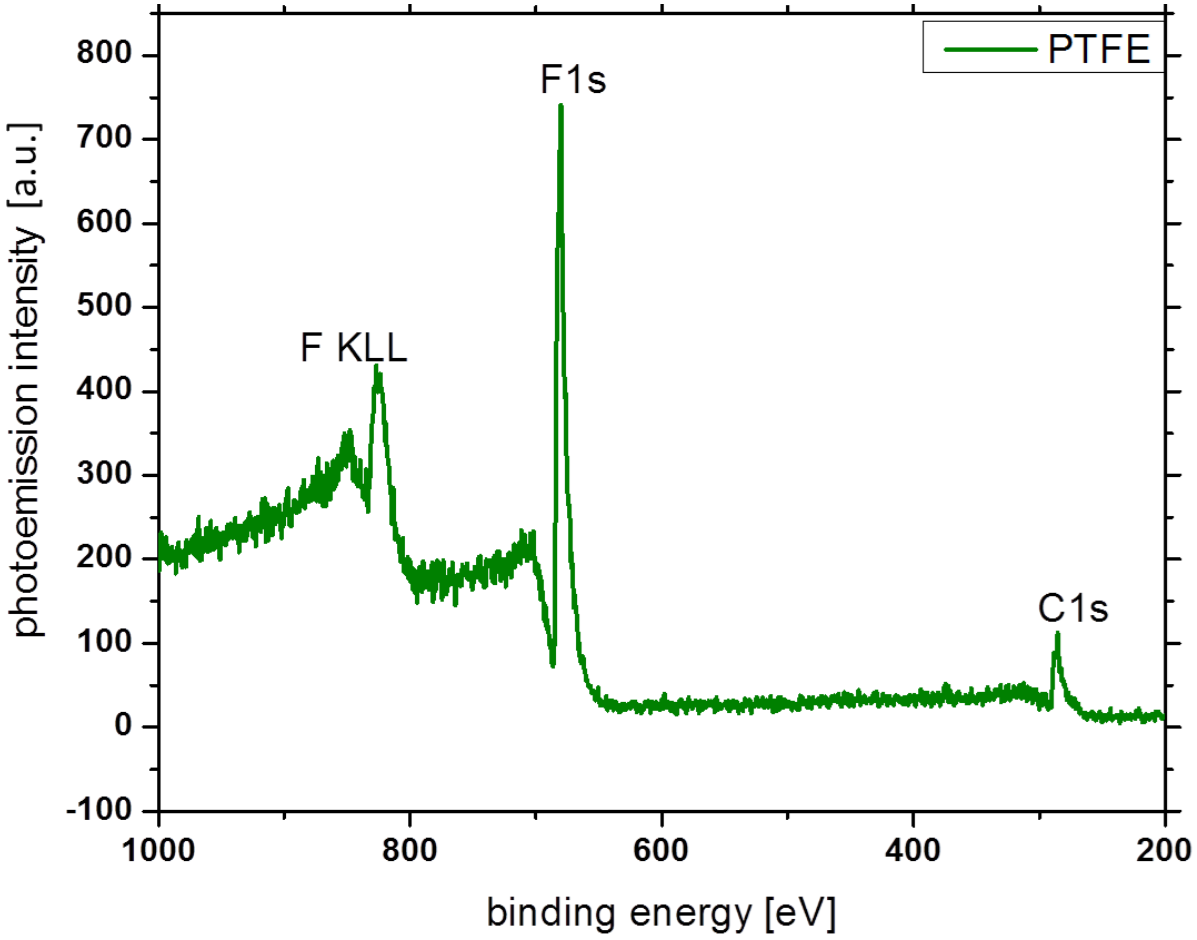

Figure 55. XPS spectrum of bare PTFE

Glance emission with take-off angle (θ = 37°) and normal emission (θ = 90°) spectra of ICN_{30} are compared in Figure 56. It shows that the F 1s and the F KLL are both reduced in intensity in GE mode, while other peaks are the same in intensity, which suggests that there is more fluorine (from PTFE) in depth rather than on the surface.

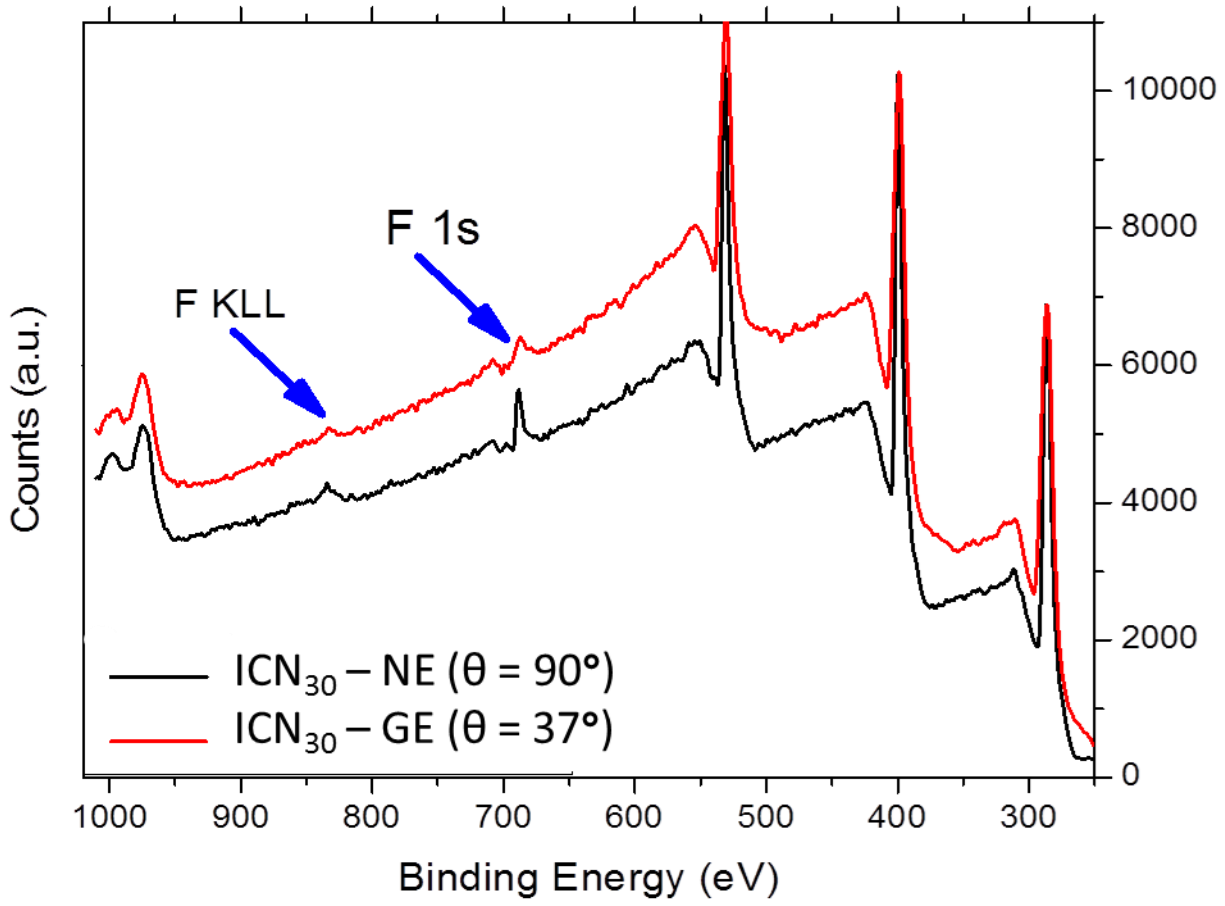

Figure 56. Wide scan XPS spectra of ICN_{30} in the NE and the GE modes

Figure 57 compares the NE and GE modes of XPS spectra of ICN_0 in the energy range of 650-850 eV. It shows that the amount of iron found is reduced as the depth of probing increases.

Confirming the existence of iron in ICN_0 requires a higher resolution XPS spectrum of the ICN_0 was collected in the range of 650-950 eV. As shown in Figure 58, Fe LMM auger peaks and Fe 2p indicate that there are small amounts (~2%) of iron in the sample.

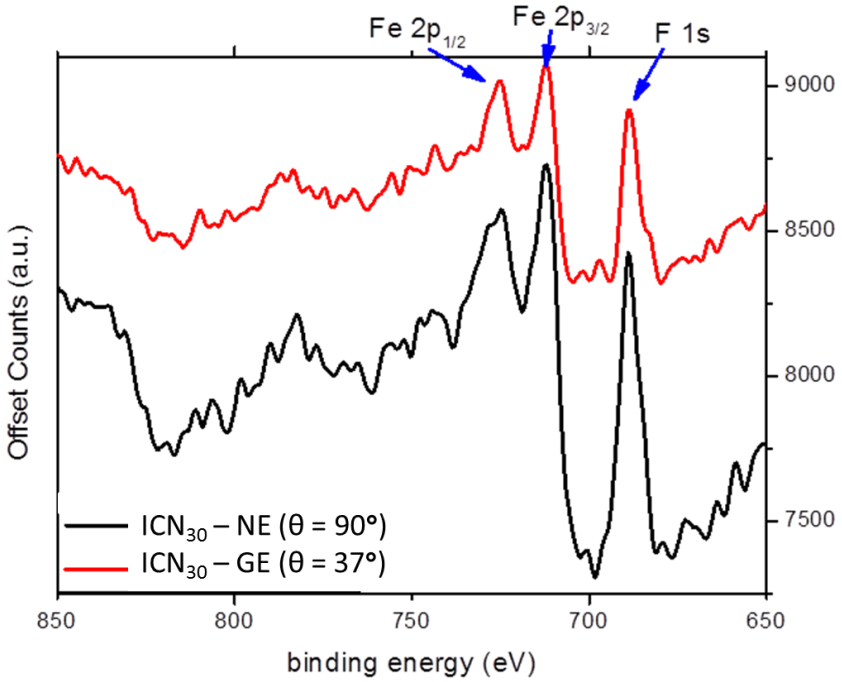

Figure 57. NE and GE modes of XPS spectra of the ICN_0 in the energy range of 650-850 eV

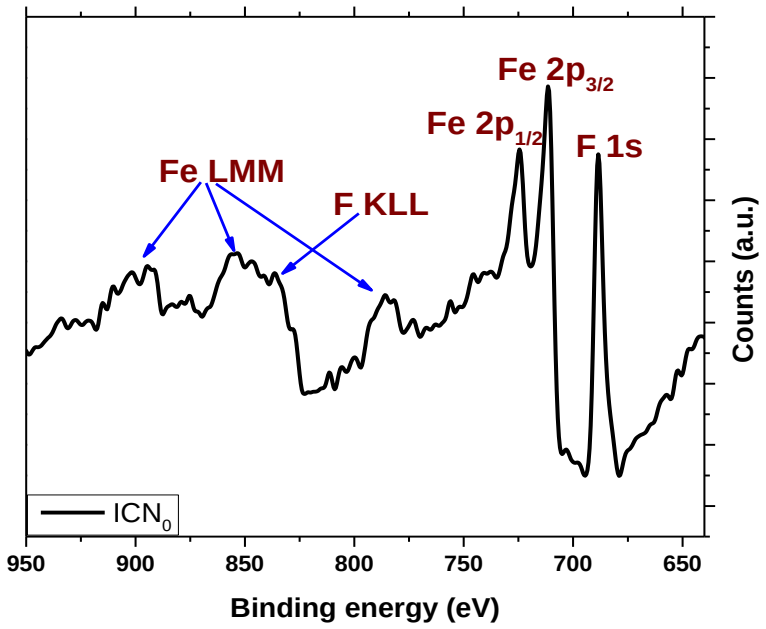

Figure 58. XPS spectrum of the ICN_0 in the energy range of 650-950 eV

The narrow-scan C 1s spectra recorded from ICN_X samples are presented in Figure 59. All the C 1s spectra were deconvoluted using Gaussian fit. The deconvolution that exhibit the best fit of the C 1s spectra were fitted with four Gaussian peaks. The curve fitting was done using Originpro 8.6 software. These peaks can be related to the various carbon bonds such as C-N, C-C, and C-O. C-C sp^2 and sp^3 bonds can also be distinguished in C 1s XPS spectra [71, 72, 73, 74, 75]. As shown in Figure 59, C 1s peaks are broadened with increasing nitrogen contents. Interestingly, the C 1s peak is shifted to a higher binding energy with adding nitrogen. The two blue dashed lines show that the C 1s peak is shifted 1.3 eV. This might be due to the increase in nitrogen contents, which in turn causes peak broadening. (I), (II), (III), and (IV) are the four Gaussian peaks used for the curve fitting. Peak (II) corresponds to Carbon-carbon (C-C) bonds and shows both sp^2 and sp^3 bonds. However, we were unable to distinguish the C-C sp^2 and sp^3 bonds, since the finding of peak (I) was unexpected and made the analysis difficult. It seems possible that the peaks (I) and (III) are due to the carbon-nitrogen bonds (C=N and C≡N) because they are grown with the increasing nitrogen content and cause broadening of the C 1s peaks. Peak (IV) is related to the C-O bonds and it is almost constant in all samples. Another possible explanation for the unexpected peak (I) is that the PTFE itself has carbon bonds that can have an effect on C 1s spectra. The fluorine was detected on the surface meaning that the some parts of the carbon peaks are related to carbons in PTFE.

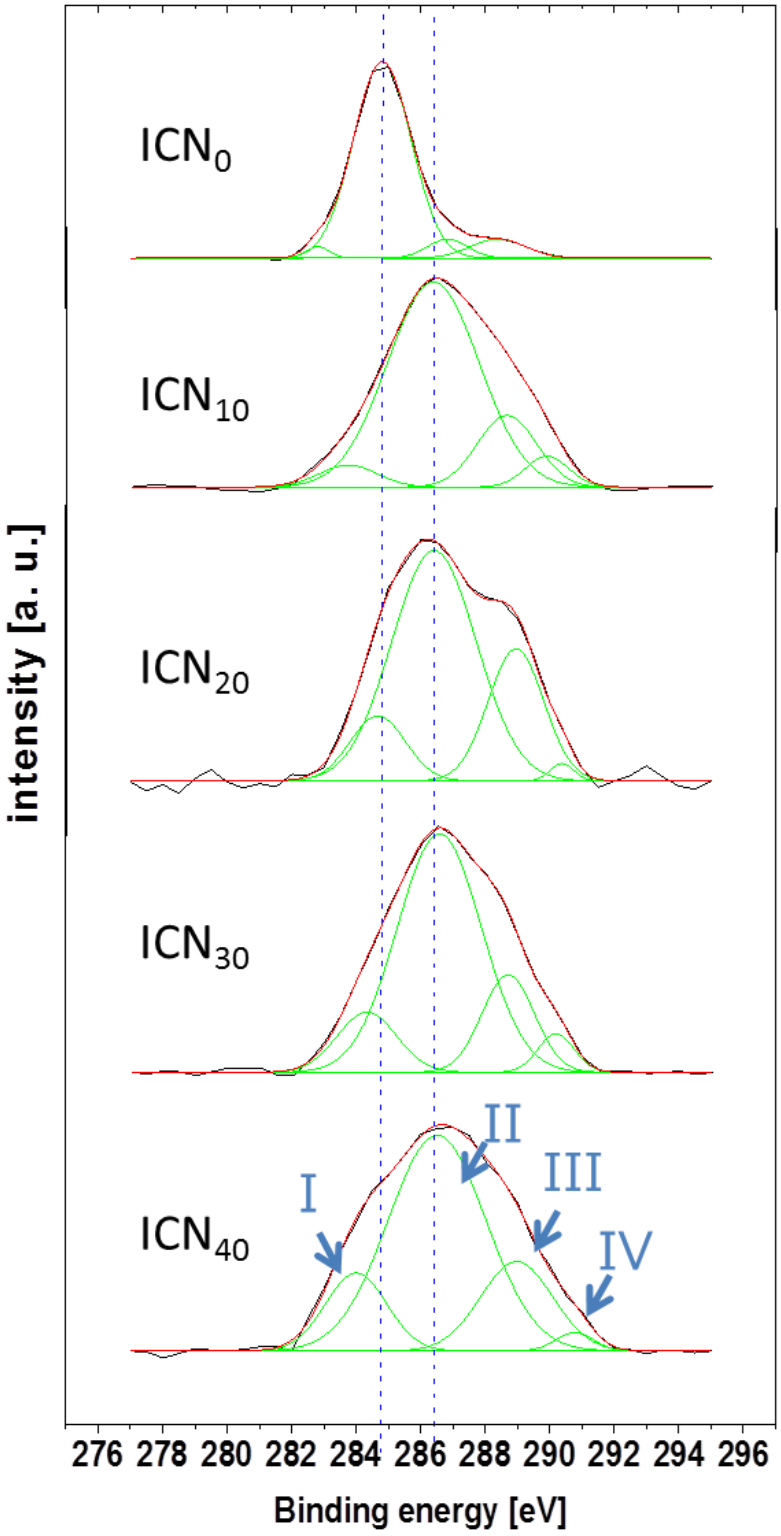

Figure 59. Narrow-scan C 1s XPS spectra acquired from ICN_X films (black curves). (I), (II), (III), and (IV) are four Gaussian peaks used for curve fitting (red lines are the fitted curves).

Table 8 shows the curve fitting data for peaks (I), (II), (III), and (IV) of the C 1s XPS spectra for all samples. Based on the area under each peak, it can be concluded that the C-O peak's relative area remains almost constant (below 8%). On the other hand, the relative areas under peaks (I) and (III) increase monotonically with increasing the nitrogen content, except for a slight decrease in the ICN_{30} sample. Figure 60 demonstrates the change in relative area percentage of each peak and shows that there has been a gradual decrease in C-C peaks.

Table 8. Curve fitting Gaussian peaks data for the C 1s XPS spectra

	Peak index	Area	Area percentage	FWHM	Max height	Center position
ICN_0	I (C-N)	1030.5	2.001432	0.859	1126.68	282.80
	II (C-C)	43456.8	84.40159	2.104	19403.84	284.80
	III (C-N)	2949.3	5.728116	1.480	1872.93	284.83
	IV (C-O)	4051.53	7.868862	2.027	1877.62	288.39
ICN_{10}	I (C-N)	1921.1	5.005367	2.129	847.82	283.72
	II (C-C)	28108.3	73.23532	3.350	7881.94	286.35
	III (C-N)	6348.4	16.54056	2.164	2755.23	288.64
	IV (C-O)	2003	5.218755	1.591	1182.75	289.88
ICN_{20}	I (C-N)	1271.3	11.6768	2.016	592.35	284.66
	II (C-C)	6874.7	63.14363	3.081	2095.79	286.41
	III (C-N)	2593.8	23.82387	2.029	1200.84	288.95
	IV (C-O)	147.6	1.355696	0.876	158.26	290.37
ICN_{30}	I (C-N)	2212.1	11.82284	2.165	959.82	284.33
	II (C-C)	12481.3	66.70782	3.081	3805.31	286.57
	III (C-N)	3151.8	16.84518	1.904	1554.81	288.71
	IV (C-O)	865.2	4.624166	1.320	615.38	290.19
ICN_{40}	I (C-N)	2491.3	14.40866	2.225	1051.72	284.00
	II (C-C)	11060.3	63.96824	3.574	2907.04	286.50
	III (C-N)	3374.3	19.51557	2.632	1204.32	288.97
	IV (C-O)	364.4	2.10754	1.374	249.12	290.76

From this data (Figure 60) we can see that nitrogen atoms substitute for carbon atoms in carbon-carbon bonds after doping with nitrogen. It seems possible that these results cause reducing the carbon-carbon bonds and increasing the carbon-nitrogen bonds. As expected nitrogen doping does not make any significant change on carbon-oxygen bonds.

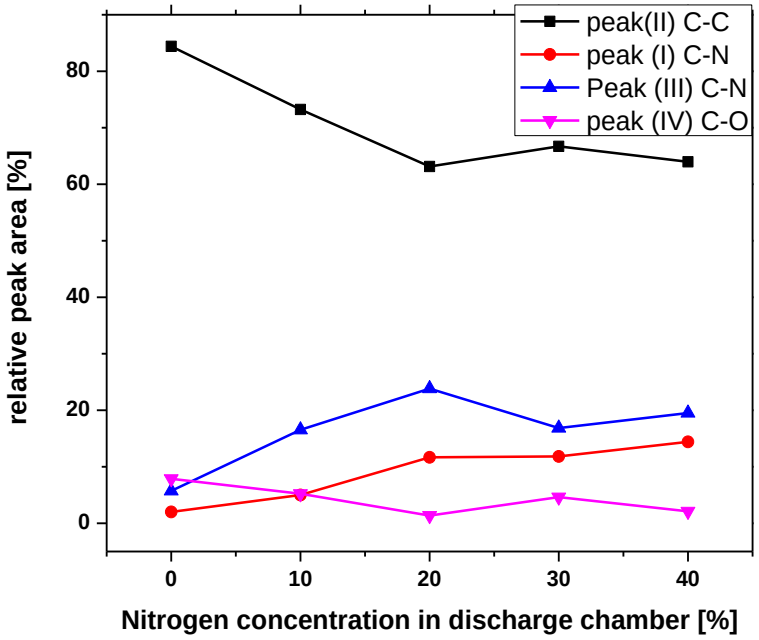

Figure 60. Relative peak area for four Gaussian peaks used in curve fitting of the C 1s XPS spectra

4.6 X-ray absorption spectroscopy

4.6.1 Introduction

X-ray absorption spectroscopy (XAS) is a technique for investigating chemical speciation and the local geometry of materials [8]. It is also used to investigate the local, partially unoccupied electronic density of states and the chemical bonding state in an atom. The XAS generally works

based on the measurement of the X-ray absorption coefficient μ. When a monochromatic X-ray beam, which is usually produced in synchrotron radiation, hits the sample or any material with intensity I_0, its intensity is reduced because of X-ray absorption according to the expression $I(x) = I_0 e^{-\mu x}$, where x is the thickness of the material and μ is the absorption coefficient. If an X-ray beam with a sufficiently high energy excites a core electron of an absorbing atom, three major phenomena happen: emission of a photoelectron, emission of auger electrons and fluorescence (Figure 61 [76]).

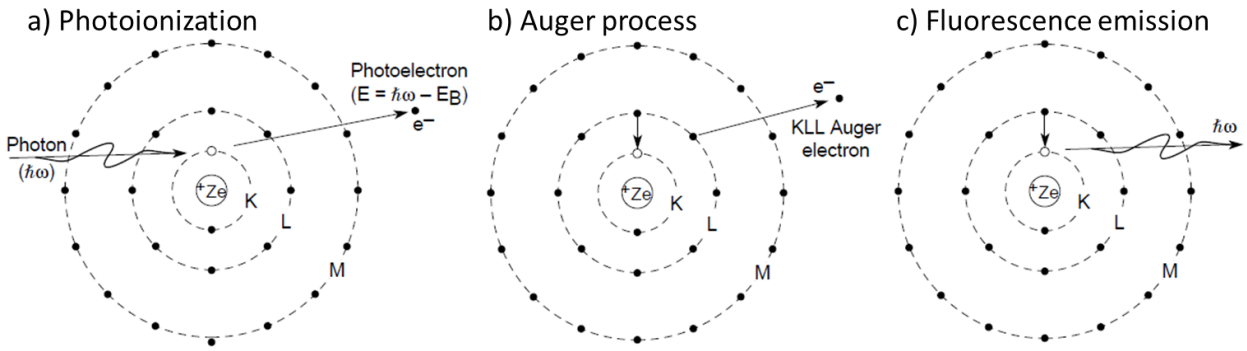

Figure 61. Schematic diagram of a) emission of photoelectron, b) auger, and c) fluorescence. Incident X-ray photon is absorbed by the sample. It causes emission of photoelectron and is followed by creation of a vacancy in the core hole. Transition of higher energy level electrons to this vacancy could cause the emission of auger electron or fluorescence.

Since each element has specific and well-known binding energy, which is the energy that a core electron needs to absorb in order to escape from the nucleus, the absorption edge on XAS can show the element speciation of the samples. Mainly, XAS deals with the measurement of the absorption coefficient μ as a function of photon energy. μ is a decreasing function of energy except for a steep rise at the absorption edge occurring at specific values of the photon energy emitted by a photoelectron [77, 78].

Beside transmittance, described above, there are three other common methods for performing the XAS measurement: (1) Total electron yield (TEY), (2) total fluorescence yield (TFY), and (3) partial fluorescence yield. As shown in Figure 61 , a photoelectron and an auger electron may be emitted from a sample by X-ray absorption leaving a net positive charge on the sample. External electrons (electric current) are needed to offset the sample's positive charge as a function of energy, which is related to the absorption spectrum and the partial density of state [79]. Thus, basically the TEY allows counting escaped electrons from the sample by neutralizing the sample. The absorption spectrum depends on the conductivity of the sample. In conductive samples, electrons can easily move within the sample to fill the vacant core holes, while it is hard to flow electrons on the surface of an insulator. Moreover, the TEY is highly surface-sensitive since the mean free path of an electron in the carbon-edge energy range is about 12 Å (Figure 62 [79]).

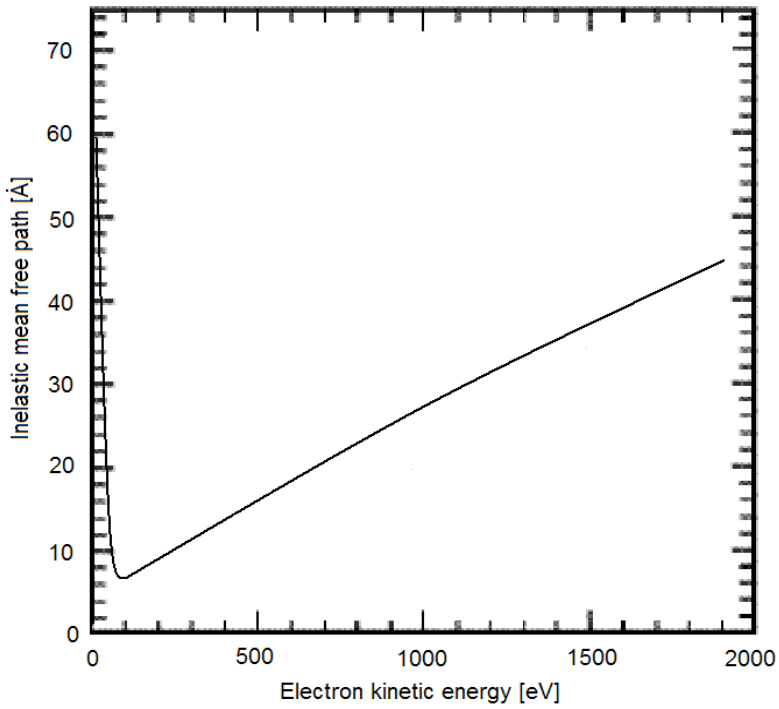

Figure 62. Electron inelastic mean free path up to 2000 eV in Carbon

Electron dipole transition from a higher-level energy to a core hole causes a photon to be emitted, whose energy is equivalent to the difference between those levels. Measuring all the fluorescence photons is called total fluorescence yield (TFY). Because they are directly related to each other, measuring TFY also gives an exact count of absorbed photons. Fluorescence photons are detected by a channeltron, which is a cascade multiplier that produces a signal proportional to the number of photons hitting it. So the TFY absorption is the number of fluorescence photons as a function of excitation energy.

If the detector measures the fluorescence photons in a certain range of energy instead of detecting all fluorescence photons as a function of excitation energy, it would be called partial fluorescence yield (PFY). Unlike the TEY, the fluorescence yield techniques are bulk-sensitive. In the carbon K-edge energy range the photons' attenuation length is about 100 nm. It means the X-ray photons can excite carbon atoms to the depth of 100 nm into the sample, and fluorescence photons can escape from up to 100 nm deep within the sample and be detected.

The X-ray source used for XAS is synchrotron radiation. Synchrotron based X-rays are produced by accelerating electrons to relativistic speeds (only 5 m/s slower than the speed of light in CLS) and forcing them to have a circular path using bending magnets. Confined electrons in the circular path (storage ring) can radiate electromagnetic waves. Changes in the velocity vector of electrons when it bends cause this electromagnetic radiation to be confined in a cone (Figure 63).

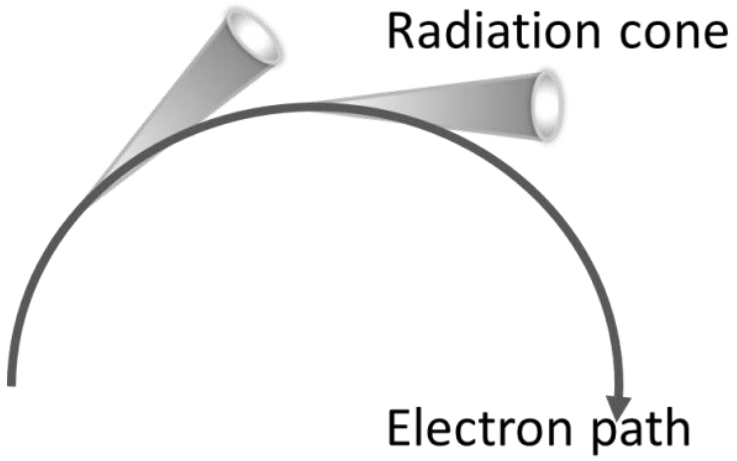

Figure 63. Schematic of a synchrotron radiation

In order to highly focus the radiation, insertion devices (wiggler or undulator) are placed in the storage ring. Insertion devices are arrays of permanent magnets and cause electrons to wiggle in their path and emit radiation at each pole.

4.6.2 Experimental results and discussion

The XAS experiments were performed in the REIXS beamline at the Canadian Light Source (CLS), University of Saskatchewan.

XAS spectra of ICN_X samples were recorded using TEY method in the REIXS beamline. Figure 64 shows the X-ray absorption spectroscopy of ICN_X samples. Change in spectra can be observed after the introduction of nitrogen, suggesting change in the electronic structures of samples. As shown in Figure 64, the ionization potential of carbon materials is located around 289-291 eV. Below the ionization energy (285-290 eV range) corresponds to the π^* states and above the ionization energy (290-320 eV range) represents the σ^* anti-bonding states. However, it is hard to distinguish these two anti-bonding states by a clear borderline. There are three

features in the π^* states region labelled A, B, and C. In nitrogen-doped samples, a dramatic drop can be seen in the features A and B, peak C has increased, and the features A and B are shifted to the left while the peak C remains at its original position. In the background of Figure 64, the XAS spectrum of highly ordered pyrolytic graphite (HOPG) is shown in a grey filled area as a reference. All atoms in the HOPG are fully sp^2 hybridized. Thus, there is an unhybridized 2p orbital in the HOPG structure that can form a π bond. The lowest energy feature of C 1s XAS spectra of HOPG occurred at 285.5 eV. This feature is related to the electron transition from 1s level to the π^* bands. Other features can be seen in the σ^* region and correspond to the electron transition of 1s to the σ^* bands.

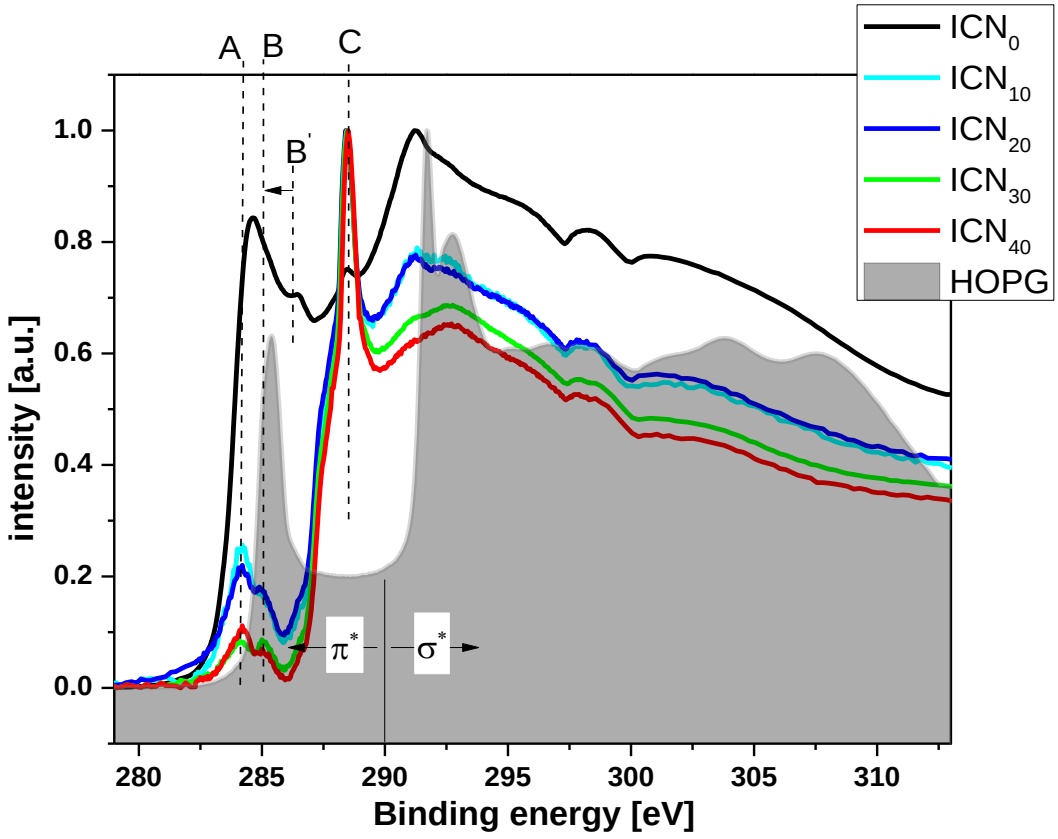

Figure 64. C 1s XAS spectra of ICN_X samples and highly ordered pyrolytic graphite (HOPG)

As mentioned earlier, the relative number of sp^2 and sp^3 bonds is important for studying the characteristics of an amorphous carbon film. The relative number of sp^2 bonds can be estimated by the relative number of π electrons [8]. If it is possible to separate the π^* and the σ^* in XAS spectra, the relative quantity of π electrons can be calculated. Comparing the relative quantity of π electrons in amorphous carbon films with a fully sp^2 hybridized reference material such as HOPG and μc-graphite is a method for computing the sp^2 contents quantitatively [80]. The sp^2 contents can be calculated by

$$\%sp^2 = 100\% \ \frac{I^{\pi}}{I^{t}} \times \frac{I^{t}_{ref}}{I^{\pi}_{ref}} \tag{4.3}$$

where I^{π} and I^{t} are integrated counts over π* features and the whole π* and σ* region respectively in XAS spectra. Similarly, I^{π}_{ref} and I^{t}_{ref} are integral intensities of π* region and both π* and σ* regions for the reference material (HOPG) respectively. Separation of π* and σ* features can be done by fitting the spectrum by Gaussian peaks. The fitting can be done either considering the ionization potential or without it. The ionization potential used here is a step-like function with onset at 290 ± 1 eV and its height chosen at the spectral height between 315-320 eV [80]. One criticism of Hamilton *et al*. [79] on this method is whether the exponential decay should be applied to the ionization potential. However, their sp^2/sp^3 values didn't completely match with the EELS (electron energy loss spectroscopy) results.

Fitted XAS spectra are shown in Figure 65. The integration energy window of 280-317 eV is chosen since spectra are almost at the same height in the 315-320 eV range. Both π* and σ* regions are fitted by three Gaussian peaks for all samples except the HOPG. However, the σ* regions were fitted by various numbers of peaks.

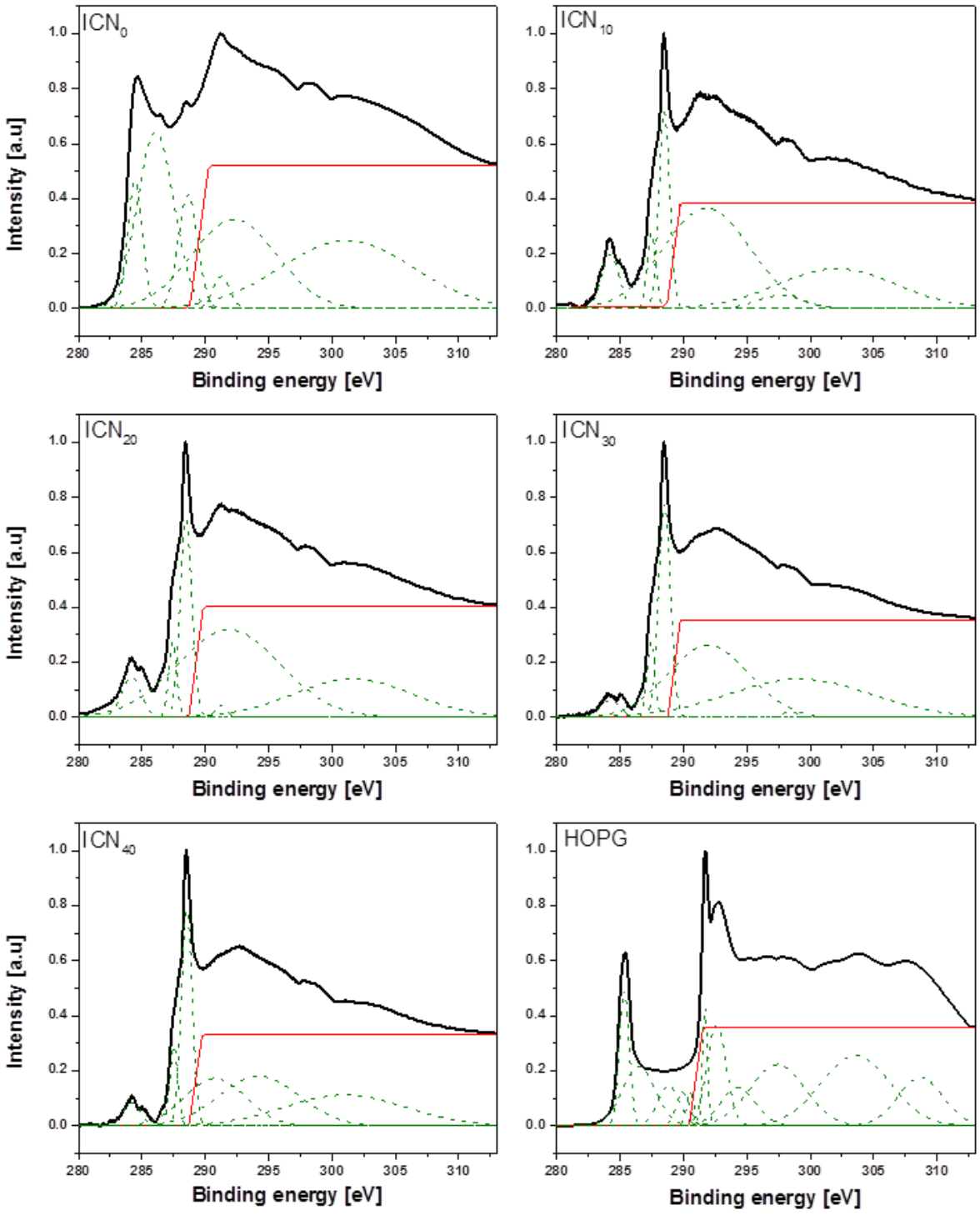

Figure 65. Fitted C 1s absorption spectra of HOPG and ICN_X samples

Peak areas were calculated and the relative area of three π^* region peaks were used to determine the sp^2 concentration. Partial peak area for three π^* peaks of ICN_X samples and HOPG are listed in Table 9. The total partial area of these three peaks for the HOPG is 25.32%, which is considered to have 100% sp^2 carbon bonds. Based on this reference sample, sp^2 concentrations in other samples were estimated.

Table 9. XAS spectra fitting results and sp^2 concentration of each ICN_X sample

Sample	π^* peaks position [eV]	Partial peak area		sp^2 concentration [%]
		Each of three	Total of three	
HOPG	285.3 286.5 288.8	7.9% 11.2% 6.5%	25.6%	100%
ICN_0	284.5 286.4 288.6	6.1% 13.1% 4.5%	23.7%	92.5%
ICN_{10}	284.2 287.5 288.5	5.3% 3.6% 11.8%	20.7%	80.8%
ICN_{20}	284.2 287.4 288.5	4.4% 3.4% 13.3%	21.1%	82.4%
ICN_{30}	284.2 287.4 288.5	2.2% 3.9% 17.1%	23.2%	90.6%
ICN_{40}	284.2 287.5 288.5	2.9% 4.4% 16.8%	24.1%	94.1%

The sp^2 concentration for ICN_X samples decreases with adding nitrogen and then increases with increasing nitrogen. The sp^2 concentration reaches its minimum at 10% nitrogen concentration. The error of these calculations was estimated by Hamilton (2005) [79]. He considered both statistical and systematic errors to be around 4-7%. Furthermore, many parameters such as

choice of reference sample and onset for ionization potential may affect the results. Thus, it is difficult to put an accurate interpretation on the fitting results.

4.7 X-ray emission spectroscopy

4.7.1 Introduction

X-ray emission spectroscopy (XES) is used to measure the occupied electronic state on a sample surface. A monochromatic X-ray beam hits the sample and excites the core electron. The emission of a photon is the result of the decay of an excited state, caused by an excited core electron. The filling of a previously created core hole by a valence band electron is followed by emission of a photon. A schematic of the photon emission is shown in Figure 66. The energy of the emitted photon is the energy difference between the core hole level and the state (usually in valance state) from which the electron fell. So the XES is the count rate or the intensity as function of emission energy.

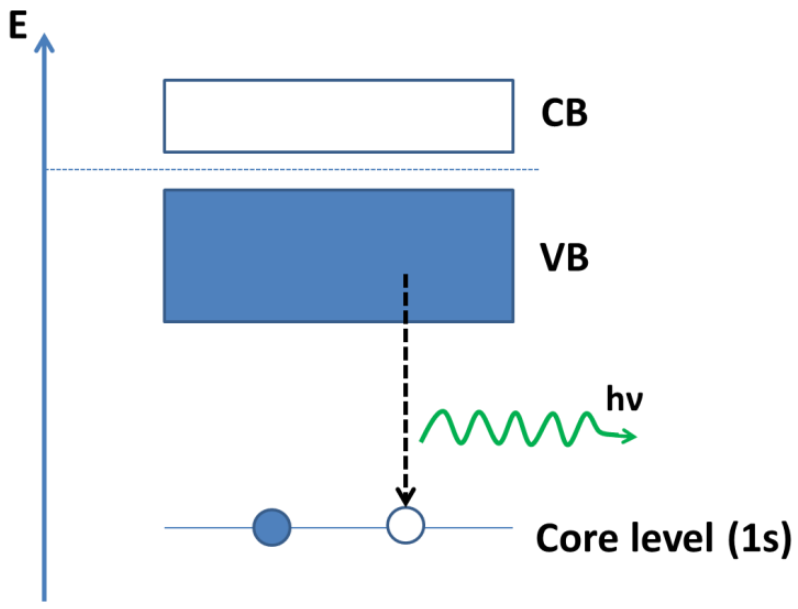

Figure 66. Schematic of emission of a photon by decaying an electron from valence band

4.7.2 Experiment results and discussion

XES spectra of ICN_X samples were recorded using REIXS beamline at the Canadian Light Source (CLS). Figure 67 illustrates the XES spectra of HOPG and ICN_X samples. There are not any clear differences in the ICN_X XES spectra. The XES spectra of ICN_X samples suggest that doping nitrogen does not cause any significant changes in the density of the occupied states in amorphous carbon films. The emission of carbon Kα means that the transition occurs from 2p to 1s energy level. An implication of this is the possibility that doping nitrogen did not change the occupied 2p state.

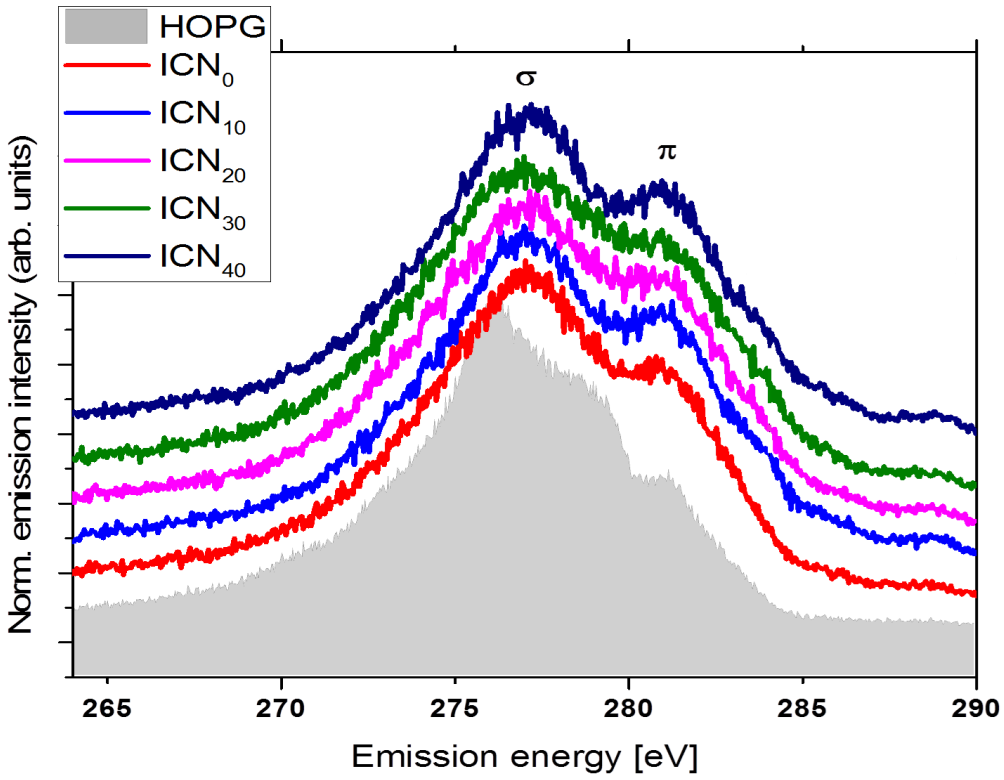

Figure 67. C Kα XES spectra of ICN_X films and HOPG

CHAPTER 5

CONCLUSIONS AND SUGGESTIONS FOR FUTURE RESEARCH

5.1 Summary

The purpose of this research is to coat DLC at low temperatures on PTFE substrates to make them more biocompatible with the human body when PTFE are used as implants, such as stents, for medical applications. Diamond-like carbon and nitrogenated diamond-like carbon films with varying nitrogen content in the working gas were successfully coated on PTFE and Si substrates using plasma sputtering in two different plasma sources, HFCVD and ICP. Coating DLC by ICP plasma sputtering is the new developed technique. Nitrogen doping level was controlled by adjusting N_2 partial gas flow rate. Producing amorphous carbon films by ICP sputtering has advantages over hot filament plasma. Deposition at low substrate temperature is the most important feature of DLC coating in ICP. This is advantageous for substrate with low melting temperatures such as polymers and plastics. The melting point of PTFE is 327° and the substrate temperature measured for HFCVD and ICP are ~200° and ~50° respectively. The thermocouples were located under the substrate holders. Hence the substrate temperature may be higher than the reported temperature. Due to the higher plasma density in ICP plasma, the deposition rate is significantly higher than in the hot filament sputtering system. Deposition time reduced from 120 minutes in HF sputtering to 30 minutes in ICP sputtering for a similar thickness (~150 nm). Cleaner atmosphere (and thus less impurity) is another superiority of electrodeless ICP versus hot filament. Deposited films and also the nitrogen doping effect on DLC films were characterized using XRD, SEM, AFM, XPS, XAS, and XES to clarify effects of nitrogen doping.

XRD patterns of coated films confirmed that the deposited DLC films are amorphous. Diffraction spectra pattern of samples confirmed that the substrate (PTFE) were crystalized during the deposition process.

SEM and AFM images of the films showed a uniform coated surface. HCN_X samples, deposited in the hot filament plasma device, have a larger cluster in the range of 300 nm (smallest grain can be seen in the images) which could be seen in SEM images. On the other hand, carbon clusters in samples produced in ICP (ICN_X) are much smaller in size (about 40 nm in nitrogenated samples). The cluster size and surface roughness of ICN_X samples were measured and compared in AFM images for ICN_X samples. The results of this investigation showed that the grains size are decreased in nitrogen doped samples by almost 30% but it is not sensitive to the nitrogen percentage introduced to the chamber. The roughness of the raw PTFE surfaces is also decreased dramatically with DLC coating. However, the nitrogen contents in the plasma did not make any difference in the roughness and the cluster size and shape.

Studying the Raman spectra of ICN_X samples (G peak position, intensity ratio I_D / I_G, and FWHM) showed that by adding nitrogen, bond-disorder and carbon sp^3 content increase. In this investigation, the aim was to assess the structural information and the partial sp^3 content. Although many factors influence Raman spectra and make it difficult to make an accurate estimate of the sp^3 content, according to Ferrari and Robertson [67] and comparing their results (three stages diagram [Figure 48]) with our Raman data, we may conclude that the ICN_X samples have less than 20% sp^3 bonds. This finding is in agreement with the DLC ternary diagram (Figure 11) which indicates that the sp^3 content in sputtered DLCs are less than 20%. Raman spectra of HCN_X samples are comparable to the ICN_X Raman spectra up to 20% nitrogen concentration. Raman spectra of the both set of samples (ICN_X and HCN_X) are similar and

showed a similar trend in G position, I_D / I_G and FWHM of G peak with increasing nitrogen concentration. The D to G peak intensity ratio however, showed opposite trends with increasing nitrogen concentration in the plasma. A possible explanation for the observed increase in I_D / I_G could be attributed to the more disorder carbon contents and may not necessarily change the sp^3 content. Raman data are summarized in Table 10.

XPS study is to determine the surface atomic composition. The quantitative measurement of peak intensities indicated that the nitrogen concentration in ICN_X samples increases rapidly from ~5% in ICN_0 to ~35% in ICN_{10} and remains at the level with further increase nitrogen concentration in plasma up to ICN_{40}. On the other hand, the oxygen concentration decreases from ~42% in ICN_0 to ~26% in ICN_{10} and remains almost constant up to the ICN_{40}. In addition, XPS spectra of ICN_0 indicated that there are small amounts (~2%) of iron in the sample and the iron concentration is reduced as the depth of probing increases. It was also shown that there is no iron in the nitrogen doped samples. Furthermore, the C 1s XPS peak was analysed in detail to study the chemical bonding of C and N atoms. Deconvolution of the C 1s core level spectrum into four Gaussian components suggested that each Gaussian peak can be attributed to a specific bonding of C, N, and O. The results showed the increasing C-N bonds and decreasing C-C bonds with increasing nitrogen doping. This finding of the XPS study suggests the substitution of N atoms with C atoms. Moreover, it was difficult to distinguish between sp^2 and sp^3 carbon-carbon bonds due to the broad C 1s core level peaks.

XAS spectra of ICN_X samples showed the electronic structure and unoccupied electronic density of state of the samples. In general, Doping nitrogen changed the unoccupied electronic density of states (XAS) but the occupied density of states (XES) remained the same. This technique is able to estimate the sp^2 content of the sample comparing a reference material (HOPG) with 100% sp^2

content. The results have shown that the sp^2 content in the deposited samples varies from 80% in ICN_{10} to 94% in ICN_{40}. The present findings are consistent with the results drawn from Raman data. Both XAS and Raman spectra suggests the sp^2 contents are more than 80% in our deposited films. In addition, both measurements showed a dramatic drop in sp^2 content after adding nitrogen. Most important properties of ICN_X samples are summarized in Table 10.

These results signify the change in the structure of the films coated in a plasma with nitrogen dopant. However, the properties of the films are not sensitive to the percentage of doped nitrogen. Studying the relation between these properties and the biocompatibility remains as future work.

Table 10. Summary of properties of PTFE and ICN_X samples

	AFM measurements		**Raman analysis**			**Elements concentration [%]**		**sp^2 contents [%]**
	Cluster size [nm]	**RMS Roughness [nm]**	**I_D/I_G**	**G peak position [cm^{-1}]**	**FWHM (G) [cm^{-1}]**	**N**	**O**	
PTFE	-	662	-	-	-	-	-	-
ICN_0	57.6	179	0.51	1573.5	131.1	5.0	41.5	92.5
ICN_{10}	40.6	173	0.60	1564.8	176.8	35.2	25.7	80.8
ICN_{20}	39.2	160	0.47	1562.9	167.5	35.3	26.0	82.4
ICN_{30}	40.4	158	0.63	1565.2	173.8	35.4	27.6	90.6
ICN_{40}	41.3	159	0.61	1564.7	175.4	36.2	25.2	94.1

5.2 Suggestions for future research

This research opens up many questions which require further investigation. Since the ICP sputtering of DLC is a new technique, a number of possible future studies using the same experimental set up are apparent and more systematic studies on the effects of experimental parameters on the formation of amorphous carbon are needed. Suggestions are as follows:

1) Nitrogen can be introduced to the chamber with smaller steps (1-2 %) instead of 10 %.
2) The effect of varying RF power on DLC films produced by ICP sputtering is another possible future study.
3) Different bias (DC) voltage can be applied to the graphite target in the ICP setup and its possible influences on disordering, clustering and sp^3 contents can be studied.

Future research for characterizing the same samples can be focused on:

1) EELS (Electron Energy Loss Spectroscopy) and NMR for measuring the sp^3 contents with more accuracy.
2) Using ultraviolet Raman spectroscopy, since Raman G peaks in amorphous carbon disperse as a function of excitation energy. Thus, studying the dispersion gives more structural information of the films.
3) Using different substrates and studying the effect substrates on film growth and adhesion.
4) Substrate heating and its influences on DLC characteristics.
5) Thickness measurement is another practical implication to study the deposition rate and its influences on the structure of the DLC films including internal stress and adhesion.
6) More importantly, study of the biocompatibility of the DLC samples needs to be conducted to identify the relationship between the biocompatibility and other coating properties (chemical,

mechanical, electrical, etc.). Biocompatibility can be assessed by studying the interaction of the samples with whole blood, other blood cells, and body tissues. Studying the thrombogenicity, Blood clotting time, platelet adsorption and activation, and neutrophils adsorption are possible primarily tests that can be conducted. Some samples have already been sent to the collaborators. The results from those tests will likely help to shape the future research plan for DLC studies in the laboratory.

Bibliography

[1] "Angioplasty and Stenting," [Online]. Available: http://www.cedars-sinai.edu. [Accessed 2012].

[2] R. K. Roy and K. R. Lee, "Biomedical Applications of Diamond-Like Carbon Coatings: A review," *Wiley Interscience,* 2007.

[3] "myhealth.alberta.ca," 2011. [Online]. Available: https://myhealth.alberta.ca/health/pages/. [Accessed 2012].

[4] A. Yevzlin and A. Asif, "Stent Placement in Hemodialysis Access: Historical Lessons, the state of art and future directions," *Clin J Am Soc Nephrol,* vol. 4, pp. 996-1008, 2009.

[5] Gwon DI, Ko GY, Kim JH, Yoon HK, Lee IS, Kim KA and Sung KB, "A comparative analysis of PTFE-covered and uncovered stents for palliative treatment of malignant extrahepatic biliary obstruction.," *AJR Am J Roentgenol,* no. W463-9, 2010.

[6] D. I. Bower, An introduction to polymer physics, Cambridge: Cambridge university press, 2002.

[7] R. A. Pethrick, Polymer science and technology, Caithness, New Jersey, Hoboken: Whittles Publishing, 2010.

[8] M. Foursa, "Plasma- assisted deposition of nitrogen doped amorphous carbon films onto

polytetrafluroethylene for biomedical applications," 2007.

[9] C. Corbella Roca, "Thin film structures of diamond-like carbon prepared by pulsed plasma techniques," Thesis in Universitat de Barcelona. Departament de Física Aplicada i Òptica, 2006.

[10] H. O. Pierson, Handbook of carbon, graphite, diamond and fullerenes, Albuquerque, new mexico: Noyes publication, 1993.

[11] K. H. Ng, "Development of a planar coil radio frequency inductively coupled plasma system for material processing," Phd thesis in University Malaya, 2008.

[12] "Georgia Tech nanotechnology LAB," Georgia Tech nanotechnology LAB group, [Online]. Available: http://eosl.gtri.gatech.edu/Default.aspx?alias=eosl.gtri.gatech.edu/newnano. [Accessed 10 2012].

[13] F. F. Chen, "Introduction to plasma physicsand controlled fusion," Plenum Press, New York, 1984.

[14] F. F. Chen and J. P. Chang, Lecture notes on priciple of plasma processing, New York: Plenum Publisher, 2003.

[15] M. Liberman and A. Liehtenberg, Principles of plasma discharges and material processing, New York: John Willey & Sons, 1994.

[16] H. Li, "Meadurment of electron energy distribution function and neutral gas temperature in an inductively coupled plasma," Thesis, University of Saskatchewan, Saskatoon, 2006.

[17] A. Grill, "Diamond-like carbon: state of the art," *Diamond and related materials,* vol. 8, pp. 428-434, 1999.

[18] J. Angus and Y. Wang, "Diamond and Diamond-like films and coating," New york LLC, Springer-Voriag, 1991, p. 173.

[19] J. Robertson, "Diamond-like carbon," *Pure & Appl. Chem.,* vol. 66, pp. 1789-1796, 1994.

[20] W. Jacob and W. Moller, "On the structure of thin hydrocarbon films," *Appl. Phys. Lett.,* vol. 63, no. 10.1063/1.110683, p. 1771, 1993.

[21] A. C. Ferrari, "Non-destructive characterisation of carbon films," in *Tribology of Diamond-Like Carbon Films*, New York, Springer, 2008, pp. 25-82.

[22] A. Casiraghi, A. C. Ferrari and J. Robertson, "Raman spectroscopy of hydrogenated amorphous carbons," *Phys. Rev. B,* vol. 72, no. 10.1103, p. 085401, 2005.

[23] A. C. Ferrari, "Non-destructive characterisation of carbon films," in *tribology of diamond-like carbon films*, New York, Springer, 2008, pp. 25-30.

[24] H. Schmellenmeier, *Experimentelle Technik der Physik*, vol. 1, p. 49, 1953.

[25] S. Aisenberg and R. Chabot, "IonBeam Deposition of Thin Films of Diamondlike Carbon," *J. Appl. Phys.* , vol. 42, no. 10.1063/1.1660654, p. 2953, 1971.

[26] L. Holland and S. M. Ojha, "The growth of carbon films with random atomic structure from ion impact damage in a hydrocarbon plasma," *Thin Solid Films,* vol. 58, no. 1, pp. 107-116,

1979.

[27] K. Bewilogua, D. Dietrich, L. Pagel, C. Schurer and C. Weissmantel, "Structure and properties of transparent and hard carbon films," *Surface Scince,* vol. 86, pp. 308-313, 1979.

[28] C. Weissmantel, K. Bewilogua, C. Schurer, K. Breuer and H. Zscheile , "Characterization of hard carbon films by electron energy loss spectrometry," *Thin Solid Films,* vol. 61, no. 2, pp. L1-L4, 1979.

[29] T. C. Arnoldusson and E. M. Rossi, "Materials for magnetic recording," *Ann. Rev. Mater. Sci.* , vol. 15, pp. 379-409, 1985.

[30] F. K. King, "Datapoint thin film media," *IEEE Trans. Magn.*, vol. 17, no. 4, p. 1376, 1981.

[31] C. Donnet and A. Erdemir, Tribology of diamond-like carbon films, fundamental and application, New York: Springer, 2008.

[32] F. Jason, M. Mackonkin, S. Kaplan, S. Hark and J. Vac, *Sci. Technol. A 3,* p. 605, 1985.

[33] Y. Catherine, "Diamond and diamond-like carbon thin films," *NATO ASI,* p. 193, 1991.

[34] J. Angus, P. Koidl and S. Domitz, Plasma deposited thin films, Boka Raton: CRC Press, 1986.

[35] A. Voevodin and M. Donley, "Surf. Coating Technol. 82," p. 199, 1996.

[36] A. Anders, *Surf. coating technol.,* vol. 121, p. 319, 1999.

[37] B. Bhushan, "Chemical, mechanical and tribological characterization of ultra-thin and hard amorphous carbon coatings as thin as 3.5 nm," *diamond And related materials,* p. V 8. Issuee 11, 1999.

[38] J. Schwan, S. Ulrich, H. Roth and H. Ehrhardt, "Tetrahedral amorphous carbon films prepared by magnetron sputtering and dc ion plating," *American Institute of Physics*, 1996.

[39] February 2012. [Online]. Available: www.plasma- universe.com.

[40] H. Conrads and M. Schmidt, "Plasma generation and plasma sources," *Plasma Sources Sci. Technol.*, vol. 9, pp. 441-454, 2000.

[41] J. Robertson, "Diamond-like amorphous carbon," *Material science and engineering R,* p. 37, 2002.

[42] S. Sethuraman, "ION BEAM DEPOSITION OF NITROGEN DOPED DIAMOND-LIKE CARBON THIN FILMS FOR ENHANCED BIOLOGICAL PROPERTIES," Thesis in university of Saskachewan, Saskatoon, 2009.

[43] G. Dearnaley and H. James, "Arps Biomedical applications of diamond-like carbon (DLC) coatings," *Surface & Coatings Technology*, pp. 2518-2524, 2005.

[44] C. J. Torng, J. M. Sivertson, J. H. Judy and C. Chang, "Structure and bonding studies of the C:N thin films produced by rf sputtering method," *journal of material research,* vol. 5, no. 10.1557, pp. 2490-2496, 1990.

[45] J. Robertson, "Diamond-like amorphous carbon," *Material science and engineering,* vol. 37,

pp. 129-281, 2002.

[46] G. Manickam, "Deposition of diamond films on steel substrates for tribological application," Thesis, Radboud Univerisy , Nijmegan, 2008.

[47] W. G. Eversole, "Synthesis of diamond". US Patent 3030187, 17 april 1962.

[48] S. Matsumoto, Y. Sato, M. Tsutsumi and N. Setaka, "Growth of diamond particles from methane-hydrogen gas," *Journal of material science,* vol. 17, pp. 3106-3112, 1982.

[49] J. W. Hittorf, *ann. phys.* , vol. 21, p. 90, 1884.

[50] G. I. Babat, "Electrodeless discharges and some allied problems," *Institution electrical engineering III, Radio communication,* vol. 94, no. 27, pp. 27-37, 1947.

[51] T. B. Reed, "Induction-coupled plasma torch," *Journal of Applied Physics,* vol. 32, no. 5, p. 821, 1961.

[52] A. D. Stokes, "Induction-field calculations and their application to measurements of conductivity distributions in cylindrical plasmas," *Institution of Electrical Engineering,* vol. 112, no. 8, pp. 1583-1588, 1965.

[53] G. L. Moore, Introduction to inductively coupled plasma atomic emission spectroscopy, New York: Elsevier, 1989.

[54] Y. Suidong, "Diagnostics and modelling of an inductively coupled RF low-pressure low-temperature plasma," Thesis, The Open university, Oxford, 1998.

[55] J. R. Roth, Industrial Plasma Engineering, Bristol and Philadelphia: Institute of Physics Publishing, 1995.

[56] J. Hopwood, "Review of inductively coupled plasma for plasam processing," *Plasam Source Science and Technology,* vol. 1, pp. 109-116, 1992.

[57] L. J. Mahoney, A. E. Wendt, E. Barrios, C. J. Richards and J. L. Shohet, "Electrondensity and energy distributions in a planar inductively coupled discharge," *J. Appl. Phys.* , vol. 76, no. 10.1063/1.357672, pp. 2041-2047, 1994.

[58] T. Okumura, "Inductively Coupled Plasma Sources and Applications," *Physics Research International,* vol. 2010, no. 164249, p. 14 pages, 2010.

[59] 02 2012. [Online]. Available: http://chemwiki.ucdavis.edu.

[60] Y. A. Lebedev, Y. M. Korolev, V. M. Polikarpov, L. N. Ignat'eva and E. M. Antipov, "X-ray poder diffraction study of Polytetrafluoroethylene," *Structure of Organic Compounds,* vol. 55, no. 10.1134/S1063774510040127, pp. 651-656, 2010.

[61] E. Charles and J. Carraher, Seymour/Carraher's polymerchemistry, CRC Press, 2003.

[62] 02 2012. [Online]. Available: http://www.few.vu.nl/~wroos/Virus.html.

[63] D. Ricci and P. C. Braga, "How the Atomic Force Microscope Works," in *Atomic Force Microscopy : Biomedical Methods and Applications*, Totowa, New Jersey, Human Press, 2004, pp. 3-12.

[64] D. Ricci and P. C. Braga, " Imaging Methods in Atomic Force Microscopy," in *Atomic Force Microscopy : Biomedical Methods and Applications*, Totowa, New Jersey, Human Press, 2004, pp. 13-23.

[65] R. J. Milewski, Y. Kumagai, K. Fujita, D. M. Standley and N. I. Smith, "Automated processing of label-free Raman microscope images of macrophage cells with standardized regression for high-throughput analysis," *Immunome Research,* no. 10.1186/1745-7580-6-11, 2010.

[66] A. Ferrari and J. Robertson, *J. Philos. Trans. R. Soc. Lond., Ser. A: Math.Phys. Eng. Sci.,* pp. 362, 2477, 2004.

[67] A. C. Ferrari and J. Robertson, "Raman spectroscopy of amorphous, nanostructured, Diamond-like carbon, and nanodiamond," *The royal society,* no. 10.1098/rsta.2004.1452, 2004.

[68] J. R. Shi, X. Shi, Z. Sun, S. P. Lau, B. K. Tay and H. S. Tan, "Resonant Raman studies of tetrahedral amorphous carbon," *Diamond and Related Materials,* pp. 76-81, 2001.

[69] W. G. Cui, Q. B. Lai, L. Zhang and F. m. Wang, "Quantitative measurements of sp3 content in DLC films with Raman spectroscopy," *Surface & Coatings Technology,* pp. 1995-1999, 2010.

[70] V. S. Yadav, D. K. Sahu, M. Singh and K. Kumar, "Study of Raman Spectra of Nano-crystalline Diamond Like Carbon (DLC) films Composition (sp2:sp3) with Substrate Temperature," *World Congress on Engineering and Computer Science,* vol. 1, no.

ISBN:978-988-17012-6-8, 2009.

[71] E. Riedo, F. Comin, J. Chevrier, F. Schmithusen and S. Decossas, "Structural properties and surface morphology of laser-deposited amorphous carbon and carbon nitride films," *Surface and Coatings Technology,* vol. 125, pp. 124-128, 2000.

[72] J. Filik, P. W. May, S. J. Pearce, R. K. Wild and K. R. Halla, "XPSand laser Raman analysis of hydrogenated amorphous carbon films," *Diamond and Related Materials,* vol. 12, pp. 974-978, 2003.

[73] S. Zhang, Y. Q. Fu, X. L. Bui and H. J. Du, "XPS study of diamond-like carbon-based nanocomposite films," *World Scientific Publishing Company,* vol. 3, pp. 797-802, 2004.

[74] T. W. Scharf, R. D. Ott, D. Yang and J. A. Barnard, "Structural and tribological characterization of protective amorphous diamond-like carbon and amorphous CNx overcoats for next generation hard disks," *J. Appl. Phys.* , vol. 85, no. doi: 10.1063/1.369654, p. 3142, 1999.

[75] J. L. Endirno, J. F. Marco, P. Poolcharuansin, A. R. Phani, M. Allen, J. M. Albella and A. Anders, "Functionalization of hydrogen-free Diamond-like film using open air dielectric barrier discharge atmospheric plasma treatment," *Applied Surface Science,* vol. 254, no. 17, pp. 5323-5328, 2008.

[76] D. Atwood, Soft X-rays and Extreame Ultraviolet Radiation: Principles and Applications, New York: Cambridge University Press, 1999.

[77] Y. Tang, "Plasma and ion beam enhanced chemical vapour deposition of diamond and diamond like carbon," 2010.

[78] 02 2012. [Online]. Available: http://commons.wikimedia.org/.

[79] T. D. Hamilton, "Determining the sp2/sp3 bonding concentration of carbon films," University of Saskatchewan , saskatoon, 2005.

[80] J. Diaz, S. Anders, X. ZHou, E. J. Moler, S. A. Keller and Z. Hussain, "Analysis of the p* and s* bands of the x-ray absorption spectrum of amorphous carbon," *PHYSICAL REVIEW B,* vol. 64, p. 125204, 2001.